Université de Neuchâtel
Institut de Microtechnique

Microcrystalline Silicon Solar Cells In The N-I-P Configuration: Optimisations On Light Scattering Back-Reflectors.

Thèse
Présentée à la Faculté de Sciences
pour optenir le grade de docteur ès sciences
par

Lukas Andreas Feitknecht

Imprimé: September 25, 2003

VERLAGSIMPRESSUM

Dissertation mit ISB-Nummer 3-935511-25-6
Band 424

IMPRIMATUR POUR LA THESE

Microcrystalline silicon solar cells in the N-I-P configuration: optimisations on light scattering back reflectors

de M. Lukas FEITKNECHT

UNIVERSITE DE NEUCHATEL

FACULTE DES SCIENCES

La Faculté des sciences de l'Université de Neuchâtel, sur le rapport des membres du jury

MM. A. Shah (directeur de thèse), H.-P. Herzig, H. Keppner (Le Locle) et M. Vanecek (Prague)

autorise l'impression de la présente thèse.

Neuchâtel, le 15 juillet 2003

Le doyen:

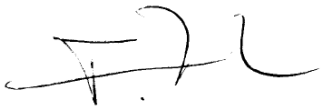

François Zwahlen

Der Dinggang

Langsam ist der Gang der Dinge
wenn es nach den Dingen ginge
dauerte es elend lang.
Sind die Dinge mal im Gang

muss man halt vor allen Dingen
sehr sehr viel Geduld aufbringen.
Hat es aber angefangen
mit den langen Dingendangen

sind sie endlich angesprungen
ist es tatsächlich gelungen
und sie kommen in die Gänge
Mann! Das zieht sich in die Länge

Und das geht so lang es geht
bis das Ding dann steht.

F. W. Bernstein

Abstract

Thin films of hydrogenated microcrystalline silicon (μc-Si:H) are deposited by the Plasma Enhanced Chemical Vapour Deposition method onto substrates with the aim to fabricate solar cell devices. In the time span from late 1997 to early 2002 the main challenge of this work is the optimisation of functional solar cells in the n-i-p configuration with respect to newly introduced substrates (e.g. glass, stainless steel, Kapton), better Transparent Conductive Oxide contact materials (sputtered ZnO (Zinc Oxide) at the back-contact and LP-CVD ZnO at the front contact, replacing ITO) while maintaining high film deposition rates around 8 Å/sec and resulting in conversion efficiencies around $\eta = 8\%$.

The transition from microcrystalline to amorphous growth conditions is observed based on a so called 'dilution series' which served for a variety of observations and which was used by many members of the research groups at IMT Neuchâtel and in Prag: Silicon films were deposited at various silane concentrations around the phase transition of microcrystalline to amorphous silicon, for both intrinsic films deposited onto glass and the intrinsic absorber layer within the n-i-p solar cells. Investigations on optical, electrical, and structural (crystallographic) aspects led to a better understanding of the μc-Si:H material.

This thesis is split into two parts:

Part I presents three fabrication methods of microcrystalline silicon thin films. The first chapter on the PE-CVD method comments on how films and cells are fabricated and analysed. The second chapter reports on the novel deposition method which combines the PE-CVD and Hot-Wire techniques in order to fabricate μc-Si:H solar grade material at rates exceeding 25 Å/sec; no other research group fabricated functional solar cells at such high deposition rates by this method at that time (1997) to our knowledge. In the third chapter amorphous silicon films are transformed by the Aluminium induced Crystallisation process into p-type doped poly-crystalline silicon films which then can be used for the fabrication of junctions whether in the p-n configuration or in a p-i-n configuration; first rectifying devices could be fabricated. This method is interesting because of a low energy consumption (compared to laser crystallisation) and the temperatures far below the strain temperature of glass (below 200°C).

Part II comments on the optimisation of n-i-p solar cells fabricated by PE-CVD method: The excellent optical absorption properties of μc-Si:H films are necessary but not sufficient for solar cell fabrication because the n-i-p device consists not simply of a succession of different films, but only a general view on the optimisation process of films, interfaces, substrates and the two electrical contacts (at the back and the front) result in a reasonably working solar cell. This implies optimisations on roughly 230 working microcrystalline silicon solar cells as well as many un-usable deposition runs where the layers peeled off, cells were destroyed only by the last structuring process or other incidents often encountered in that long fabrication chain from the substrate to the I-V characteristics of the solar cell.

The light-scattering back-reflector may considerably increase the performance of thin-film solar cells if the cell and the substrate are thoroughly matched. No "kitchen recipe" for *the* very high conversion efficiency solar cell can be given. This thesis sketches several aspects of thin-film silicon solar cell fabrication. These investigations are meant to promote cheaper and more efficient solar energy conversion.

Contents

List of Figures

List of Tables

Part I

Deposition methods and layer characterisation

Introduction

Silicon solar cells are fabricated essentially by two methods, the bulk process (mono- /multicrystalline wafers) and in the thin film technology. An important difference between the two solar cell technologies is the substrate: thin-film solar cells always are deposited onto a substrate while in the case of the wafer based cells *the cell is the substrate*. The 'thick' silicon wafer stands for both the active cell and the substrate, whereas 'thin' films of silicon are deposited onto glass, steel or plastic substrates (thus *foreign* substrates, meaning non-silicon substrates)[1]

Among all the existing fabrication methods, this chapter comments on three thin-film fabrication methods: first the Plasma Enhanced Chemical Vapour Deposition (PE-CVD) used here in form of Very High Frequency Glow Discharge (VHF-GD), second the combination of Hot-Wire and PE-CVD and as a third candidate the Aluminium induced Crystallisation (AiC) method. In each section, first the deposition method is explained in short, then the methods for characterisation of the fabricated films are presented and finally the observed results are reported. A discussion and interpretation of the results both of the deposition method and of the layer characterisation method terminates this first part.

A more detailed fine-tuning of solar cell fabrication by the PE-CVD technology is reported in part two of this thesis: The chapters on the introduction of back-reflecting substrates, device interface optimisation and the dilution series of the intrinsic absorber layer material are of paramount importance.

[1] In the context here, thick means above 300μm and thin means below 3 μm.

Chapter 1

PE-CVD

1.1 The deposition system

Fig. 1.1: Image of the PE-CVD deposition vacuum chamber 'System G' used for the fabrication of μc-Si:H n-i-p solar cells.

Thin silicon films were fabricated in a capacitively-coupled parallel plate reactor, using the very high frequency glow discharge (VHF-GD) method in a vacuum chamber. A plasma excitation frequency of 70-130MHz (i.e. within the VHF range) was used. The VHF-power is applied to the cathode, the introduced mixture of hydrogen and silane gas is decomposed in a plasma reaction and the reactive ions deposit onto the substrate which is attached to the anode. For n-type and p-type films, phosphorus and diborane doping gas diluted in hydrogen gas are used, respectively. A gas purifier was used

to avoid incorporation of detrimental oxygen contamination in intrinsic μc-Si:H layers[86]. The non-used gas remains are pumped out, they pass a burner at 700°C and are exhausted.

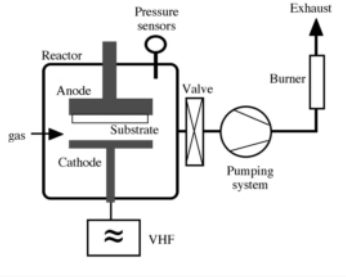

Fig. 1.2: Schematic set-up of the single-chamber VHF-GD deposition system which is mainly used to fabricate both μc-Si:H films and solar cells.

SiH_4 flow	1-10 sccm
H_2 flow	80-100 sccm
d-electr.	14 mm
pressure	0.1-0.9 mbar
VHF power	5-50 W
Frequency	70-130 MHz
temperature	200 °C

Table 1.1: Typical deposition parameters used for silicon film and solar cell fabrication.

A picture of the single-chamber VHF-GD deposition system at IMT Neuchâtel which has been used throughout this work for the fabrication of layers and solar cells is given in Fig. 1.1.

1.2 Film characterisation

Methods and results

One of the most important parameters in the PE-CVD deposition process of microcrystalline silicon thin films is the concentration of silane gas in hydrogen ($\frac{[SiH_4]}{[SiH_4+H_2]}$). In fact, a transition from microcrystalline to amorphous material is observed around 7% silane concentration (SC). Films deposited below that threshold are composed of a high crystalline amount whereas films deposited above that threshold tend to be amorphous. An increase in deposition rate from typically 5Å/sec up to 11 Å/sec (cf. section 1.3) for a variation from 5% to 8% SC accompanies the trend towards an amorphous growth regime. In other words, a morphological transition from μc-Si:H (low silane concentration) towards a-Si:H (high silane concentration) is possible by simply increasing the silane feedstock gas flow at a fixed total gas flow.

Similar morphological transitions are observed by varying the injected plasma power deposition pressure or the substrate temperature.

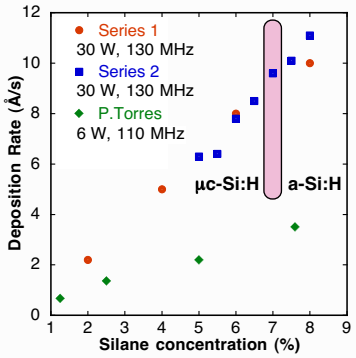

Fig. 1.3: The deposition rate increases with an increase of the SC; linear fit on two dilution series of the author under same plasma conditions compared to another series of Torres et al. [87] at lower plasma power and frequency.

The author fabricated a 'dilution series' which earned wide interest of several members of the IMT Neuchâtel and the Prag research groups. This series consists of a variation of SC for absorber films on glass on one hand and a variation of SC for the absorber layer within the operational solar cell on the other hand. The most care was taken not to vary any other parameter except for silane concentration of the absorber layer. A large number of interesting characterisations permitted further comprehension of thin-film silicon solar cells.

This parallel development of both films and cells is important since some characterisation techniques can not be applied to solar cells[1] but only to films. The couple of functional cells and of the intrinsic films on glass are fabricated at exactly the same deposition conditions. This design of experience bears many comparative information.

The complete series consists of pairs of cells and films fabricated at a silane concentration (SC) of 5%, 5.5%, 6%, 6.5%, 7%, and just films for SC

[1]For instance the sub-band absorption can not be easily measured on a n-i-p device because the doped layers and because the back-contact would disturb the results, the measurement is, thus, made with an intrinsic film deposited on glass.

of 7.5% and 8%. The cells were deposited on sputtered ZnO and on ZnO deposited by LP-CVD (low pressure chemical vapour deposition), the films were fabricated onto glass, sputtered ZnO and polished silicon wafers. The SC range between 5% and 8% contains a transition zone from μc-Si:H to a-Si:H and is the most interesting zone to explore since so far the best solar cells (microcrystalline and amorphous) are fabricated close to that transition.

The silicon absorber film must satisfy two main requirements: first a maximum optical absorption of the incident light spectrum and second optimum electronic transport properties. The absorption aspects are presented in the following section, the electronic aspects in the section thereafter.

1.2.1 Absorption measurement set-up

At first sight, a 2μm thin microcrystalline silicon film deposited on glass at 5% silane concentration (SC) has a grey or milky surface (a good sign for a natural surface texture above a Root Mean Square value RMS of 20 nm) and a film deposited at 8% has a mirror-like flat surface and is amorphous. This difference in surface roughness shows just one of the many fundamental differences between μc-Si:H and a-Si:H films, as for instance the optical reflection (see Fig. 1.4).

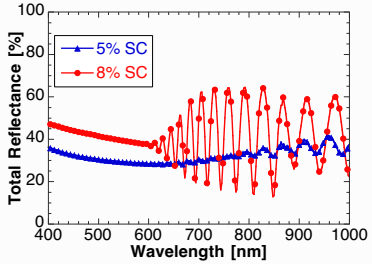

Fig. 1.4: Total optical reflectance (R) measured on a naturally growth-textured μc-Si:H film on glass deposited at 5% silane concentration and on a flat amorphous silicon film on glass deposited at 8% SC.

The commercially available Perkin-Elmer photo-spectrometer type Lambda 900 with integration-sphere was used for a first optical characterisation by measuring total and diffuse reflectance, total and diffuse transmittance for a spectral range within 320 nm-1200 nm; thus, the spectral range of Ultra Violet up to the VISible range, abbreviated 'UV-Vis' is covered.

More precise optical measurements for sub-band absorption have been achieved by using the Constant Photocurrent Method (CPM, introduced by Vanecek et al. [94]). The CPM measurement is based on the photoconductivity which is related to the generation rate by a power law. Assuming an uniform absorption (for $\alpha \cdot d \ll 1$) the generation rate is approximately proportional to $\alpha \cdot \Phi$ where Φ is the incident light flux; in CPM the photoconductivity and therefore also the the product $\alpha \cdot \Phi$ is kept constant during the measurement by adjusting the light intensity; under these conditions we have $\alpha \sim \frac{1}{\Phi}$. For the measurement, two coplanar aluminium contacts are evaporated on top of the silicon film at a certain interelectrode spacing, this spacing may vary between 30 μm and 3 mm and influences in this way the contribution of the scattered light to the bulk absorption. A more detailed description of the CPM technique is found for instance in [93].

CPM measurements allow for a determination of the absorption coefficient α over five orders of magnitudes. Because of this large dynamic range of CPM, a better evaluation of the sub-bandgap part of optical absorption

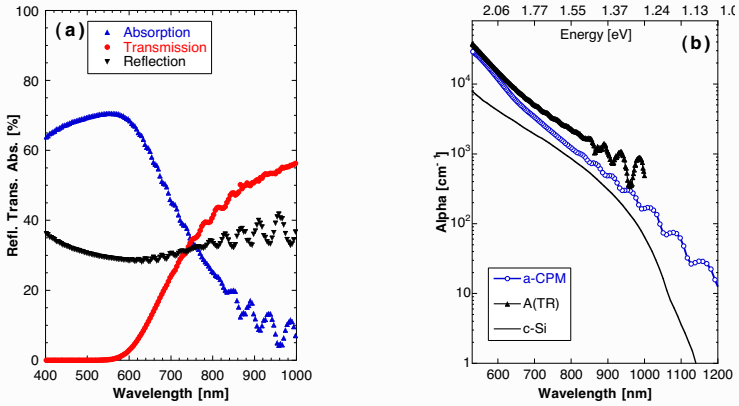

Fig. 1.5: (a): Reflectance (R), Transmittance (T) and Absorptance (A) of the 5% μc-Si:H film measured with an integration sphere. (b) The calculated absorption A(R,T) based on R and T of the same 5% film compared with the measured CPM and as a reference the c-Si wafer (ref. Keevers and Green[39]); x-axis with energy units at the top (eV) and wavelength units (nm) at the bottom.

spectra related to the defect states within the energy gap is possible. A low defect density is a prerequisite for device grade material and thus a necessary condition for fabricating high efficiency solar cells made with μc-Si:H material. These sub-bandgap absorption measurements are a good check for the capability of μc-Si:H layers that are to be incorporated into devices.

1.2.2 Absorption measurements

Fig. 1.5(a) shows the two ways of presenting the absorption. Commonly UV-Vis plots are presented in function of the wavelength whereas CPM plots are presented often in function of energy units on the x-axis (as is often done in spectroscopy); both x-axis units are utilised in Fig. 1.5(b). The absorption coefficient based on UV-Vis data (*calculated* according to equation1.1) is compared with the *measured* absorption coefficient based on CPM data, and the data of crystalline silicon [39]. Note the mismatch of the curves in the long wavelength region, due to a low precision of the equation 1.1 as soon as multiple reflections at the interfaces become too important.

The UV-Vis measurement in Fig. 1.5(a) on μc-Si:H material can be subdivided into two intervals, namely the strong absorption region (ranging from 320 nm up to 650 nm) and the weak absorption region (above 650 nm). This second interval may extend into sub-band gap absorption, depending on the measurement method: the detection limit of UV-Vis is about $\alpha \approx 100\text{cm}^{-1}$, whereas the CPM method detects up to a limit of about $\alpha \approx 0.1\text{cm}^{-1}$ [11].

1.2.3 Absorption coefficient α

The absorption coefficient α can be calculated with equation 1.1 based on measured reflectance and transmittance data obtained from the UV-Vis spectrometer; see also Beer's Law[9].

$$\alpha = -\frac{1}{d} \cdot \ln \frac{T}{1-R} \tag{1.1}$$

This method of determining α can only be applied to the spectral region of strong absorption (here up to a wavelength of λ=650 nm), as previously described. The remaining part of the spectrum up to the optical gap at 1109 nm or 1.12eV of μc-Si:H material can be measured more precisely by the CPM method[26].

1.2.4 Defect densities

It has been shown that the apparent optical absorption coefficient α_{app} as measured by CPM overestimates the true (or material intrinsic) absorption

coefficient α_{true} by a factor 10 to 12 in the sub bandgap region[66]. This too high value of α_{app} can be traced to various light scattering effects (mainly due to natural surface texture and also to a bulk scattering contribution) of the silicon films as reported by Poruba et al. [66]. In consequence true absorption would be a factor 10 to 12 lower than plotted in Fig. 1.6 because of maximal enhancement due to light scattering in these samples of the dilution series.

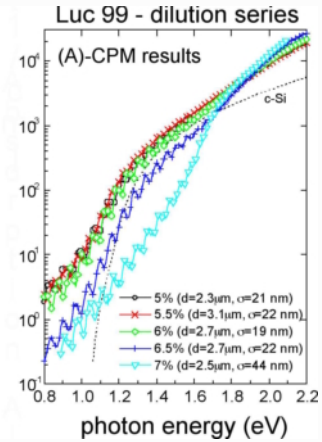

Fig. 1.6: Apparent absorption coefficient α_{app} as measured by absolute CPM on films of the dilution series; source: [67].

SC [%]	Apparent $\alpha_{0.8}$ [cm^{-1}]	True $\alpha_{0.8}$ [cm^{-1}]
5.0	3	0.3
5.5	3	0.3
6.0	2	0.2
6.5	4	0.4

Table 1.2: The defect-connected absorption $\alpha_{0.8}$ of films deposited at various Silane Concentrations (SC); calculations based on apparent CPM data, including correcting for the surface roughness.

An interpretation of the measurements of the dilution series from the point of view of the true defect-connected absorption $\alpha_{0.8}$ at the energy 0.8 eV yields that all samples seem to be similar within the precision of the method, see also the data in Table 1.2. The best sample is deposited at SC of 6.0% but has a high amorphous volume fraction of some 50%, see also Fig. 1.8(b) with more Raman spectroscopy data. The 7% SC is not usable because of a non-homogenous surface of partially very rough μc-Si:H material mixed with flat surface regions. All samples have about 10 times higher defect density than the best sample of a former series (5% SC and 12 W plasma of a power series[100]); but the here presented samples were deposited at much higher growth rates ranging from 6.3Å/sec up to 9.6Å/sec.

What concerns the crystalline fraction of the series, it can be noted that

samples 5%, 5.5% and 6% SC are 'fully' microcrystalline whereas sample 6.5% and 7% have a large amorphous fraction; there will be more on the crystalline volume fraction in section 1.3 on Micro-Raman spectroscopy.

Defects in μc-Si:H thin films can probably come from various sources, such as

- grain boundaries with dangling bonds that are not passivated by hydrogen
- oxygen and other impurities (like contaminations from preceding doped layers, e.g. in a single-chamber deposition system).

In the second case there is also a detectable influence on the dark conductivity σ_{dark}, see section 1.4. More information on the hydrogen incorporation (thus, the hydrogenating of dangling bonds) within the film as detected by Infra-Red spectroscopy is given in section 1.5.

Special note: Within the analysed dilution series, the best film quality with regards to defect density is found to be deposited at a SC of 6.0% whereas the best conversion efficiencies within the dilution series yield a maximum value of η=5.5% at a silane concentration of 5.5% without any back-reflector (see also chapter 9). The usual care is thus necessary if a layer series is compared to a series of intentionally *similar* cells: since the solar cell is not just an assembling of several doped and undoped layers, but also interfaces, the matching of different material's growth structures and electronic potential play an important role. In general, one can observe similar tendencies on the layer and the cell series, but evidently the best layer quality does not result inevitably in the best conversion efficiency. As an example, there is a trend for layers to grow more amorphous with increasing SC (see Fig. 1.8) but the crystalline volume fraction measured on a layer deposited at 6% SC on glass will not match the crystalline volume fraction of the solar cell deposited at 6% SC because of the different initial growth condition of the intrinsic film in the two cases. In fact the layer grown on glass has the tendency to be more amorphous, see also the section 8.1.2 on the n-i interface of cells.

1.2.5 Interference fringes

Interference fringes in transmittance and reflectance data are rather disturbing for the accurate calculation of the absorption[2]. Nevertheless these fringes

[2]If the minima and maxima of the fringes in reflectance and transmittance data do not fall to exactly the same wavelength, a certain error is introduced. In practice this may

may bear some additional information on the nature of the film if evaluated consciously:

- Swanepoel showed a method for the determination of the film thickness and/or the refraction index based on the interference fringes of optical measurements [82].
- We present here a new interpretation of the interference fringes transmittance measurements on thin films (for both textured and flat surfaces) which yields information on the natural texture of the film surface roughness.

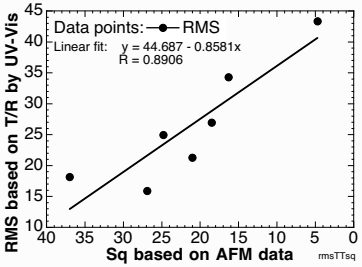

Fig. 1.7: A linear correlation between the RMS of the interference fringes of transmittance and the surface roughness Sq (definition: see page 132) determined by AFM (see section 1.6) of the dilution series films.

A straight-forward correlation between the fringes in UV-Vis transmittance measurements and the surface roughness measured by AFM is possible: The Root Mean Square (RMS) of the optical transmittance (T) data gives us information on the nature of the fringes (i.e. on their amplitude). On the other hand, Atomic Force Microscopy (AFM) scans on the surface of the films gives us the Sq value of the natural surface texture[3]. If the optical RMS value is computed for each film of the dilution series and is then plotted in function of the film's Sq value, a linear dependence may be observed, as

occur if the reflectance and the transmittance are not measured at the same place on the film.

[3]Here the abbreviation RMS and Sq are both used for the value of a root mean square roughness. The first describes the shape of an optical transmittance curve and the second is an expression of a surface topography measured by AFM. See the definition on page 132.

shown in Fig. 1.7: The smoother the film surface, the more pronounced are the interference fringes in transmission and the higher is the RMS value of the fringes (more AFM data is presented in section 1.6).

This simple relation has to be taken with care, since it assumes a homogenous film thickness, further more, the spectrometer measurement has to be done at a constant slit aperture. Never the less this observation of the RMS values of the dilution series films gives a qualitative correlation of surface roughness and interference fringes.

1.3 Raman Spectroscopy

The fraction of crystalline to amorphous silicon can be detected by Raman spectroscopy, and this crystalline fraction varies in function of the silane concentration in the fabrication process. Raman spectroscopy was performed on the material of the dilution series of intrinsic films: In this section, results of the investigations of the crystallinity of the films on glass are reported, for a complete study of the crystallinity on layers *and* solar cells of the dilution series see Droz et al. [16].

The Raman spectra in the range from 400 to 550cm^{-1} were deconvoluted with three gaussian peaks and a quadratic background, with an algorithm based on the Levenberg-Marquardt method[56]. The peak centered around 520cm^{-1} characterises the crystalline part, the peak at 510cm^{-1} is related to twinned or small crystallites (diameter smaller than 10nm [106]) finally the broad peak at 480cm^{-1} is related to the presence of a-Si:H. In equation 1.2 the value of the crystalline volume fraction Φ_C is evaluated based on these three Raman peak intensities.

$$\Phi_C = \frac{I_{510} + I_{520}}{I_{480} + I_{510} + I_{520}} \tag{1.2}$$

The crystallinity X_C as detected by X-ray diffraction (XRD) is not the same crystallinity ϕ_C as detected by Raman spectroscopy. In fact, the amorphous fraction in the material is over-estimated because of the difference in Raman cross-section of c-Si and a-Si:H and other contributions to the 510cm^{-1} line [95, 36]. See also the publication by Vanecek et al. [92] on the correlation of Raman spectroscopy, FT-IR spectroscopy and Electron Spin Resonance (ESR) observations.

If the Raman spectra are taken once from the film side and once from the glass substrate side of the 6% SC film of the dilution series two different pictures of the crystalline fraction of the same film are observed, see Fig. 1.8(a). These two viewpoints highlight a lower crystalline volume fraction for the

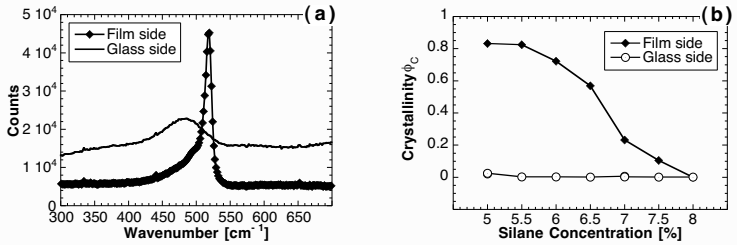

Fig. 1.8: (a) Raman spectroscopy (wavelength $\lambda_{Laser} = 514nm$) measured from the film-side and through the glass substrate of the μc-Si:H film deposited at 6% SC. (b) The crystalline fraction is strongly dependent on the silane-concentration if observed from the film side - from the glass side, no crystalline signal is detectable at all.

part of the film at the beginning of growth (substrate side) compared to a high crystalline volume fraction as observed from the film side. The penetration depth at the wavelength $\lambda_{Laser} = 514nm$ is in a-Si:H of the order of 100nm, whereas it reaches 300nm in μc-Si:H [10].

If the dilution series of films is analysed, the trend towards a reduced crystallinity for films deposited at a higher silane concentration is observed. Within the top 100nm or so of the 2μm thick film, there is a growing amorphous volume fraction and a reduced crystalline fraction, up to the complete amorphous film characteristic as observed for a SC of 8%.

In opposition to this previous observation from the film side, there is hardly any change in the fully amorphous spectra observed from the glass side. This is in our eyes evidence for the presence of an amorphous incubation layer on the substrate, and the delayed formation of crystalline silicon seeds. This means the amorphous incubation layer on the glass substrates has a thickness of 100nm or more in every step of the silane concentration series. Within the absorption depth of the laser light no crystalline trace can be detected.

1.4 Dark conductivity (σ_{dark})

1.4.1 Set-up of the σ_{dark} measure

For the dark conductivity measurement, two metal contact pads (aluminium 100 nm thick, 8 mm long, separated by 0.5 mm) are evaporated through a mask on the silicon film in order to create an Ohmic contact. The sample is then loaded into a dark vacuum chamber and connected with a Ohm-meter. The vacuum chamber is pumped down to the base-pressure ($\approx 10^{-4}$ mbar) and filled up again with nitrogen (N_2) to a level of 10 mbar, in order to perform the measurement in a controlled atmosphere without the presence of oxygen. The measurement itself consists of a rapid heating ramp to the annealing temperature of the sample (as a rule of thumb: deposition temperature minus 20°C), then a period of constant temperature for a full annealing of the contact, and finally a constant rate cooling ramp of 0.8°C per hour down to room temperature; in this third phase, the actual dark conductivity is measured. This program of three cycles allows the measurement of the specimen in an annealed and, thus, electronically well defined state.

1.4.2 Results and discussion

The dark conductivity and activation energy (E_{act}) is finally extracted from the Arrhenius plots (σ_{dark} in a logarithmic scale as a function of 1000/temperature in Kelvin) for films deposited in the dilution series in Fig. 1.9(a). The slope of the obtained curve yields the activation energy, assuming a

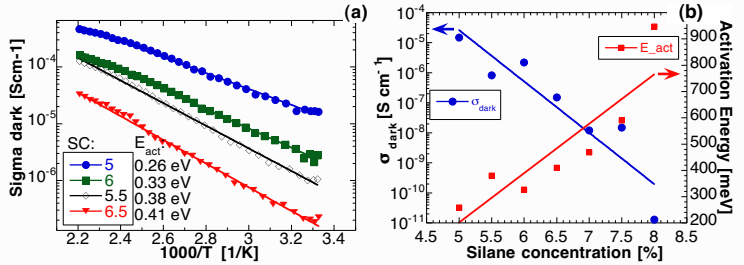

Fig. 1.9: (a) Arrhenius plots of dark conductivity σ_{dark} measurements of layers of the dilution series and (b) evaluation of activation energy and σ_{dark} in function of silane concentration.

simple thermally activated transport model. In Fig. 1.9(b) the activation energy and dark conductivities are reported in function of the film's silane concentration.

Basically, σ_{dark} and E_{act} are influenced by two factors

1. A higher amorphous volume fraction tend to lower the value of σ_{dark} and increase the value of E_{act}.

2. A higher impurity content (oxygen and other dopant-like impurities) tends to increase σ_{dark} and lower E_{act}.

A typical value of $\sigma_{dark} < 10^{-6} Scm^{-1}$ on one hand and an activation energy $E_{act} \approx 550\ meV$ on the other hand are the signature of a μc-Si:H material with truly intrinsic character, i.e. with the Fermi level E_F at midgap, a condition that is necessary for solar cell absorber material.

However the interpretation of these measurements is delicate because of the following reasons:

1. **Post-oxidation**: The value of σ_{dark} can be influenced by the effect of oxygen incorporation into the μc-Si:H film which disturbs the initially intrinsic character of the film. The presence of oxygen in the $< i >$ type films is undesirable because of the donor character of oxygen (n-type doping) in silicon. This post-oxidation occurs inevitably after unloading the sample from the deposition chamber for further processing and measurements. Basically the oxidation is proportional to the time of exposure to the ambient atmosphere and oxidation increases exponentially with the temperature of the film.

2. **Sensibility to post-oxidation**: Films of a high degree of crystallinity may oxide more than films at the transition to the amorphous growth regime. The highly textured surface may increase even more the surface oxidation. Further oxidation may occur because of small cracks along the crystalline grains of certain μc-Si:H films; cracks were observed by TEM [96]. These facts are potentially increasing the post-oxidation of intentionally intrinsic films.

Thus, several μc-Si:H films which have too low an activation energy (e.g. $E_{act} < 550meV$) might have been initially intrinsic but may have suffered from post-oxidation. The difficulty to make a correlation between transport properties and solar cell efficiency illustrated in Fig. 1.10 where the conversion efficiency of μc-Si:H solar cells of the dilution series (see chapter 9) are reported against the product of the $\mu^\circ \cdot \tau^\circ$, (mobility times lifetime of corresponding individual layers). This expression is widely used in the area of

a-Si:H solar cell and thin-film research [11, 27], its application to the μc-Si:H material seems to be more difficult. Even though this method may be used for a first exploration of film quality before fabricating an actual device, it is our opinion that many researchers have spent too much time on $\mu^\circ \cdot \tau^\circ$ product and forgot about the main topic of *fabrication* of solar cells.

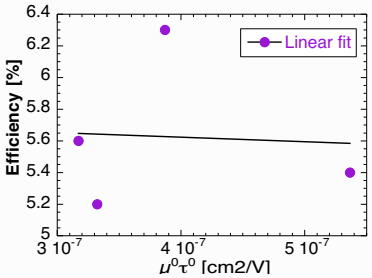

Fig. 1.10: The product of mobility times lifetime, a figure of quality widely used in a-Si:H research, can not be applied reasonably to correlate μc-Si:H film quality and conversion efficiency of solar cells.

1.5 FT-IR spectroscopy

1.5.1 Set-up of the FT-IR measure

Fourier Transform Infra Red (FT-IR) Spectroscopy gives information on the atom-bonding vibration modes occurring in amorphous and microcrystalline silicon films. The absorption spectra reveal peaks which can be identified with hydrogen bonds like the Si-H rocking-wagging mode at 640cm^{-1} but also the peaks at 900cm^{-1} and 2101cm^{-1} are of interest. See the references [7, 70] for a in-depth discussion on FT-IR spectroscopy.

A Perking Elmer FT-IR 1720X spectrometer was used to measure the absorption spectra between 4000cm^{-1} and 400cm^{-1} of the thin films deposited on double-side-polished p-type $< 100 >$ silicon wafers. The hydrogen content C_H was obtained by numerical integration of the Si-H rocking-wagging mode at 640cm^{-1}. The complete procedure is well described by Kroll et al. [45]. As the authors point out, this evaluation method is valid for the estimation of the hydrogen content of thin silicon films of both amorphous and microcrystalline phase.

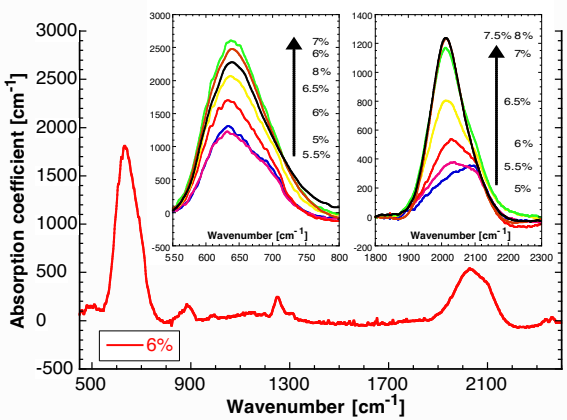

Fig. 1.11: The FT-IR plot of the silicon film deposited at 6% SC, the inlays show the evolution with an increase of silane concentration of the two peaks centered at 640cm^{-1} and 2100cm^{-1} respectively.

1.5.2 Results and discussion

The whole infrared spectrum of the film deposited at 6% is shown in Fig. 1.11 and the two inlays show the evolution with silane concentration of the two peaks centered at 640cm^{-1} and 2100cm^{-1} respectively, which show the main evolution: with an increasing SC the peak centered at 640cm^{-1} becomes more important and a shift of the peak centered at 2100cm^{-1} towards the a-Si:H related peak centered at 2000cm^{-1} is observed. This shift is often reported in the literature and seems to be a reliable indication of a phase transition from amorphous to microcrystalline material deposition conditions [89, 45].

For the determination of the hydrogen content C_H by FT-IR spectroscopy the Si-H rocking-wagging mode at 640cm^{-1} was numerically integrated. The measured C_H values of the here presented μc-Si:H dilution series lie between 6 and 14 atomic percentage [at.%]. As shown in Fig. 1.12 there is good agreement with the data of the earlier series by Kroll et al. [45].

Rather puzzling is a systematic mismatch of C_H when measured in intrinsic films as compared to the C_H when measured in complete n-i-p devices: our standard solar cell deposited around 5% SC has a C_H of only 3.8 at.% whereas device grade intrinsic films should have a C_H around 5 at.%, see Fig. 1.12. The higher absorption coefficient in the infrared of doped n-type an p-type films compared to the intrinsic material may be an explanation of this difference.

Interesting to note are the observations by Vanecek et al. [92] where a stepwise annealing from 380°C up to 690°C in an oxygen-free atmosphere

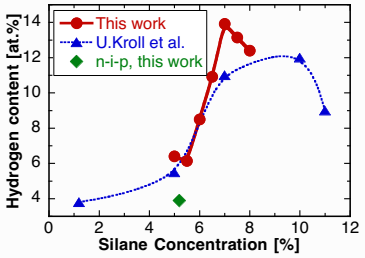

Fig. 1.12: The hydrogen content of two different dilution series follow the same trend; also indicated is the surprisingly low C_H-value of a standard n-i-p solar cell.

has been done on μc-Si:H films. Hydrogen desorption is observed in infrared spectrometry at the typical μc-Si:H peak at 2100cm^{-1} as well as at the 630cm^{-1} peak and at the doublet between 800cm^{-1}and 900cm^{-1}. Simultaneously with the effusion of hydrogen, the absorption coefficient α at photon energy 0.8 eV increased from the range of 0.06 - 0.3 to the range of 50 - 120cm^{-1} this being a sign of a defect-related optical absorption.

In connection to the post-oxidation effect of section 1.4 it may be interesting to note that Flückiger observed by FT-IR measurements an increased post-oxidation only for layers deposited below a deposition temperature of 220°C. Films deposited above that temperature contain less hydrogen, seem to be less porous and suffer less from the post oxidation effect.

1.6 Atomic Force Microscopy

1.6.1 Set-up of the AFM measure

With an atomic force microscope (AFM) the surface of a sample is scanned by a cantilever onto which a small tip is mounted. This cantilever is moved in the x-y direction by a stepping motor whereas the z-direction is actuated by a piezo-electric device. The tip follows the topography of the sample and communicates every change in the z-direction to the cantilever. These small z-movements are measured optically by interferometry. In this work, a Burleigh Vista 100 AFM was used in contact mode.

1.6.2 Silicon seeds in function of deposition temperature

The question on initial nucleation of silicon films at the growth interface is a central point in cell optimisation, since at least three films have each to start to grow and form a new interface (n-type on TCO, i-type on n-type and p-type on i-type).

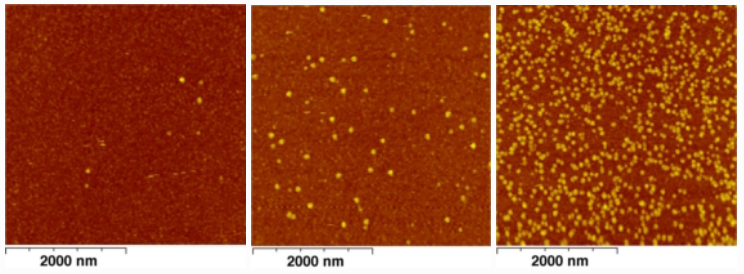

Fig. 1.13: AFM images of three 100nm thin μc-Si:H seed layers deposited on glass at successive temperatures: 200°C, 250°C, 300°C.

A μc-Si:H film starts to grow first at a nucleation site and develops a conical 'cauliflower' shape which fills the entire surface at the end of the 2μm thick whole film growth. At the initial growth interface between the substrate and μc-Si:H, these seeds are embedded in a tissue of amorphous silicon[40]. The density of these first nucleation sites depends (among other deposition conditions) on the deposition temperature, see Fig. 1.13 where 100 nm thin microcrystalline films were fabricated on glass at three different

temperatures. For all films (L051099G), a silane concentration of 6% was chosen at a deposition rate of 7.8 Å/sec.

The three seed films reveal the following statistic fingerprint: the root mean square (Sq) of the surface roughness, the Peak to Valley (P/V), skewness and kurtosis of the scanned profile as well as the counted number of particles are reported in Table 1.3; all three AFM scans were made on a square of 4μm side length.

Table 1.3: Statistics of AFM scans on seed layers in function of the deposition temperature: surface roughness Sq, Peak to Valley (P/V), Skewness, Kurtosis (see page 132 for exact definitions) and counted number of particles.

Temp [°C]	Sq [nm]	P/V [nm]	Skew.	Kurt.	Particle number
200	1.8	20.24	1.46	11.48	11
250	2.57	31.59	3.07	18.17	71
300	5.5	31.11	1.01	2.87	578

The interpretation of these three AFM scans is at first a low nuclei density for low temperatures and an increasing density for higher temperatures. This can be well explained with the higher formation energy of crystallites compared to a lower activation energy to form the amorphous tissue. For 'more amorphous' growth conditions (such as a higher SC or low plasma power) this amorphous tissue can form a continuos film which is often referred to as an incubation layer. If such an amorphous incubation layer is too thick, it may hinder good solar cell performance. The nucleation layer can be detected by Raman spectroscopy, see section 1.3, or by TEM, see section 1.6.4.

1.6.3 The edge of an n-i-p device

This investigation was focused on the microscopic resolution of the solar cell in growth direction and not on the surface orthogonal to the growth direction, in order to see the μc-Si:H grains not from top view but from a side view. For this purpose, a finished and functional solar cell was cut in two pieces which then were pressed into plasticine. Doing so, the edge of the cell was accessible on one side of this plasticine disk of about one inch diameter. The plasticine surface was metallurgically polished: first a coarse-grained and later a very fine grained polishing paper was used. Within the flat polished plasticine surface the structure ZnO-n-i-p-ZnO is polished at the same level.

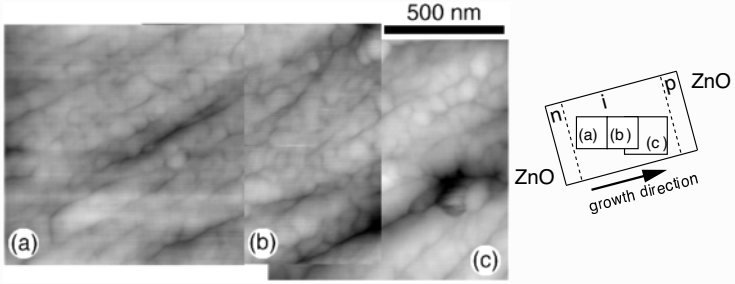

Fig. 1.14: AFM picture of three successive scans of a microcrystalline solar cell: n-side at the left border of the picture and the p-side at the far right border and the growth direction is indicated in the sketch.

The n-i-p cell structure sandwiched between the two TCO layers is observed first by an optical microscope (in order to check the absence of remaining scratches due to the polishing procedure) and then by atomic force microscope. Note that the sample is exactly in a rectangular position with respect to the picture frame, but that a 'shearing' took place during the sample preparation.

These images give a first evidence of microcrystalline silicon microstructure of two different sizes, see Fig. 1.14. The large columns (with column height in the order of a micrometer) are in fact composed of small spherical grains (diameter in the order of 10nm). This observation of the columnar structure is in perfect agreement with SEM pictures where these 'cigar' shaped columns are close to the detection limit. Between the apparent boundaries of the columns the presence of cracks can be noticed. Cracks are often suggested to be responsible for an increased post-oxidation of the μc-Si:H films and, thus, for a poor device performance. They are speculated to be also responsible for shunts and, thus, for a reduction in V_{OC} and fill-factor of solar cells.

The presence of the small granular grains is in agreement with the results of calculations of the grain size by the Scherrer formula[4] based on X-Ray Diffraction data[28]. Recent observations show that the columnar grains are actually a conglomerate of the small grains, thus the large grains are made of the small granular grains.

[4]The Scherrer formula, permits the determination of the grain size based on the size of the XRD diffraction peak.

The polishing procedure of the solar cell on glass and the surrounding plasticine results in a not perfectly flat but a slightly curved surface of the edge. This difference in height between the center of the cell (i-layer) and its interfaces (ZnO-doped layers) unfortunately hides the interesting borders of the cell because the limited z-resolution of the AFM gets out of range.

1.6.4 Incubation layer or mixed-phase layer?

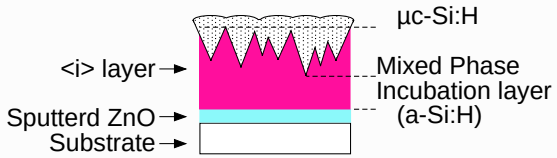

Fig. 1.15: Sketch of the nucleation zone of a μc-Si:H film.

The term 'incubation' layer is currently used in the context of nucleation and crystalline growth, but it is sometimes not referred to exactly the same observations, thus, creating rather confusion than a clear usage of language. We prefer to apply the definition like originally used in medical science, where it describes the period between infection (e.g. by bacteria) and the appearance of the first symptoms[5].

The situation of silicon film growth is sketched in figure 1.15. Looking at the evolution of the layer thickness, the phase before "infection" (i.e. the appearance of crystalline grains) is observed to contain an amorphous phase. This first continuous amorphous phase is the incubation layer, then there is a phase of a mixture of amorphous and crystalline silicon, the so called 'mixed-phase'. After a long enough growth, the formerly isolated crystalline nuclei join each other, a competition of several grains leads finally to a continuously formed μc-Si:H film.

This definition of the term 'incubation' layer refers *exclusively* to the amorphous phase, as observed by TEM in Fig. 1.16 where a silicon film of 7% SC is deposited onto a sputtered ZnO layer. On top of the dark ZnO film at the bottom of the micrograph, a homogenous part (grey) can be seen which is identified with the amorphous incubation layer. Only about 100nm above the ZnO layer, first crystalline grain formation are observed, this is

[5]Definition taken from 'Oxford Dictionary of Current English' by A.S. Hornby.

the beginning of the mixed-phase, up to the part at about 700nm thickness, where a continuous microcrystalline film is observed.

For a discussion on the growth of solar cells on different back-TCO and the difficulty fabricating very thin and very crystalline doped films, see also section 8.1.2.

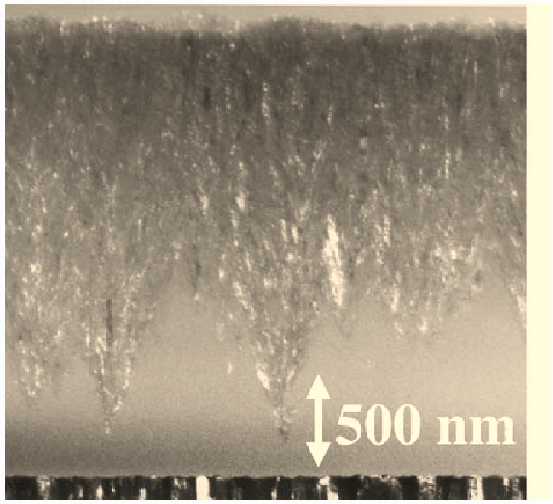

Fig. 1.16: TEM bright field micrograph of a μc-Si:H film deposited at 7% SC onto sputtered ZnO (at the bottom): after the incubation layer, nuclei start forming (mixed-phase) then finally a continuous microcrystalline film in the upper half of the micrograph is observed; source: Bailat et al. in ref. [3].

1.7 Optical Emission Spectroscopy

1.7.1 Set-up of OES

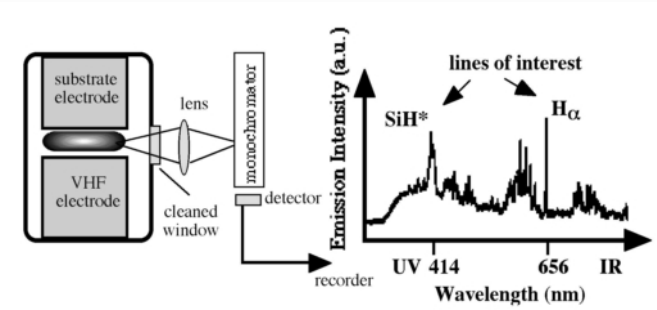

Fig. 1.17: Experimental set-up for measuring the optical emission spectroscopy (OES) with a typical spectrum. The emission lines of interest are at a wavelength λ=414nm and at λ=656nm; these lines are attributed to the emission lines of the SiH* radical and to the atomic hydrogen (H_α), respectively.

The plasma deposition is a combination of chemical and physical processes and its interactions. This interaction process as such can be approximated by complex formulae, as for instance in the publication by Kushner using 229 equations[42]. Still, the link between such descriptions of the plasma with the resulting material quality or even solar cell conversion efficiency could not been established so far.

In short, gas molecules are dissociated by the injected RF-power. Radical ions, formed by this dissociation, are then accelerated in the E-field and processes such as deposition and ion attack may occur[50].

Plasma characterisation by Optical Emission Spectroscopy (OES) is a real-time tool for a simplified characterisation of the plasma processes, see Fig. 1.17: In the plasma many transitions from high energy levels to low energy levels of electrons take place, thus electro-magnetic radiation is emitted. A part of this radiation in the visible range may be detected with appropriate sensors and may give insight into the reactive species involved and may also help to clarify the reaction mechanisms. In the context of thin-film silicon deposition by PE-CVD, the emission lines of SiH* and H_α are of special interest; they are identified at wavelengths λ=414nm and 656nm, respectively.

Torres et al. [88, 89] showed that the ratio of these two emission line intensities $\frac{SiH*}{H_\alpha}$ can be used to determine the microstructure of the deposited film, see Fig. 1.18. The figure shows the transition of phase for a variation in silane concentration and a variation in injected plasma power. This observation is used in section 1.8 for monitoring the evolution in time of a special plasma condition.

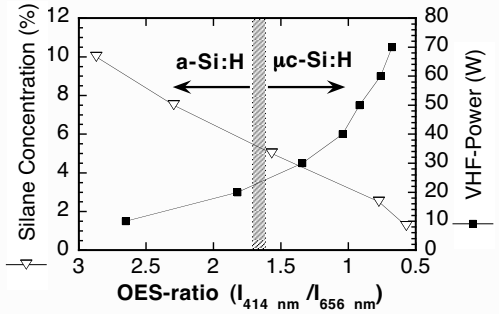

Fig. 1.18: OES measurements on a PE-CVD reactor operated at 110MHz plasma excitation frequency: The ratio of the emission line intensities of SiH* and H_α indicates in real-time the growth condition (whether a μc-Si:H or an a-Si:H) of the plasma, source: P. Torres[89]

Another observation is the scaling of the SiH* emission line intensity with the deposition rate independently of the material type of the layers (e.g. a-Si:H or μc-Si:H). Thus, OES is an efficient and easy to handle in-situ process control tool that can certainly contribute to monitor deposition processes.

1.8 Closed Chamber Plasma

The investigations presented in this section contributed to the PVSEC-12 conference in June 2001 on Cheju island, Korea [20].

Plasma Enhanced Chemical Vapour Deposition (PE-CVD) is commonly used to produce amorphous (a-Si:H) and microcrystalline (μc-Si:H) silicon thin-film solar cells [19]. Parameters like hydrogen dilution of silane feedstock gas, plasma power, deposition pressure, etc. strongly influence the plasma reaction and, thus, the characteristics and quality of the deposited film. In contrast to the conventional PE-CVD deposition process, the closed chamber plasma presented here can be characterised by the following points:

1. The absence of hydrogen feedstock gas.
2. A low silane feedstock gas supply.
3. The absence of a gas purifier.
4. A low gas extraction out of the vacuum chamber which is almost in closed chamber condition.

For the growth of microcrystalline silicon films we used AF45 Schott glass substrates at a temperature $T_S = 270°C$, no hydrogen gas flow at all, silane gas flow of up to 3 sccm at 0.1 mbar, no gas purifier, an injected plasma power of up to 30W, and a VHF plasma excitation frequency of 130 MHz. These are similar parameters as those proposed by Matsuda et al. [49] and we call it a *static closed-chamber* process (SCC VHF-GD), in contrast to the cyclic process proposed by Koynov et al. [44]. There is no cycling between two deposition regimes like in the layer-by-layer method, but a steady and constant process and, thus, a *static* process. The deposition chamber is therein not fully isolated but small quantity of used gas is pumped out. A specially interesting aspect is the formation of microcrystalline silicon in the absence of any hydrogen feedstock gas dilution; to our knowledge for the first time, such material is used as absorber layer in n-i-p type solar cell devices. In this section, we report on the transient behaviour of the SCC VHF-GD plasma and its in-situ monitoring by OES.

1.8.1 Kinetics monitored by optical emission spectroscopy: comparison of closed chamber conditions and standard VHF conditions

The Optical Emission Spectroscopy (OES) technique has been used by us to characterise the temporal evolution of a pure silane plasma in the first

90 seconds after ignition of a Static Closed-Chamber Very High Frequency Glow Discharge (SCC VHFGD). Special interest is drawn to the formation of microcrystalline silicon (μc-Si:H) in the absence of any hydrogen feedstock gas dilution. The kinetics of the emission lines of SiH* and H_α are reported here. The deposited films are characterised by Photothermal Deflection Spectroscopy (PDS), Fourier-Transform Infra Red absorption (FT-IR); they show typical microcrystalline fingerprints.

1.8.2 Results: OES

In the first 30 seconds after ignition, a high intensity of the SiH*-line and a low intensity of the H_α-line is observed (see Fig. 1.19). This is identified with a pure silane plasma without any noticeable hydrogen precursors, as one should expect from the deposition conditions (no hydrogen dilution).

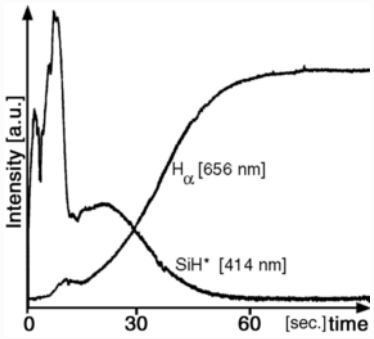

Fig. 1.19: Temporal evolution of the emission intensities (measured with OES) of the hydrogen and silane lines, respectively. More and more hydrogen is dissociated in the pure silane gas phase during the first 90 seconds just after the plasma ignition. See [21] for a quick-time movie of this evolution.

Then in the next 30 seconds, the emission intensity of the H_α-line gradually becomes more pronounced. This is explained by a dissociation of the SiH_4 gas molecules: The growth of the film consumes Si-atoms, the low silane flow permits only a reduced gas phase regeneration and, therefore, dissociated H-species start populating the plasma reaction. An increasing amount of H-species is generated by the dissociation of the depleted plasma and a much lower ratio of the [SiH*]/[H_α] emission is observed.

Steady conditions for the plasma can finally be observed after 60 seconds. A balance of SiH* and H_α species is then achieved, conditions for microcrystalline growth are established and the typical OES-fingerprint for a microcrystalline growth (ratio of the [SiH*]/[H_α] below unity) may be observed. In agreement with observations previously reported in the literature, μc-Si:H growth is indeed observed as soon as enough atomic hydrogen is available[55, 63]. The bulk of the film deposition is made in this plasma condition.

1.8.3 Solar grade material and solar cells

Table 1.4: Hydrogen content C_H as integrated from the 640 cm^{-1} peak of FT-IR absorption spectra of μc-Si:H films fabricated by the two different deposition methods

Static cc-GD		**Standard VHF-GD**	
SiH_4-flux	C_H	dilution [%]	C_H
[sccm]	[at.%]	$SiH_4/(SiH_4+H_2)$	[at.%]
1	3.8	5.5	6.1
2	4.6	6.0	8.5
3	7.8	6.5	11.0

Similar to the dilution series by conventional PE-CVD a transition from microcrystalline to amorphous deposition conditions can be observed by the SCC VHF-GD method if the silane gas flow is increased from 1 sccm to values above 3 sccm. Films deposited at 1 sccm silane flow are composed of a high crystalline volume fraction whereas films deposited at 3 sccm silane flow tend to incorporate less crystallites and more amorphous material. The increase in deposition rate from 1.5 Å/sec up to 5.8 Å/sec for an increase of the silane flow between 1 sccm and 3 sccm confirms the trend towards an amorphous growth regime. In other words, a phase transition from μc-Si:H towards a-Si:H is possible in the closed-chamber process without the use of any hydrogen feedstock gas dilution but by simply increasing the silane feedstock gas flow.

Infrared absorption measurements on the deposition layers reveal a close relation between the flow of fresh silane gas introduced into the closed-chamber and the hydrogen content C_H (see Table 1.4). FT-IR spectroscopy data of the Si-H rocking-wagging mode centered at 640 cm^{-1} was numerically

integrated, see also section 1.5. These C_H values lie between 4 and 8 atomic percentage [at.%] for the SCC VHF-GD material. Such values correspond very well to these obtained for layers deposited in the standard VHF-GD process at a silane dilution around 5%, see also Fig. 1.12.

The shape of the absorption spectra see Fig. 1.8.3) of the μc-Si:H layer deposited by SCC VHF-GD follows the parabolic shape of c-Si [39] over a wide range of energy, and is shifted to lower energies and higher absorption values. Both, the enhancement and the shift of the absorption edge are typical characteristics of device-grade μc-Si:H material, which occur for both deposition methods observed so far in our lab i.e. for standard VHF-GD and here for SCC VHF-GD. Despite the higher subband absorption of the new material this encouraging results motivated us to investigate further in this novel deposition method.

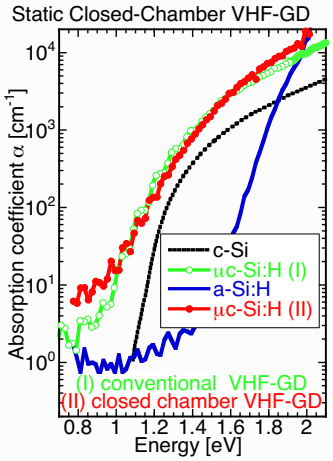

Fig. 1.20: Absorption of the film fabricated by the CC-VHF method (II) compared with a standard μc-Si:H film produced by 'conventional' PECVD (I); for comparison, typical absorption of a-Si:H and c-Si (wafer) material is indicated.

The best solar cell fabricated so far by the proposed closed-chamber method has a conversion efficiency of η=2.5%, an open-circuit voltage of 419mV, a fill-factor of 70%, a short-circuit current of 8.6 $\frac{mA}{cm^2}$ under standard AM1.5 test conditions; cell thickness of 2.2 μm. The 'device fabrication

limitations' that are specific to the closed-chamber deposition process are observed during the initial phase of the plasma. A remedy to overcome these limitations would be the introduction of a 'shutter' into the plasma chamber which prevents the deposition of an initially amorphous incubation layer and this would favour a better control of the initial nucleation on the solar cell. For more detailed solar cell results and fabrication by the 'conventional' PE-CVD deposition method, see sections 8.4 and 8.3.

In conclusion, the initial phase of the plasma is documented by monitoring the kinetics by OES of the SCC-VHF deposition method, where a transient behaviour is found. Other characterisation methods like infrared spectroscopy and PDS absorption measurements failed to give evidence for the presence of an incubation layer, only Raman spectroscopy showed the presence of the amorphous incubation layer, if the substrate side and the film side illumination are compared.

The SCC-VHF method reduces considerably the amount of necessary silane feed stock gas: To fabricate a μc-Si:H film by the VHF method a value of 21000 sccm·sec is necessary (thickness 2.2 μm, deposition rate: 7 Å/sec) whereas only 10800 sccm·sec are needed for a film deposited by the SCC-VHF method (deposition rate: 4 Å/sec). Silane consumption is halved for the deposition of device-grade absorber films with the SCC VHF-GD method compared to the standard VHF method. Since there is no need for hydrogen feedstock gas and, thus, no necessity for a gas purifier, the closed-chamber method is considered an ecologically and economically interesting alternative to the conventional plasma deposition process.

Chapter 2

Combination of Hot-Wire and PE-CVD

2.1 Introduction

In 1997, one aim at IMT was to increase deposition rates from below 1 Å/s towards 10 Å/s by using the VHF-GD technology. Several solution for increasing the deposition rate (in μc-Si:H cells) were investigated: 1. Increase of the deposition frequency from 70 MHz up to 130 MHz. 2. Increase of injected plasma power 3. Combination of VHF-GD and hot-wire (HW) deposition technique. This third option will be presented in this chapter.

The novel deposition method combines the already well investigated PE-CVD deposition process with the newly investigated Hot-Wire (HW) process by Ziegler during his PhD in our IMT research group [109, 110]. Only minor changes on the HW deposition chamber were necessary for the fabrication of μc-Si:H solar grade material at rates exceeding 25 Å/sec. At this time, all publications on the HW process focused on *a-Si:H* applications exclusively, but no other research group so far utilized the HW technique to investigate in the fabrication of functional *μc-Si:H* solar cells at such high deposition rates at that time (1997) to our knowledge.

2.1.1 The deposition system

Essentially the same vacuum chamber is utilised for the combined deposition method using Hot-Wire (HW) deposition and the Plasma Enhanced Chemical Vapour Deposition (PE-CVD) of silicon films. For the set-up of the HW technique, two electrically isolated connectors are mounted onto a flask, in order to power the tungsten wire inside the deposition chamber, see Fig. 2.1

for a schematic set-up of the deposition system and typical processing parameters.

First films were fabricated without the gas purifier. For the optimisation w.r.t solar cell absorber layers, the gas purifier was used to avoid incorporation of detrimental oxygen contamination in intrinsic μc-Si:H layers[86]. The doped layers of the solar cells were fabricated in a different PE-CVD deposition chamber; for more on PE-CVD deposition parameters, see section 1.

With HW alone we achieved deposition rates up to 35 Å/s, but not satisfying μc-Si:H material quality. The idea of the combined plasma and HW deposition method was to improve on two levels: first the deposition rate is increased compared to the conventional VHF method up to a value of 25 Å/s and second a better absorber material compared to the conventional HW method is fabricated. Since at that time, the absorber material fabricated by the HW technology was inferior to material fabricated by VHF plasma technology.

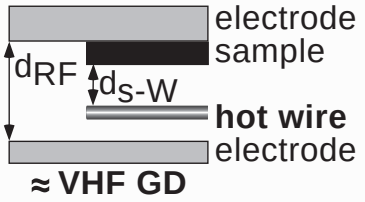

Fig. 2.1: Experimental set-up for the combination of hot-wire *and* plasma technique

SiH_4 flow	3 sccm
H_2 flow	10 sccm
d-sW	15 mm
d-sRF	15 mm
pressure	0.2 mbar
HW power	150 W
$T_{Hot-Wire}$	1850°C
$T_{Substr.}$	250°C
VHF power	10 W
Frequency	70 MHz

Table 2.1: Typical deposition parameters used for the combined deposition process.

2.2 Absorption

At a first stage 'good' intrinsic μc-Si:H films had to be fabricated with the combined Hot-Wire and plasma deposition method. For a more precise definition of 'good' material we took the following two quality criteria:

1. The Photothermal Deflection Spectroscopy (PDS) gives information on the optical absorption on one hand and on material defects on the other

hand. Defects are found in the sub-band absorption at 0.8eV, typically a value $\alpha_{0.8eV} < 10\text{cm}^{-1}$ would be desirable.

2. The dark conductivity σ_{dark} indicates whether the film is intrinsic or extrinsic, here a typical value of $\sigma_{dark} < 10^{-6} S\text{cm}^{-1}$ would be desirable. Experimental analysis show [51] that good thin-film solar cells need an intrinsic absorber layer.

In Fig. 2.2 the optimisation process of the combined deposition method is sketched with respect to the above first criterion of optical absorption: First, absorption around 1.4 eV is improved for the material with the combined HW and plasma method compared to the HW-only material. Second, the silane concentration is varied for the combined deposition process with the result of a better absorption around 1.4 eV for the film at 7% SC on one hand, but the 23% SC film has a lower defect density. Third, the deposition pressure is found to be best (w.r.t. defect absorption) around 0.2 mbar. There is a trade-off w.r.t. absorption in the visible which is higher for the film deposited at p=0.075 mbar.

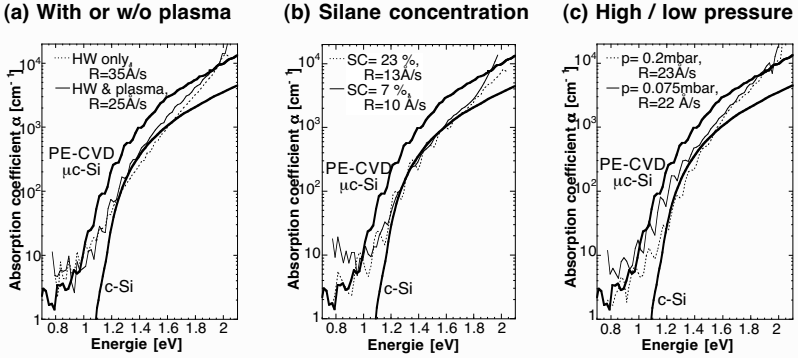

Fig. 2.2: Absorption by PDS measure; as reference with the standard PE-CVD μc-Si:H and c-Si curves: (a) the difference of adding the hot-wire to the PE-CVD process. (b) the influence of the Silane Concentration (SC) on the film quality, and (c) the importance of the deposition pressure.

2.3 Dark conductivity (σ_{dark})

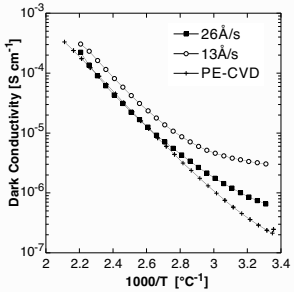

Fig. 2.3: Dark conductivity σ_{dark} measurements of films deposited with the combined process of HW + PE-CVD compared with a high standard μc-Si:H film deposited by PE-CVD.

In Fig. 2.3 the Arrhenius plots of material fabricated by the combined method is compared with a high quality solar grade material by conventional PE-CVD. The film deposited at 13Å/s has a σ_{dark}=3.0·10^{-6}Scm^{-1}, whereas the film deposited at the highest rate (26Å/s) has a lower σ_{dark}=6.5·10^{-7}Scm^{-1}. These two films deposited with the combined method (HW and PE-CVD) almost reach a promisingly low σ_{dark} value of the standard film deposited by the PE-CVD method at a rate of roughly 5Å/s with a σ_{dark}=2.1·10^{-7}Scm^{-1}.

Note the pronounced curvature of the Arrhenius plots of the material fabricated by HW: Up to now, our μc-Si:H material showed only a little bend in the plots of dark conductivity σ_{dark} in function of the inverse temperature but the Arrhenius plots for this new material deviates considerably more from a straight line. Similar behaviour on HW material is also reported by Cifre et al. [13].

2.4 FTIR absorption

The infrared spectra in Fig. 2.4 of the high temperature (400°C) μc-Si:H film fabricated by the hot-wire method shows sharp peaks centered at 900 cm^{-1} and at 2100 cm^{-1}which often is identified as a typical fingerprint of μc-Si:H material [89]. The corresponding peaks of the two other materials fabricated with plasma assistance are broader, and a sign for a lower crystalline volume fraction.

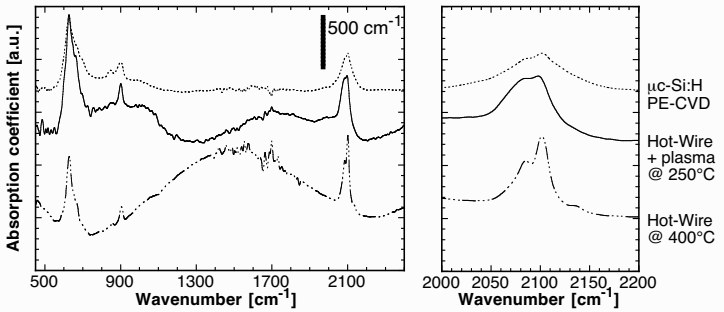

Fig. 2.4: Infrared absorption spectra of μc-Si:H films deposited with three different methods: 1. PE-CVD at 2.5% silane concentration, deposition temperature 250°C; 2. the combined hot-wire and plasma method; 3. by hot-wire alone, deposition temperature 400°C.
The peak at 2100cm^{-1} is separately plotted to highlight the difference in the three microcrystalline materials.

On the other hand, the peak centered at 640cm^{-1} is more pronounced for the material fabricated by Hot-Wire plus PE-CVD, indicating a higher hydrogen content compared to the two other materials. This fact may be beneficial, as we are, thus, obtaining material that is nearer to the microcrystalline/amorphous transition, which is often used so far for best solar cell results (see also part II). The most hydrogen is incorporated in the μc-Si:H film fabricated by PE-CVD, the second largest amount of hydrogen is contained in the film deposited by the combined method HW and PE-CVD and very little hydrogen is contained in the material by the HW method, see Table 2.2.

Table 2.2: Comparison of the hydrogen content C_H of films fabricated by PE-CVD, HW and the combination of HW and PE-CVD.

Deposition method	C_H [at.%]
PE-CVD	4.7
HW & PE-CVD	3.1
HW	0.6

2.5 Optical Emission Spectroscopy

As shown in section 1.7, optical emission spectroscopy is a convenient tool for an in-situ monitoring of plasma processes. The growth conditions of μc-Si:H material fabricated by the combined deposition method (plasma and hot-wire) are analysed in this section. The ratio of the emission line intensities SiH*/H_α gives information on the deposition regime (amorphous or microcrystalline) of the film actually in growth [88, 89].

In Fig. 2.5(a) the optical emission spectrum of the hot-wire process is rather difficult to interpret because of the dominant baseline of light emis-

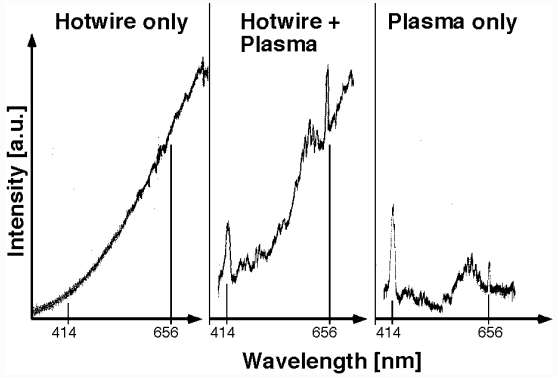

Fig. 2.5: The fingerprints of the three different deposition methods as measured by OES. Note the emission lines of SiH* at 414nm and H_α at 656nm which allow an identification of the growth condition wether μc-Si:H or a-Si:H.

sion. The OES spectrum in Fig. 2.5(b) for the combined process can be better identified with the typical microcrystalline growth condition of a strong peak centered at 414 nm and a low peak at 656 nm wavelength, whereas in Fig. 2.5(c) for PE-CVD standard deposition, the growth conditions appear to be more amorphous as far as OES is concerned. The presence of the hot-wire in the plasma of the deposition chamber does change considerably the OES spectra, thus the combined process is strongly influenced by the hot-wire.

2.6 Solar cells

After an optimisation process of the absorber material towards the desired quality requirements (see section 2.2), a short time of the project was left to pass to the next step of solar cell fabrication. Thanks to the well established knowledge in the IMT thin-film lab on the fabrication of solar cells by PE-CVD, the absorber material could be integrated into a well known and functional p-i-n structure.

Three test devices could be fabricated:

1. Straight forward incorporation of a 3.5μm thick μc-Si:H absorber fabricated by the combined method (at a deposition rate of 25Å/s) with n-type and p-type layers fabricated in another deposition chamber by conventional PE-CVD.
   On this poor quality solar cell, a problem of interdiffusion of the doped p-layer into the intrinsic layer is observed, since the calibrated deposition temperature on the growing layer was measured to reach 380°C. The reason for this excessive temperature is the tungsten wire which is at a temperature around 1800°C and at a distance to the substrate of only 15 mm.

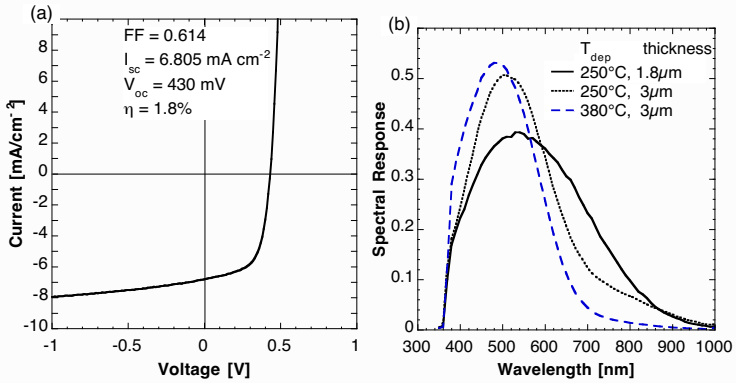

Fig. 2.6: (a) The so far best I-V curve of a 3.5 um thick μc-Si:H solar cell at a deposition rate of 10Å/sec, using a heat-protection, deposited at 250°C substrate temperature (b) The so far best spectral response of a third solar cell compared with the two first ones.

2. The second solar cell was thus fabricated with a heat protection between the cell and the hot-wire. The consequence of the lower substrate temperature of 250°C was a reduced deposition rate of "only" 10Å/s. A promising V_{OC} of 430 mV could be measured (see Fig. 2.6(a)), but the absorber layer was probably too thick (3.5μm).

3. For the third test the absorber layer was thinner, the heat protection was used and a 'soft-start' of the i-layer deposition was applied.
The I-V curve of this last solar cell was not measurable because of too many shunts, but the spectral response (see Fig. 2.6(b)) indicated a better performance in the long-wavelength region.

The rather low performances of these cells (η=1.5%, V_{OC}=484 mV, FF=48%, J_{SC}=6.7 $\frac{mA}{cm^2}$ for the best cell) can be traced mainly to an excessively high deposition temperature during i-layer growth, due to the heating of the surface by the hot filament.

2.7 Conclusions

After a short time on the research project treating the combined deposition method of hot-wire **and** plasma-enhanced chemical vapour deposition (PE-CVD), following conclusions can be drawn:

- Microcrystalline silicon films of a 'device grade' quality could be fabricated by the combined method; these films have comparable properties to the standard μc-Si:H films deposited by PE-CVD as for the optical absorption and the dark conductivity while maintaining a deposition rate of 25Å/s compared to standard material deposited at around 5Å/s by PE-CVD.

- Infrared absorption (by FT-IR) reveal a hydrogen content of 3 at.% compared to 4.7 at.% by the conventional PE-CVD method.

- During layer growth, substrate-temperature control is identified as an important topic for the combined deposition method. In the present study, the following solutions are tested:

    1. If a protection shield between the substrate and the hot-wire is introduced, a reduction of the substrate temperature from 350°C down to 280°C is possible (at a distance substrate-wire of 15 mm) with a drawback of a reduced deposition rate from 25Å/s down to 10Å/s.

    2. The increase of the distance between the substrate and the hot wire reduces considerably the substrate temperature from 350°C at 15 mm down to 200°C at a distance of 35 mm again with the drawback of a reduced deposition rate, this is a well reported effect [8, 81].

    3. The introduction of a powerful cooling system would solve the problem best, since no reduction of deposition rate should then result (as e.g. by the introduction of a shield or by an increase in wire-to-substrate distance). The present study did not allow us any further time to follow up this possibility.

    4. A last possibility would be the optimisation of a 'high-temperature' thin film solar cell which withstands temperatures around 350°C without any interdiffusion. This possibility again is judged to be quite time consuming.

- So far, there seems to be a trade-off between lowering the basically high deposition rates and avoiding the disturbing high substrate temperatures, as seen in the presented study.

- First relatively promising solar cells with a rectifying diode characteristics and a spectral response up into the long-wavelength region of the light spectrum were fabricated. The best device fabricated has a conversion efficiency η=1.8% and with a V_{OC}=430mV, FF=61%, J_{SC}=6.8$\frac{mA}{cm^2}$and is deposited at a rate of 10Å/s, cell thickness 3.5μm.

Chapter 3

Aluminium induced Crystallisation

3.1 Introduction

As the high melting point of silicon (1415°C) is a major obstacle for the direct formation of large-grained poly-Si films on glass substrates, the crystallisation of amorphous silicon deposited on glass substrates is increasingly gaining interest for polycrystalline silicon (poly-Si) devices [98, 76]. Most attention in the field of crystallisation has been paid to solid phase crystallisation (SPC) and laser crystallisation (LC), for a review, see Ref. [6]. In the present study, we investigate the option of aluminium-induced crystallisation (AiC) as another technique that has the following advantages: simple processing (crystallisation temperature below 600°C), standard industrial fabrication methods, and short crystallisation time compared to SPC. It has been demonstrated that the time for the transformation of a 500nm thick a-Si layer into a poly-Si layer by the AiC process can be as short as 30 min at 500°C [57].

Amorphous silicon films crystallise in contact with certain metals at temperatures well below the usual crystallisation temperature[32]. In the case of aluminium (Al), crystallisation temperatures as low as 150°C have been reported[30] which is indeed far below the eutectic temperature (577°C) of the composition silicon-aluminium.

Although up to now a lot of investigations on characterisation and understanding the crystallisation process have been published, to our knowledge no other contribution on functional solar cells incorporating AiC material on glass have been published so far. Several contributions were made on heterojunctions of c-Si wafer and recrystallised material: Tsaur et al. showed that

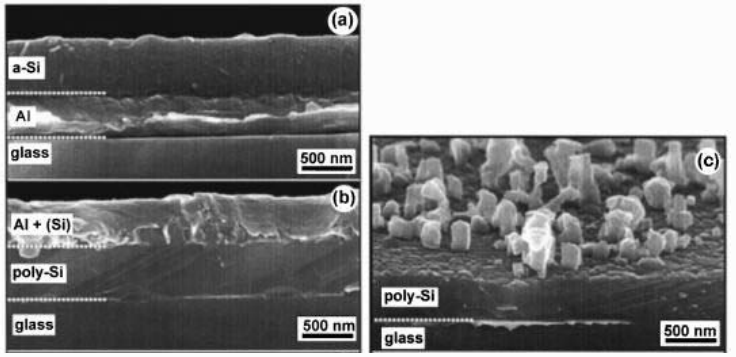

Fig. 3.1: Cross-section FIB micrographs of the glass/Si/Al structure: (a) before annealing; (b) after annealing for 60 min at 500 °C and in (c) after Al etching; the specimen is slightly tilted to depict the Si protrusions on the surface. The short white dotted lines are guides to the eye; source: Nast et al. [57]

a-Si:H deposited on poly-Si wafers can be epitaxially regrown by introducing an Al interface layer to form a p-n junction for solar cells[83]. Although Wallace et al. fabricated heterojunctions with V_{OC}=0.51V, J_{SC}=27$\frac{mA}{cm^2}$ and FF=49% [97], little work has been reported on using AiC to produce poly-Si layers for solar cells on foreign substrates[34].

Up to now, there is no indication of the exact nature of the crystallisation process used by the Australian solar cell manufacturer Pacific Solar, but it could perhaps have some relation with the topic of this chapter. A fact is that at the time of writing, Pacific Solar has achieved 7% conversion efficiency on modules of $0.1m^2$ based on an unpublished crystallisation method of films deposited on glass by PE-CVD[5]. On the other hand the Japanese Kaneka Corp. has presented a conversion efficiency of η=12% for a micromorph[1] ($0.4m^2$ area) module based on PE-CVD fabrication[107].

The work described in this chapter was done by the author during a 6 months working period as visiting research fellow at the Photovoltaic Research Center (PV-RC) of the University of New South Wales, Sydney Australia. It contributes also to the first attempts to fabricate actual working

[1]The IMT researcher's idea to combine the low bandgap μc-Si:H cell with the high bandgap a-Si:H cell, thus, the **micro**-crystalline amo-**morph** tandem cell.

solar cells on glass substrates based on the AiC method. The gathering of c-Si solar cell processing knowledge of the PV-RC on one side, and the experience of thin-film solar cell fabrication of the IMT Neuchâtel group formed an excellent background for this joint project.

3.2 The fabrication process

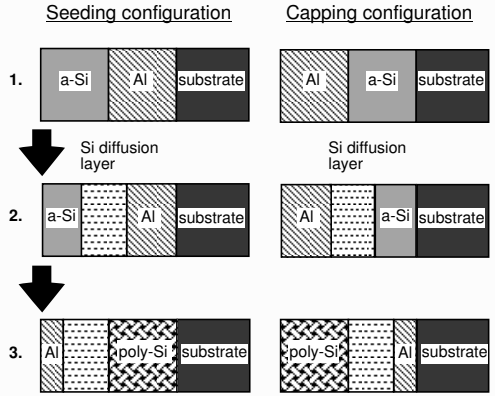

Fig. 3.2: Process steps of the Aluminium induced Crystallisation.

The AiC was performed in this work within a temperature range of 300°C to 500°C for periods ranging from 18 min up to 12 hours in a dry N_2 ambient. Directly after that annealing step the samples were removed from the furnace and cooled to below 100°C in less than 2 minutes in a strong N_2 flow. By doing this, the successive order (glass/Al/a-Si:H) of the deposited layers before the annealing is inverted to glass/poly-Si/aluminium. By a selective Al removal[2] the poly-Si film re-appears and the former separation line Al-Si can be analysed.

The annealed samples were analysed by Raman spectroscopy (Renishaw Ramascope), optical microscope, focused ion beam microscope (FIB) four-point-probe resistivity measurements.

[2]Aluminium removal etch solution: 80 parts phosphoric acid, 5 parts nitric acid, 5 parts acetic acid, and 10 parts deionized water at a temperature of 50 to 55°C

3.2.1 Two fabrication configurations

The AiC process is used to fabricate p-type doped poly-silicon films which then can be further processed for the fabrication of devices. Essentially two different configurations for the film fabrication by AiC have been investigated here. Each of these two ways bring their specific advantages and difficulties with regards to process handling, cost efficiency and device fabrication possibility. Find below the differences for the two fabrication configurations, which are sketched also in Fig. 3.2.

- The so called *seeding* structure based on a deposition order glass/Al/a-Si:H) is transformed into a resulting structure glass/poly-Si/Al. This structure is successfully utilised as a seed layer for an epitaxially thickened silicon film on glass by e.g. Ion Assisted Deposition [37]. This configuration allows for the fabrication of thick (over 5μm) polycrystalline silicon layers on foreign substrates. Possibility to incorporate this AiC film into a p-i-n type solar cell.

- An inverted order of the films (i.e. glass/ a-Si:H/Al) is the basis of the so called *capping* structure. This configuration allows the crystallisation of the whole thickness of the film or even only a fraction of the amorphous film thickness, in such a way as to possibly produce a well-defined and continuous thin AiC-film on top of a thick amorphous film ('thin' meaning up to 20nm and thick around 500nm). This results thus in a structure glass/a-Si:H/AiC. This configuration would then be integrated into an n-i-p type solar cell.

Table 3.1: Two different fabrication sequences used for the Aluminium induced Crystallisation process of silicon; the last column designates the structure of a further utilisation of the AiC material for thin-film solar cells.

configuration	fabrication sequence	Final cell
"seeding"	glass/Al/a-Si anneal	p-i-n structure
"capping"	glass/a-Si/Al anneal	n-i-p structure

The common principle of both configurations is a stack of two films (Al and amorphous silicon) which then is annealed whereby thermally activated silicon diffuses into the aluminium in order to form poly-crystalline silicon. A real inversion of the silicon and the metal layer and a p-type doping of initially undoped silicon occurs. In some cases protrusions impinging the former separation line were observed after the removal of the remaining Al,

see Fig. 3.1(c). These protrusions on the surface have a diameter of several hundred nanometers and turn out to be of silicon; prior to further device processing they are removed or they may complicate the seeding procedure.

Important parameters for the AiC process are the annealing temperature, annealing time, thickness ratio of Al to Si (under-/oversupply of Al) and the presence of a native oxide at the surface.

For the fabrication of devices, it is not fully clear as yet, whether a simple p-n type junction or a p-i-n type junction has to be used. For this discussion, more knowledge on the electronic properties of AiC material is needed, however, these properties like diffusion length etc. are still object of research [62]. Here we have analysed p-i-n and n-i-p type devices where the p-type layer alone was fabricated by AiC and the other layers by PE-CVD. We have not looked at p-n type devices at all.

3.3 Focused Ion Beam imaging

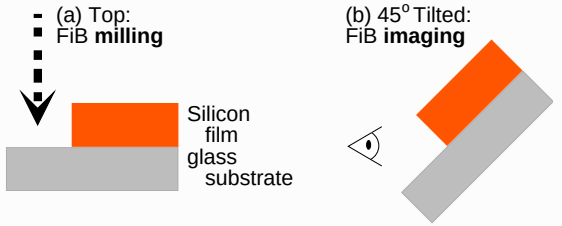

Fig. 3.3: The two steps to FIB imaging: (a) a high energy Ga^+ beam is milling the film; (b) after the sample is tilted, a low energy beam is scanning the probe similar to the procedure in SEM imaging.

The Focused Ion Beam imaging method provides both the opportunity for preparing clean cut cross sections into the silicon film and imaging the sample similar to SEM imaging (for more details on FIB microscopy see e.g. [64, 47]). Advantageous in this case is the fact that the FIB microscopy yields a good contrast between metallic and non-metallic material, in the present case aluminium and silicon, respectively. Thus zones containing metallic residues can well be identified from the surrounding silicon material within the layer. In Fig. 3.3 the procedure of sample preparation (a) and imaging (b) is sketched.

In the first phase of the AiC processing, two main difficulties were identified: first, the crystallised film is not continuous and, second, traces of not fully consumed aluminium within the poly-Si film create a "dirty" absorber, see Fig. 3.4. The protrusions at the former interface Al-Si (see Fig. 3.1(c) are later chemically or physically removed prior to further deposition processing. Surprisingly to some sceptics, a first device made on that raw surface already showed an encouraging result (see section 3.5).

From the point of view of device fabrication, it is desirable to have a homogenous film of polycrystalline silicon. The crystallisation process has to be controlled in such a way that large silicon grains interconnect without any holes on its boundaries. A second requirement is the desired p-type doping of Al. The AiC process has to incorporate Al in the network of Si atoms and not to form a compound Al-Si, see also section 3.6.2.

A better understanding of the AiC process with respect to the previously mentioned obstacles is necessary in order to perform a controlled crystalli-

sation as required for device fabrication. In section 3.6 interpretations and explanations of the AiC process are discussed.

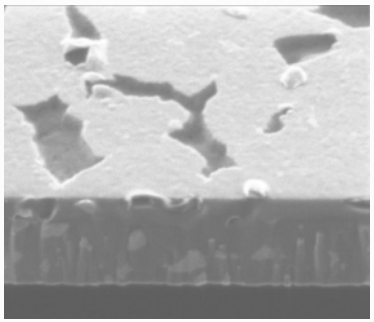

Fig. 3.4: Focused Ion Beam micrographs of a 500nm thin film, tilted by 45°: the holes at the surface indicate a non homogenous formation, white traces in the bulk indicate residual aluminium within the 0.5μm thick film.

3.4 Raman Spectroscopy

Raman spectroscopy was utilised for the detection of the crystallinity of the AiC processed films. As indicated in Fig. 3.5(a) the successful crystallisation can be identified with a transformation of the Raman spectra from a rather smooth bump to a sharp peak centered at 519cm^{-1}.

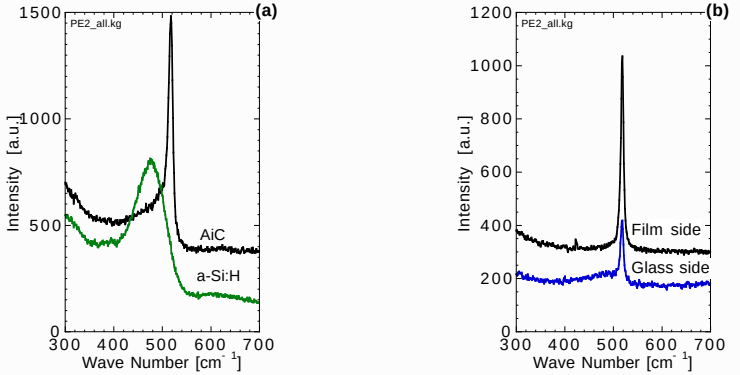

Fig. 3.5: (a) The fingerprints of amorphous and crystalline silicon detected by Raman spectroscopy are used to test whether the material has undergone a crystallisation process. A fully crystallised material is identified in (b) where from the film side as as well as through the glass substrate a strong crystalline peak centered 519cm^{-1} is recorded.

Since the AiC films are fabricated on glass substrates, the probing HeNe laser beam ($\lambda = 632nm$) of the Raman spectroscope can be applied to both sides of a processed film. This method was used in order to test the depth of the crystallisation process: The whole film thickness is fully crystallised, as shown in Fig. 3.5(b) where the Raman spectra from the film side and the glass side are both centered at 519cm^{-1} and no amorphous signal can be detected.

Another question to probe is the origin of the crystalline Raman signal, e.g. the question whether the heat treatment or the presence of the Al actually transforms all the amorphous silicon into crystalline silicon. For this purpose aluminium films of thickness between 6nm and 400nm were evaporated through a mask onto 500nm thick a-Si:H samples of 4x4 cm size. The annealing process transformed only the parts which have been covered with

Al into crystalline silicon, whereas the parts without Al remained amorphous. The crystalline Raman signal originates from the AiC process and not from a SPC process which might have transformed the material, it is thus an interaction of Al-Si in the annealing process.

This is demonstrated with a succession of Raman spectroscopy measurements along a line of several patches of the sample (see Fig. 3.6): the parts with aluminium caps show a significant crystalline peak at 519cm^{-1} and non-metallised parts appear as typical amorphous bumps. With this method, a selective recrystallisation of a 500nm thick amorphous film has been demonstrated. This result encouraged us to look forward to the fabrication of a test junction in the 'capping' configuration.

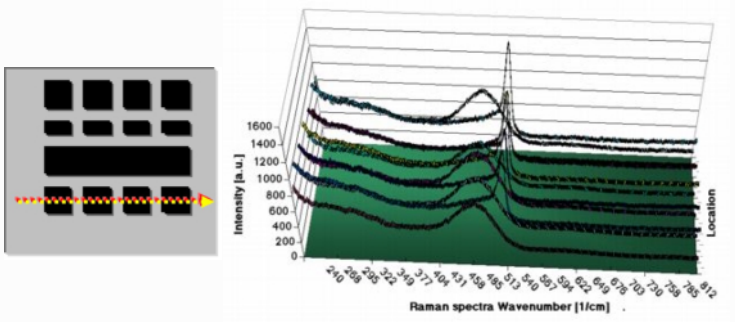

Fig. 3.6: (a) An a-Si:H film sample is locally covered with Al (at the dark patches), but not at the brighter zones where the bare a-Si:H film appears. (b) After a short annealing, a Raman probe scanning consecutive spots over the sample reveals the 'binary' structure of the annealed film: Crystalline peaks and amorphous parts are observed.

3.5 Devices

3.5.1 Seeding structure

After the realisation of fractional crystallisation in the capping structure and fully crystallised films in the seeding structure, a further step towards a solar cell fabrication could be envisaged. The two possibilities of a capping and a seeding structure were implemented for the fabrication of solar cells. The seeding structure was used in a first approach. After the annealing process of the glass/a-Si:H/Al structure, the residual Al was etched off and this non-optimised AiC film was utilised as a p-type layer to form a p-i-n device whereby the remaining $< i >$ and $< n >$ layers were deposited by PE-CVD at IMT Neuchâtel. Even though this raw film has a non-optimised rough surface with protrusions, eventual cracks of adjacent poly-Si grains and a lot of grains emerging from the surface (see Fig. 3.7) it was used for a first cell processing; see the results in Table 3.2

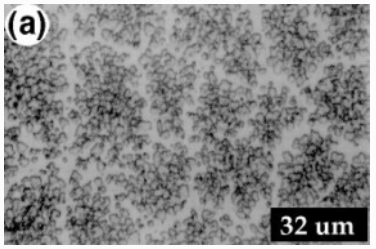

Fig. 3.7: Optical micrograph of the surface of the first raw device.

3.5.2 Capping structure

The first capping structure device was proposed by Sridhar et al. [79]: Molybdenum foil / 50nm of n-type a-Si:H / 7μm of intrinsic a-Si:H by PE-CVD / 100nm of aluminium evaporation is annealed for 2 minutes in the range of 500-725°C. The electrical characterisation was made on films transferred onto a ceramic substrates and photolithographic patterning from the Mo-side. Best results are reported for a film annealed at 500°C with a photoconductivity of $1.8{\cdot}10^{-4}\Omega\text{cm}^{-1}$ and a carrier diffusion length (deduced from photoconductivity) of 5.3μm; XRD revealed a preferential crystalline orien-

tation along the < 111 > direction. How come the authors did not report any solar cell measurements such as I-V or quantum efficiency?

Anyhow, this paper encouraged us to fabricate a further device, based on the following capping structure: TCO/n-type μc-Si:H (20nm)/intrinsic a-Si:H (500nm) /Al (9.4nm). A commercially available Asahi U type Transparent Conductive Oxide (TCO) coated glass substrate was covered with a microcrystalline n-type and the intrinsic amorphous silicon film by VHF-GD and then 22nm aluminium was evaporated on top of this structure. Between the silicon deposition and the aluminium deposition there was a vacuum break. The final structure is then annealed. No holes in the surface film could be observed in the microscope images and no aluminium inclusions appeared in the trench-cut. This was the first working device in the capping AiC configuration which permitted measurements of external quantum efficiency (see Fig. 3.8(b)), current-voltage (I-V), and reflectance & transmittance (T&R).

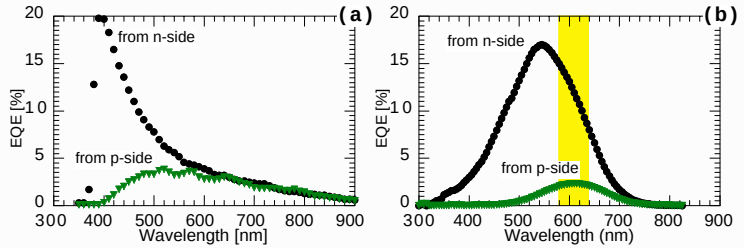

Fig. 3.8: External Quantum Efficiency (EQE) measurements: (a) of the first raw AiC sample PE14a11 used as solar cell in the seeding configuration; (b) of a solar cell based on the capping configuration AiC-sample LN3c5.

In both configurations, a higher quantum efficiency is recorded for n-side illumination of the device compared to the p-side illumination. This may be an indication of a poor bulk absorption, of poor interfaces or it could be possible that only the n-type μc-Si:H film generates the photocarriers that are seen in the quantum efficiency data. These hypothesis have to be investigated further, in future work.

Table 3.2: Values extracted from 1 sun I-V measurements on both, seeding and capping configurations of AiC junctions.

	Seeding structure		**Capping structure**	
	Illuminated from:			
	p-Side	n-side	p-side	n-side
V_{OC}	0.12V	0.15V	0.381V	0.152V
J_{SC}	$0.73\frac{mA}{cm^2}$	$1.5\frac{mA}{cm^2}$	$0.39\frac{mA}{cm^2}$	$1.6\frac{mA}{cm^2}$
FF	44%	38%	28%	25%
Area	$0.01cm^2$		$0.4cm^2$	

3.6 Discussion

3.6.1 Crystallisation process

It is already known[60] that for the AiC process at 475°C the interdiffusion of Si and Al atoms leads to the formation of crystalline silicon nuclei within the Al layer. These nuclei grow initially up to the thickness of the metal layer and then continue to grow laterally, sandwiched between the substrate and the Al/a-Si interface. The Si grains, which have grown within the former Al film, can achieve a size of 10μm and more until adjacent grains meet to form a continuous Si layer[58]. The overall process therefore consists of the exchange of the layer positions, whilst a poly-Si film is formed on the glass substrate. It seems that the formation of a well-defined continuous poly-Si film is only possible for similar thicknesses of both Al and a-Si films (a ratio of layer thickness Al/a-Si of about 1:1)[60], thus neither an undersupply nor a oversupply of Al is recommendable. Furthermore, both the grain size of the poly-Si film and the speed of the crystallisation process depend on the annealing temperature. In general, the lower the temperature during AiC, the larger the Si grains will be.[59]

The general driving force in metal-induced crystallisation of a-Si:H is the difference in the free energy between the amorphous and the crystalline phase[35]. In the case of the AiC process there is apparently a delicate equilibrium of thermally activated diffusion and nucleation. The outcome of the crystallisation process eminently depends, thus, on factors like annealing temperature and film thickness ratio on one hand and on the state of surface oxidation of the a-Si film on the other hand.

All the previously mentioned investigations by O. Nast et al. were carried out on sputtered amorphous silicon (a-Si) which is known to be rich in electronic defects, since here the dangling bonds are not passivated by hy-

drogen. Our investigations were made on hydrogenated amorphous silicon (a-Si:H) deposited by the PE-CVD method where the defects are passivated by hydrogen. They furthermore showed that here (at least for the capping structure) a removal of the native oxide prior to Al evaporation is essential for a well controlled AiC process. The phase transformation from hydrogenated amorphous silicon to crystalline silicon may occur already around 200°C and a selective crystallisation of thin layers is discovered to be possible.

3.6.2 Doping by Aluminium

The Aluminium induced crystallised silicon layers always have p-type doping characteristics. In order to use these doped layers within junctions, it is required to have a p-type doping where the Al is incorporated in the network of Si atoms and not a formation of a compound Al-Si, as mentioned previously in section 3.3.

Nast et al. [59] report on SIMS measurements indicating an Al concentration of $3{\cdot}10^{19}\text{cm}^{-3}$ (equivalent to 0.06 at.%) within poly-Si films annealed at 500°C. However, not all of the incorporated Al is electrically active since Hall-effect measurements revealed a p-type doping concentration of $2.6{\cdot}10^{18}\text{cm}^{-3}$. It is suggested that the Al is incorporated on interstitial and substitutional sites in the Si lattice. In fact, Tsaur et al. [83] have shown that the incorporated Al can be thermally activated during heat treatments at 900°C so that it ends up on substitutional sites leading to a doping concentration of $2{\cdot}10^{19}\text{cm}^{-3}$, which agrees with the values of the solid solubility of Al in Si reported in the literature [84].

3.7 Conclusions

In conclusion of the 6 months research project at the Photovoltaic Research Center of the UNSW Sydney, there is still some work to be done in order to transform amorphous silicon by AiC into a poly-Si material which then can be used in thin-film devices such as solar cells and TFTs. In literature, many contributions on metal-induced crystallisation have been made since the 1960s, but up to now no solar cells incorporating AiC on foreign substrates are reported. The research activity in the last years concentrated more on material science than on the fabrication of devices. In this work, an attempt was made to finally fabricate a working solar cell. In the capping configuration, the problems of a separation of a wholly amorphous layer into a crystallised top and amorphous bulk are presented: The recrystallised film had holes in the surface (no continuos film). Further analyse by focused

ion beam microscope (where a view onto a trench-cut of the film is possible) indicated aluminium inclusions in the bulk of the film. After a careful optimisation, the process allowed a selective growth of a p-type film. This AiC-film was formed on an amorphous silicon absorber and a junction-like behaviour is observed: V_{OC}=0.381V, J_{SC}=0.39$\frac{mA}{cm^2}$.

In the seeding configuration the AiC layer on glass is coated with a μc-Si:H n-type film. At the end of that project, the seeding device structure was still under investigation[62]. Further research is necessary for a better understanding of the material of aluminium induced silicon thin-films and the fabrication of reasonably working devices.

Chapter 4

Conclusions of Part I

In the first part of this work three fabrication methods for thin microcrystalline silicon films are presented: first the widely and successfully used PE-CVD method, second the novel method of combined HW and PE-CVD deposition and third the AiC method were investigated. The first method has already reached a mature stage of industrial application of large-scale solar module fabrication since about ten years. The two other methods are still in an early phase of development. This makes the younger methods attractive, since there are new elements to be found and old knowledge from plasma technology can be re-applied.

In the center of our description of the PE-CVD deposition method, there is the dilution series which allowed for a large number of investigations. Since there are both films on glass and functional cells within a silane concentration around the phase transition between microcrystalline and amorphous material, this series is of a large interest and will appear in chapter 9 again. Raman spectroscopy of films reveals two clear information: first the Raman peak documents a phase-transition from amorphous to crystalline silicon for films deposited on glass if analysed from the film-side. Second, the absence of any crystalline Raman peak for the same films analysed trough the glass substrate, thus a prove of an amorphous incubation layer for films deposited on glass (see Fig. 1.8). A lot more is known now on the crystalline microstructure of μc-Si:H films thanks to TEM, AFM and XRD characterisation techniques: films deposited on glass substrates may start in a mixed-phase (or even a pronounced amorphous incubation layer can be observed) and then turn fully microcrystalline only towards the final hundreds of nanometers of the film thickness. These findings are double-checked by Raman and TEM investigations. Important to note is thus this **substrate-dependent growth** of thin silicon films, i.e. that a film may grow 'fully' microcrystalline on an adequate seeding layer (such as a ZnO film) but it may have a thick incubation layer if deposited on a glass substrate. The thin-film solar cell is thus not a simple gathering of individually optimised single films but a more complex device.

The novel configuration of the closed chamber plasma is introduced and characterised by OES. The plasma conditions of the CC-VHF-GD can be identified with typical μc-Si:H growth conditions of the conventional PE-CVD method. Solar grade material could be fabricated and integrated in functional solar cells. Because silane consumption is halved, the CC-VHF-GD is found to be an economical method to fabricate μc-Si:H thin films even though the first solar cells need further optimisations.

The combined method of hot-wire and PE-CVD is actually a straight forward approach to increase considerably the deposition rate for μc-Si:H films up to 25 Å/s. The results showed soon the difficulty of overheating the substrate by the hot wire. Films could be optimised towards solar grade material (w.r.t. optical absorption and dark conductivity). A compromise between high deposition rates and low substrate temperatures had to be found. Nevertheless, implementation of such material into a functional solar cell was possible and gave a promising conversion efficiency η=1.8%, V_{OC}=430mV, J_{SC}=6.3$\frac{mA}{cm^2}$, FF=61%, deposition rate 10Å/sec. Unfortunately, further optimisations were too time demanding for the given project time scale.

The fabrication of polycrystalline silicon thin films based on the crystallisation of amorphous films is a long lasting wish of the "bulk-silicon community", which (among other problems) will soon be in short of solar grade silicon wafer supply. The AiC method allows for a cheap (compared to laser crystallisation) and quick (compared to solid phase crystallisation) fabrication of p-type silicon films by Al doping. The process is reproducible but the achieved material still leaves some difficulties to overcome, i.e. residual metallic Al within the film and protrusions on top of the film. Nevertheless, first humble solar cells could be fabricated with diode characteristics. Focused Ion Beam milling was found to be a useful tool for microscopic studies of the fabricated films.

After this first part on three methods of fabricating silicon films, the PE-CVD method is chosen in the next part of the thesis for further optimisation on functional n-i-p solar cell devices.

Part II

Microcrystalline silicon n-i-p solar cells

Introduction

The main aim of solar cell research is an increase of the conversion efficiency η and a cut-down of fabrication cost. In this chapter, we look at thin-film microcrystalline silicon (μc-Si:H) solar cells; we present here possibilities of enhanced optical absorption due to better light coupling into the cell as well as development of back-reflector design. A definite, but small increase in short-circuit current is observed, if the microcrystalline silicon solar cells are fabricated onto a stainless steel substrate instead of being deposited on a transparent glass substrate. A much more substantial increase of efficiency is documented for cells deposited on light scattering back-reflectors of the structure substrate/silver/ZnO. The interface of the Zinc Oxide (ZnO) to the n-type silicon film has to be optimised carefully with respect to optical, electrical, and crystalline growth aspects. Correlations of the surface roughness of this back-contact ZnO and the generated short-circuit current is shown, together with a study of four different substrate types (glass/ZnO, glass/silver/ZnO, stainless steel, copper).

A series of similar cells have been studied where only the morphology of the intrinsic absorber layer was varied by a change in hydrogen feedstock gas dilution in such a way that a phase change from microcrystalline to amorphous silicon is obtained. Approaching the amorphous phase, a clear increase of V_{OC} with a decrease of fill-factor and a more or less stable J_{SC} can be observed for this series of microcrystalline solar cells; this series finally leads to only a slight increase in conversion efficiency, but it does indicate where future fine-tuning has to be done.

The quantum efficiency (QE) of solar cells illuminated from the p-side is compared with the QE of solar cells illuminated from the n-side (through the substrate) this comparison gives insight into the quality of the interface substrate-silicon. A poor signal for the n-side illuminated cells reveals nucleation problems and a non optimum n-i junction.

At last, investigations made on lock-in thermography showed the presence of shunts not only on the borders of patterned cells but also inside the cell surface.

In this second part of the thesis, three approaches to improve the solar cell's conversion efficiency are given: starting with observations on the optical behaviour of the thin-film device, then going over to the problem of interfaces of successive silicon layers (which make up the solar cell) and ending with results regarding the variation of the crystalline phase of the absorber layer.

Chapter 5

Fabrication of n-i-p solar cells

Important steps for n-i-p solar cell manufacturing are: a successive deposition of a first thin film of n-type doped μc-Si:H onto a electrically conductive back-contact, then the deposition of the intrinsic μc-Si:H absorber layer (also referred to i-layer), then the deposition of the p-type μc-Si:H film and a final top-contact. Three possible deposition methods for depositing μc-Si:H layers are given in the first part of this thesis, whereas throughout this second part, we concentrate on solar cells fabricated by the PE-CVD method. Fig. 5.1 shows the different layers involved in the entire n-i-p solar cell and Table 5.1 gives typical dimensions of these layers as used in this work.

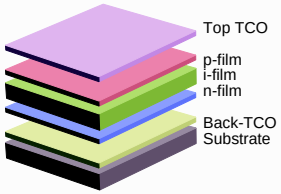

Fig. 5.1: Thin film silicon solar cell: a multi-film device.

film-type	thickness [μm]
top-TCO	0.07 - 2.5
$< p >$	0.02
$< i >$	2.2
$< n >$	0.025
back-TCO	0 - 0.5

Table 5.1: Typical n-i-p cell parameters

Essential aspects in the fabrication of a silicon n-i-p solar cell are:

1. The choice of a substrate involves aspects like: material cost, compatibility to vacuum low temperature processes (with temperatures below 300°C), optical (e.g. back-reflecting) and electrical (preferably: insulating[1]) properties.

[1]A series connection of cell segments is much simpler if the substrate is non-conducting.

2. The back-TCO material (commonly used in this work were SnO_2 or ZnO) has to be optically transparent and electrically conductive (as we will see later).

3. Solar cell deposition parameters depend on deposition temperature, feedstock gas dilutions, deposition pressure, plasma power, plasma frequency, RF-electrode design, outgassing rate of the vacuum chamber and many other factors.

4. The top-contacts have to be made of transparent conductive oxides (TCO) in order to connect electrically the device without a significant illumination loss (commonly used in this work were ITO or ZnO).

5. The so fabricated cell needs to be patterned and wired for measurements and applications.

6. Finally characterisation of the solar cell is done both under a solar simulator and in a quantum efficiency set-up.

5.1 Coupling light into silicon

The principal task of a solar cell is to convert light into electricity, and, thus, to absorb a maximum amount of light in a cheap and efficient way. Reasons enough to consider first some optical aspects of the device.

5.1.1 Optical loss

After the deposition process of a solar cell on a commercially available TCO coated glass from ASAHI Corp. the following structure is measured optically with a spectrometer (probing beam onto the cell): glass/n-i-p cell of 2.2μm. The total reflectance on the solar cell in Fig. 5.2(a) is on an average of 30% whereas the total transmittance is 19% in average over the whole spectrum. Thus, 49% of the light falling onto the solar cell is lost due to high reflection and incomplete absorption.

5.1.2 Anti reflection Coatings

The high index of refraction of silicon (n=4.5 @ λ=350nm) is the main reason for the high reflection losses at the silicon-air interface, as indicated in Fig. 5.2(a). Cell absorption can considerably be improved and optical losses reduced by the introduction of an anti-reflecting coating (ARC), which in

the present case of n-i-p solar cells serves as well as front contact[2]. The two types of ARC used in the presented work are shown in Fig. 5.2(b): A 70nm thin film of ZnO or ITO gives a typical blue color to the solar cell and results in a minimum reflectance below 2% at a wavelength around 530nm. However the average reflectance of this ARC is in the present case over the whole spectral range from 320nm to 1200nm as high as 36%. A much better wide-range ARC is made of a thick (up to 2μm) surface-textured ZnO film, where an average reflectance of 17% is commonly measured over the full spectral range. The device structure used here for measuring both ARC types is glass/silver/ZnO/n-i-p/ARC-ZnO.

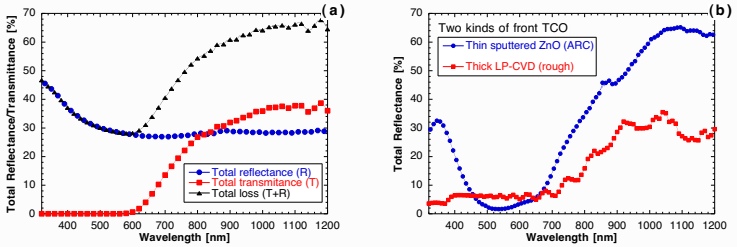

Fig. 5.2: (a) Optical loss on a solar cell on glass substrate without any front contact; reflectance (dots), transmittance (squares) and the sum of both (triangles).(b) The reduced optical loss due to an anti-reflection coating on the silicon solar cell.

[2]The present study of n-i-p cells "generously" ignores the need for encapsulation of solar cells. This important fabrication step for commercially available solar cells can change the optical behaviour of an ARC.

Chapter 6

Matching reflectors to the solar spectrum and absorber material

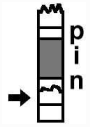

A reasonably working thin-film silicon solar cell absorbs a limited amount of light at the first passing through the absorber. If a reflecting substrate is used instead of a transparent substrate, light is reflected back into the cell. This section gives the calculated requirements for the design of back-reflectors (B-R) or the answer to the question "what would be the optical characteristics of a perfectly designed B-R for a thin-film solar cell?"

6.1 Definitions

In this work, the term *substrate* is used in the most common way of any possible material onto which a cell can be deposited, regardless of the presence of anything between the substrate and the cell such as a back-reflector. The term *back-reflector* designates the optically reflecting part of a substrate onto which the cell is deposited, but *back-reflector* is also used as a more general term in the sense of a 'substrate containing an optical back-reflector'. The B-R in this work have to scatter the light back into the absorber layer for a better light-trapping of the solar cell - such an angularly diffuse reflectance is in contrast to the *mirror* which reflects light only specularly without any diffuse scattering.

6.2 Solar spectrum and silicon absorption

The following calculations are based on the idea of shaping an ideal B-R which reflects light back into the solar cell at precisely computed angles with a nearly 100% reflectance. This is the typical behaviour of an optical diffraction grid. There is just one drawback: The diffraction orders (and thus, also the angular distribution) of the reflected light depend directly on the wavelength of the incoming light. A spectrally wide-range diffraction grid is hardly achievable. But never the less, for interest and in view of future projects, here are basic requirements for the design of such reflectors.

Given is the normalised energy irradiation of the sun on earth[1] AM1.5 and the band-gap of the μc-Si:H absorber material E_g=1.12eV. All light of an energy higher than the gap ($320nm < \lambda < 1109nm$) can be absorbed within a sufficiently thick absorber layer.

The reduction of the cell thickness while maintaining good cell absorption properties is the challenge of this work; it is motivated by a certain economic interest, for thanks to light trapping schemes such thin film cells become economically feasible.

The optimisations start with the two available quantities 1^{st} the standard AM1.5 solar radiation on earth and 2^{nd} the optical absorption of a standard[2] μc-Si:H film deposited on glass, see Fig. 6.1. Then with the help of equation 6.1 for absorption [80] the light reaching the rear end of the cell can be calculated.

$$\Phi(x) = \Phi_0 e^{-\alpha x} \tag{6.1}$$

The part of the AM1.5 sun spectrum which is left behind a 2μm thick microcrystalline film is plotted in Fig. 6.2 and reveals the amount of not absorbed light (this quantity will be reduced by the introduction of an appropriate light-trapping scheme, but could also be absorbed with a thicker absorber layer).

Now, the following procedure is chosen to determine the wavelength λ_0 at which the B-R is supposed to work best: The surface under the curve of microcrystalline absorption (see Fig. 6.1) is integrated, the whole integrated surface is divided by two, the wavelength λ_0 can be read out at the place where this integral reaches half the surface.

[1] AM1.5 actually corresponds to the normalised irradiance at a latitude of 48° on earth, with $AMx = 1/cos(\alpha)$ where α is the latitude on the globe. See ref.[1] for the spectrum data.

[2] There is actually no such thing as *the* standard microcrystalline film, but as an in-house reference we use the optical data from a typical PDS measurement from a preceding thesis [28].

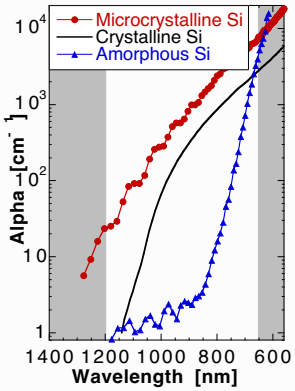

Fig. 6.1: Absorption curves of silicon in crystalline, microcrystalline[2] and amorphous phases. Markers indicate the interval of interest of $650nm < \lambda < 1200nm$.

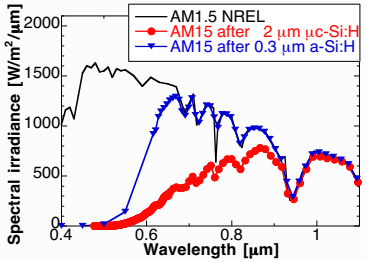

Fig. 6.2: What light of the solar spectrum AM1.5 arrives at the back-reflector? In this figure the spectrum is 'filtered' by a 2μm thick microcrystalline silicon (dots) film on one hand or by a 0.3μm thin amorphous silicon layer (triangles), on the other hand

The numerical integration interval running from 450nm up to 1100nm yield a half surface at the wavelength $\lambda_0 = 866nm$. In other words, the amount of not absorbed sun light below the band-gap of E_g=1.12eV is divided into two equal parts and the wavelength at which a B-R for μc-Si:H thin film solar cells should work best is found in this manner.

We find the ideal reflector grating for μc-Si:H cells could be optimised to work best at a wavelength of $\lambda_0 = 866nm$. Recently Eisele et al. [18] presented submicron gratings with grating periods from 390nm up to 980nm. Amorphous p-i-n type solar cells were fabricated onto these optical diffraction grids. In this paper, only a reduction in overall reflectance below 10% within the wavelength interval from 400-800nm is reported but no J_{SC}-improvement so far – this experience is most suitably performed with a low band-gap solar cell absorber material such as μc-Si:H.

The fabrication of such sub-micron gratings and the implementation in n-i-p thin-film solar cell devices is a technological challenge and is at the time of writing still under investigation.

Chapter 7

Back-reflectors

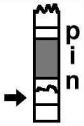

Microcrystalline silicon solar cells have been successfully deposited on back-reflecting substrates with a naturally grown surface texture. The main benefit of such substrates is a better *diffuse* reflectance (which increases the optical path and thus the absorption probability in the cell absorber), and a simple manufacturing process. These type of back-reflectors (B-R) do not scatter the light completely randomly, but rather in a more or less well preferred direction, which is typical for the nature of growth.

7.1 Comparison of three kinds of back-reflectors

This section comments on the observations of the optimisation process of back-reflectors (B-R), even though the most of time was invested in the fabrication process of solar cells. Unfortunately during this thesis, hardly any resources were available to investigate in the fabrication process of B-R at IMT.

Fig. 7.1 gives an overview of reflectance data of the best samples of each B-R category i.e.

- Glass/silver/ZnO = "Jülich type"
- Copper/ZnO, developed at IMT
- Steel/hot silver/ZnO, developed at IMT

Many of these B-R were measured before cell deposition in order to obtain a background information on the optical quality of the utilised substrate. These reflectors were supplied from project partners[1] and are compared with

[1]Early B-R were developed during an European joint project 'NEST' and 'JOULE' at the Photovoltaik Institut Jülich, Germany.

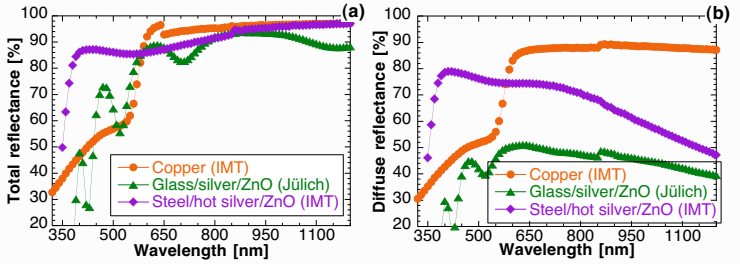

Fig. 7.1: (a) Total reflectance and (b) Diffuse reflectance of three typical B-R.

results of IMT in-house B-R development.

The spectral range of interest for B-R design of μc-Si:H solar cells lies within $650nm < \lambda < 1100nm$ because the short-wavelength part of the solar spectrum is already absorbed. For a better understanding of the recorded reflectance data (especially if interference fringes appear) it makes sense to extend to both sides of the interval these limits to an interval included within $320nm < \lambda < 1200nm$.

7.1.1 Method of comparing back-reflectors

For a careful comparison of different B-R, a discussion on the requirements is necessary and the question on back-reflecting "quality" arises, i.e. one must answer the question 'what is a good back-reflector?' Basically, one needs:

- A maximum overall reflectance (approaching R=100%).
- A maximum diffuse reflectance (reaching the total reflectance).
- A maximum near-infrared reflectance (where low solar cell absorption should be increased).

As a preliminary conclusion, one can say that the haze factor alone is a very poor characteristic for a B-R since it bears not much information on the value of absolute reflectance. It is best to present both, diffuse and total reflectance together. Furthermore, a specific disadvantage of the diffuse reflectance curve is the lack of any information on the the angular distribution of that amount of scattered light. So angular resolved reflectance measurements are necessary here. The choice of the absorber material (whether

amorphous or microcrystalline silicon) determines as well the choice of the spectral interval to be considered in reflectance measurements.

We prefer here to reduce the reflectance data to the average values over a certain spectral range of total and diffuse reflectance, and where necessary we present the full spectral reflectance measurement and thus use less the haze curve.

7.2 Solar cells on silver/ZnO back-reflectors

The B-R structure with a silver film as reflecting material and a ZnO film as a diffusion barrier (to prevent a silver contamination into the silicon i-layer) became soon a popular B-R candidate. Mainly two reasons support this choice: 1st because of a relatively simple fabrication process and 2nd because of a wide process window for variations of the material properties, e.g. silver is just sputtered, ZnO can be sputtered or fabricated by CVD and parameters like substrate temperature, process pressure and thickness influence important B-R characteristics such as surface roughness, optical transparency and electric conductivity [75]. In addition to these reasons, the choice of substrate could be extended from glass substrates to stainless steel substrates.

Measurements on the average reflectance of the B-R within the long wavelength region of the spectrum have been carried out in order to classify the quality of every B-R. However, no systematic correlation between the substrate quality and the short-circuit current J_{SC} could be noted, because the optimisation of two parameters at the same time (substrates and solar cell) of such a complex process like solar cell manufacturing generates a too large scattering of the data. Generally speaking, a causal relation between one factor (the reflectance of the substrate) and the other factor (the J_{SC}) exists indeed. But in the list of hundred entries of short circuit currents, eight out of top ten currents are generated on the silver-ZnO type of B-R, thus proving the early (1998) quality of that B-R structure over the other substrates available at that time. In this comparison the cells on the recently (2001) introduced IMT-type substrate based on natural growth-textured silver, which give even higher J_{SC}-values, were not included.

7.2.1 Wet-etched ZnO substrates

The back-reflectors here presented have a structure glass/chrome/silver/ZnO and are then chemically etched (with 0.5% HCl aqueous dilution) for a time varying from 4, 7, 15 or 30 seconds (for more on this method see the publi-

cations by A. Selvan [72, 73, 74, 75]). A simplifying observation states 'the longer the etch time, the rougher the surface texture'.

The total reflectance in Fig. 7.2(a) remains approximately constant whereas the haze factor (and thus the diffuse reflectance) increase steadily with an increase of the etch time. Whereas the average within the spectral range from 650 to 1200nm was computed for the haze factor. The absorption loss (A_{loss}) in Fig. 7.2(b) is based on the subtraction of 7.1 where the quantum efficiency (QE) data and the total reflectance (RT) is computed and averaged within the spectral range from 650 to 1000nm.

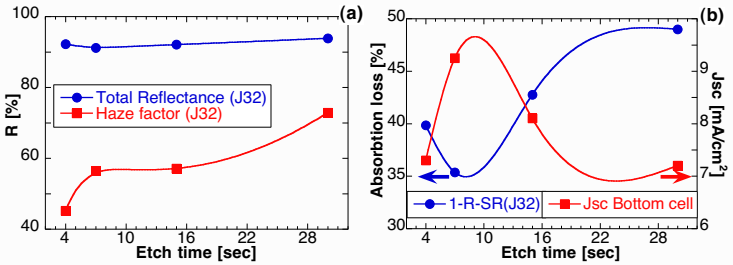

Fig. 7.2: Etch time dependence of optical parameters of wet-etched ZnO back-reflectors: (a) Total reflectance (dots) is nearly unchanged, whereas the haze factor (squares) increases with increasing etch time; (b) the J_{SC} has a clear maximum at the place (7sec etch) where the absorption loss curve has a pronounced minimum.

This is exactly what back-reflector design should be all about: with one fabrication parameter, the optical property can be tuned to the best working point for a given device structure.

$$A_{loss} = 1 - RT - QE \tag{7.1}$$

The optical fine tuning in Fig. 7.2(b) yields that the minimal optical loss and the maximal short-circuit current (J_{SC}) match at 7sec etch time. Thus the simplification mentioned above can not be continued; it would be wrong to state 'the rougher the surface texture, the better the cell performance'. The observation on the increased surface texture with increasing etch time will be discussed later on in the section on AFM / SEM.

The surface roughness root mean square value (see definition on page 132 as plotted in Fig. 7.3 gives information on vertical features of the topography

of the surface. Note that other features of the B-R surface such as horizontal dimensions of the texture are not considered in the RMS value but need further analysis of the data, e.g. autocorrelation, fourier transformations, and other statistical analysis tools.

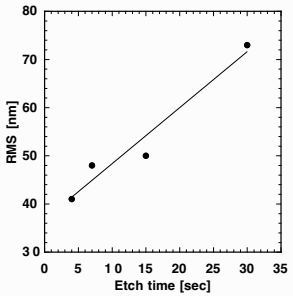

Fig. 7.3: The Root Mean Square roughness vs. the ZnO etch time.

7.2.2 Solar cells on rough silver back-reflectors

Substrates based on surface-textured silver (by hot silver deposition) had indicated most promising results as early as May 1999 on an experimentally developed silver/wet-etched ZnO substrate from Jülich (see the cell's characteristics in Fig. 8.6). The structure consisted of a stainless steel/hot silver/ZnO.

At IMT substrates having the same structure were fabricated at a later date within a diploma thesis in 2001.[99] They consisted of the naturally-grown rough surface of silver films deposited at temperatures above room temperature (up to 400°C). This rough silver surface improves the amount of diffusely reflected light over the specularly reflected light. The back scattering ability of the rough B-R enhances the absorption probability of light within the solar cell. Both the excellent optical properties of this type of B-R and the ideal interface to the microcrystalline silicon solar cell could be combined optimally. In Fig. 7.4(b) the increase in short-circuit current on a rough silver compared to a flat silver B-R is shown: The J_{SC} could be increased from 18.6 to 21.6$\frac{mA}{cm^2}$ over the whole spectral range, or from 7.1 to 9.4$\frac{mA}{cm^2}$ considering only the long-wavelength region between 650nm and 1200nm. This is an 16% increase for the overall spectrum or even a 33% increase for the long-

wavelength region. After further optimisations the so far best J_{SC} exceeding 24$\frac{mA}{cm^2}$ could be measured on these type of back-reflectors, see section 8.3.

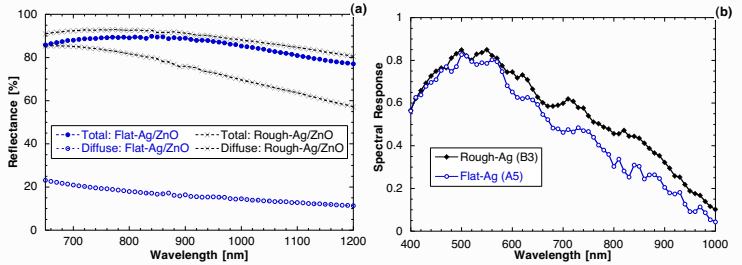

Fig. 7.4: (a) Total and diffuse reflectance of a flat and a rough B-R and (b) the gain in quantum efficiency of a microcrystalline deposited onto such substrates.

7.3 Solar cells on copper back-reflectors

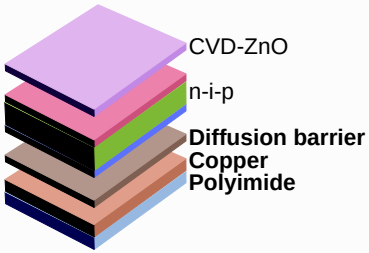

Fig. 7.5: The structure of the μc-Si:H n-i-p solar cells on copper B-R.

Several substrates with copper as reflecting material at the place of silver were tested in search of a cheap and efficient back-reflector for microcrystalline n-i-p solar cells. Reasons for the copper series are the excellent reflecting properties of copper and lower material cost of industrially available copper coated polyimides compared to the silver coating of stainless steel substrate. The investigations concentrated on the feasibility and a compatibility check of the thin-film solar cell fabrication process with the newly introduced copper substrate.

The technological main concern was to prevent chemically interdiffusion of copper to the silicon absorber, since copper contaminations within the intrinsic layer create 'bad' mid-gap defects. Most effort concentrated on the minimum necessary thickness of the diffusion barrier (our choice here: sputtered ZnO, CVD ZnO or silver) to have a maximum optical benefit. No tests on surface texturing of the back reflector material nor a surface texture of ZnO for better light scattering were carried out.

Solar cells are fabricated of the structure depicted in Fig. 7.5 and an overview of the cells with best V_{OC} or best J_{SC} out of this series is presented in Table 7.1. For some cells, a diffusion barrier in form of a thin Ag layer was introduced. This interface Ag-ZnO is known to function in cells on glass and stainless steel, but is not an optimal option for the copper B-R. Surprisingly, CVD-ZnO is used as back-TCO for all cells in Table 7.1 which is in contrast to other observations, where the interface TCO-cell seems to work better for sputtered ZnO, see section 8.1.

In conclusion, out of the eight microcrystalline deposition runs of μc-Si:H solar cells on copper substrates the best cell had a conversion efficiency

Table 7.1: Summary: solar cells on copper back-reflectors.

Structure Thickness[nm]	V_{OC} [mV]	FF [%]	J_{SC} [$\frac{mA}{cm^2}$]	η [%]
Cr/Cu/CVD-ZnO [5/100/2000]	**509**	52	14	3.7
Cr/Cu/Ag/CVD-ZnO [5/100/5/1000]	**472**	64	16.6	5.0
Cr/Cu/CVD-ZnO [5/100/2000]	440	64	19.1	**5.4**
Cr/Ag/CVD-ZnO [5/100/2000]	440	55	20.4	**5.0**

of η=5.4% (with V_{OC}=440 mV, FF=63%, J_{SC}=19.1$\frac{mA}{cm^2}$). The main benefit of the series of copper/polyimide based substrates (low cost of a flexible back-reflector material) is opposed to the technological problems encountered in the fabrication of solar cells so far. These substrates systematically destroyed the junction of the solar cell, probably due to a diffusion problem. With the introduction of diffusion barriers (silver, sputtered ZnO and CVD ZnO) the cells operated normally, but the optical benefit of the copper was lost again.

Chapter 8

Interfaces make up the whole cell

In chapter 7 the possibility of adjusting optical properties of back-reflectors (B-R) is shown. In this chapter, the need for adjusting cell deposition parameters for every newly developed back-reflecting substrate is explained. The interface of the substrate and the cell, where the nucleation of the first silicon film starts is a technologically crucial part in cell manufacturing, see also section 9.1.1 for the interfaces observed from both n- and p-side by quantum efficiency.

8.1 The back-TCO/cell interface

The interface back-TCO/n-type film (we call it here 'back-interface') takes on a very important role for the cell deposition and has an influence on the structure of the whole cell and its performance: Indeed, nucleation of silicon grains, electronic and optical properties are key issues which depend on the

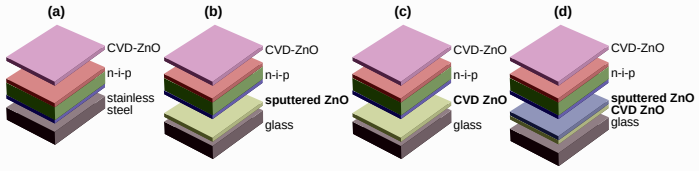

Fig. 8.1: Four different back-TCO interfaces onto which we deposited a n-i-p cell.

nature of the underlying back-TCO. We deposited the same n-i-p type μc-Si:H cell on stainless steel substrates coated with four different TCOs: CVD ZnO, sputtered ZnO, CVD with a sputtered ZnO on top and finally a stainless steel plate, see Fig. 8.1.

Questions on the interfaces of the solar cells are easy to investigate on the layers deposited at the end of the fabrication process because of the better access to this films. But the here investigated interface of the back-TCO / n-layer of the n-i-p solar cell is not directly accessible. Since most of the light is absorbed within the first 2μm of the absorber, only the long wavelength part of the light spectrum reaches the back-interface under normal illumination. In this situation, we turned the light source to the back-side of the solar cell in order to illuminate the cell not from the p-side (the normal configuration for thin-film silicon solar cells[1]) but to illuminate the cell trough the glass substrate, the back-TCO and the n-layer. Under the n-side illumination, more information on the performance of the junction near the back-interface can be obtained. The method of n- and p-side illuminated cells is also used in the chapter on solar cells of the dilution series, see section 9.1.1.

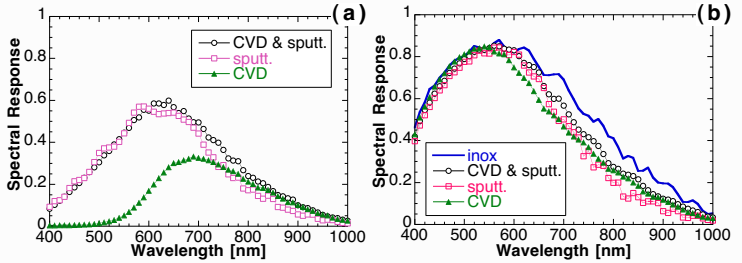

Fig. 8.2: (a) quantum efficiency illuminated from the n-side and (b) illuminated from the p-side: Back-contacts made of stainless steel (inox), CVD ZnO covered with a sputtered ZnO, sputtered ZnO and CVD ZnO on glass respectively.

In Table 8.1 the role of this first interface of the back-TCO and the n-type film becomes evident, if considering the cell characteristics. There is a close link between the type of TCO used and the performance of the solar cell. The best conversion efficiency is obtained on the reference substrate without

[1]The reason for normal p-side illumination comes from the drift driven a-Si:H solar cells, where the hole mobility is smaller than the mobility of electrons[38].

Table 8.1: Solar cells on four different back-contacts.

Nb.	TCO type	V_{OC} [mV]	FF [%]	$V_{OC} \cdot$ FF [a.u.]	J_{SC}: n/p $[\frac{mA}{cm^2}]$	ratio [n/p]	η [%]
Ib	CVD	438	64.2	281	5.7 / 17.6	0.32	4.9
IIb	Sputtered	460	69.0	317	10.9 / 17.1	0.64	5.4
IIIb	CVD and Sputtered	454	68.3	310	11.9 / 18.7	0.64	5.8
IV	Stainless steel	450	71.6	322	n.a. / 20.9	n.a.	6.7

any ZnO, the next best cell is fabricated on the combined ZnO-back contact (a textured CVD ZnO covered with the flat sputtered ZnO), see also Fig. 8.2, where the full quantum efficiency curves are given.

These observations may have several reasons: 1st all back-ZnO contacts have different surface roughness. This goes from the flat (rms of 4nm) sputtered ZnO to the intermediate roughness of the combined CVD & sputtered ZnO up to a rough (60nm) CVD ZnO. Note that the surface roughness plays a decisive role in the nucleation of the silicon film, see section 8.1.2. Then a 2nd difference of the cell interfaces may origin from a different chemistry of the ZnO films, since the CVD-ZnO is boron doped whereas the sputtered ZnO is aluminium doped. Up to now, no measured evidence for or against this second hypothesis could be given (e.g. SIMS data were not satisfactory clear); see also section 8.1.2 for a discussion on the n-i interface.

8.1.1 Interpretation: back-interface

For interpretation, the quantum efficiency data may be subdivided in three intervals, a first range up to 520nm, the second from 600nm to 800nm and the third from 800nm to 1000nm. Quantum efficiency measurement illuminated from the n-side is zero up to a wavelength of 520nm on the back-contact with CVD ZnO. On the two sputtered samples a considerably higher signal is measured and no difference between the two ZnO types is apparent, but the values obtained by the n-side quantum efficiency curve still remains below the values obtained for the p-side illuminated quantum efficiency curve of the cell. In the last interval only, the quantum efficiency curve of the cell with CVD ZnO gains over the quantum efficiency curves for the two other cells: this is an effect of the good light scattering behaviour of the textured, rough CVD ZnO. In all three curves of p-side illuminated quantum efficiency data, there is a slight dip in the region of 600nm to 800nm which is in fact often observed to disappear for cells on optimised back-reflectors.

8.1.2 Discussion on the n-i interface

Crystallographic observations help here to highlight one facet of the situation at the n-i interface. Keeping in mind that not only the physical (e.g. crystallographic) but also chemical (out-diffusion) and electronic (transport) aspects play important roles in this question.

The back-TCO and the electrical characteristics are correlated: The observations of low quantum efficiency curves of cells on CVD-ZnO goes in parallel with the poorly formed n-film visible in the TEM images. In the following paragraphs, we present possible explanations to this.

The Transversal Electron Microscope (TEM) allows for a close look on the nucleation of microcrystalline films on CVD and sputtered ZnO, see Fig. 8.3. Measurements on the dilution series cells (i.e. on a similar cell, but not on this specific "back-TCO" cell) reveal a systematically denser crystalline structure of the n-layer on sputtered ZnO than on CVD ZnO, i.e. a more crystalline n-film grows on sputtered ZnO compared to CVD ZnO. A consequence of this different n-layer is that the beginning of the intrinsic absorber-layer consists of a mixed-phase layer (amorphous and microcrystalline parts). This layer thickness is reported to vary from 140nm for cells on sputtered ZnO to 200nm for cells on CVD ZnO [3] and is sometimes referred to as 'incubation layer'. For a precise definition of this term, see the section 1.6.4.

Based on the increasing absorption depth for light of increasing wavelength, a zone within the n-layer and the beginning i-layer can be made responsible for the non-existent convertible generation of carriers for the cells on CVD-ZnO, see Fig. 8.2(a). Whether this is due to an optical problem (no photon absorption) or to an electronic problem (no electrical field, and thus no carrier separation) is a fundamental question exceeding the frame of this work. The junction lacks an electrical field within something like 100nm of the n-i interface. The most plausible explanation for the poor n-film quality is a difference in surface roughness of these two ZnO types (rough CVD ZnO and flat sputtered ZnO), since the growth on an inclined and on a textured surface is not the same as on a plane surface [61].

A possible contamination by out-diffusion of ZnO-doping molecules (in the case of CVD: diborane, in the case of sputtered ZnO: aluminium) into the n-film is a further hypothesis. The doping mechanisms in ZnO are not the same as in silicon. Since it is not yet fully understood whether the doping of CVD ZnO by boron is a substitutional or a interstitional mechanism, nothing can be said on the binding energies and, thus, on the diffusibly of the dopant in the ZnO. Considering the similar density of carriers in the two materials (at room temperature in the n-type silicon film n=$8{\cdot}10^{19}$ to $3.6{\cdot}10^{20} cm^{-3}$, see ref. [14] and for CVD ZnO N=$4.5{\cdot}10^{20} cm^{-3}$, see ref. [22]) a diffusion may

indeed occur. No measured evidence supports this hypothesis yet, and at present it can be neither proved nor denied.

Among the reasons for this lack in crystallisation quality of the beginning i-film, a phosphorus contamination due to the precedent deposition of the n-film can be excluded: This common problem of contamination in cells fabricated in a single-chamber deposition system would disturb the whole batch of cells, i.e. independent of the back-TCO. This is not the case here. Because the quantum efficiency values below 520nm are non-zero on the two sputtered back-contacts of that batch, a phosphorus contamination can be excluded.

Another explanation may be the atomic surface states of CVD ZnO, which are not inert at all. These ZnO surface states may be leading to interactions between the ZnO and the deposition plasma of the n-type film in growth. Thus particles of zinc, oxygen, silicon and phosphorus might get mixed together in the plasma process and create an n-film of a less favourable quality on CVD ZnO – something which does not happen on sputtered ZnO. The term of 'quality' refers here exclusively to crystallographic observations made by TEM and no doping profile was analysed.

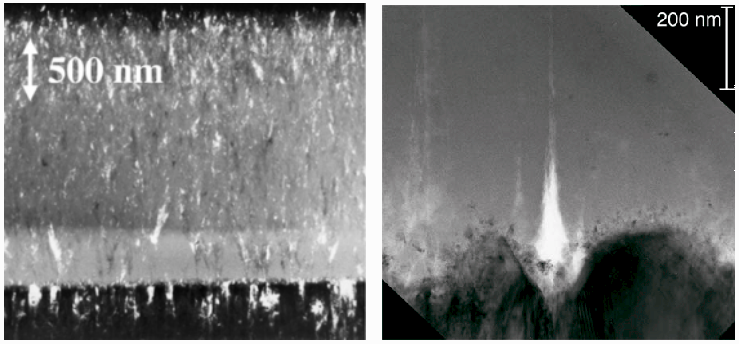

Fig. 8.3: (a) TEM dark field micrograph of a microcrystalline n-i-p solar cell deposited on sputtered ZnO. ZnO is at the bottom of the picture, n-type μc-Si:H layer appears as a thin dotty layer. (b) TEM bright-field micrograph of the ZnO-n-i interface of a solar cell deposited on CVD ZnO. ZnO tetrahedrons are at the bottom of the picture. Note the disordered grainy contrast of the n-layer. A crack/void at the bottom of the ZnO valley appears bright; source: Bailat et al. [3]

A last hypothesis may be a difference in the phosphorus diffusion from the n-layer into the first part of the i-layer. This explanation seems not to be very plausible thus.

The picture of the correlation of growth and device performance becomes steadily more clear: TEM investigations on solar cells (not on layers as in Fig. 1.16) show a direct growth of the i-layer at nucleation seeds on top of the doped n-layer. No continuously amorphous incubation layer but exclusively a mixed-phase is observed for all cells of the dilution series.

If electrical cell properties of the dilution series (c.f. chapter 9) and microstructural TEM-observations are compared, there is a proportional relation between the value of V_{OC} and the thickness of the mixed-phase layer. Often, an increase of V_{OC} is accompanied by a decrease in J_{SC}, as observed in many n-i-p cell optimisation runs (see also section 9.1.5 on this issue). The presence of a certain amount of amorphous phase surrounding the crystalline grains favours a high value of V_{OC}, probably thanks to the excellent passivation properties of a-Si:H. But if this mixed-phase layer is too thick, no beneficial effect but rather an unsatisfying device results. For good current conduction, a certain density of crystalline grains already from the first few nanometers of growth onwards seems to be necessary: this may explain the trade-off we often observed between cells with good V_{OC} values and cells with high J_{SC} values. Maximum conversion efficiency seems to be restricted to the small region of already reasonably high V_{OC} but still good enough J_{SC}.

Additional detailed TEM investigations [96] on the present dilution series for layers and full solar cells are under way at the time of writing [4]. But some further questions concerning the role of textured substrates on the growth of crystalline silicon grains within the μc-Si:H layer, the competing mechanisms of grains touching each other, formation of cracks and all questions on how photogenerated carriers are transported within such mixed-phase material (transport along the grain boundaries or inside the crystalline grain, percolation effects) are still under discussion and not fully understood.

8.2 Optimisation of μc-Si:H n-type films

The n-type film has a wide range of requirements: the μc-Si:H film has to grow properly on the back-contact (often ZnO but also steel is used), thus there is a crystalline nucleation problem; furthermore the very thin film (20nm) has to be well doped and a high optical transparency is necessary, if the underlying B-R should perform correctly.

A study of the optical transparency is carried out in order to possibly explain the poor quantum efficiency of some n-i-p solar cells if illuminated from

the n-side (see section 9.1.1). The structure glass/ZnO/n-film is measured with the spectrometer for an "old" (not yet optimised) n-film, and a newly optimised type of film. The case of no film at all, thus just the glass/ZnO interface is compared as well in Fig. 8.4.

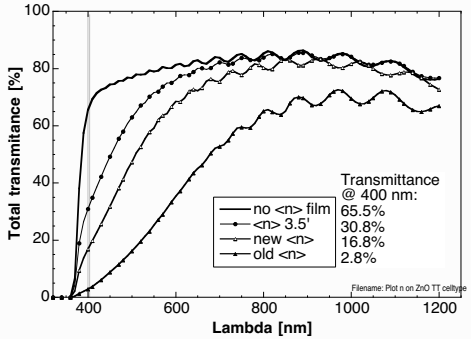

Fig. 8.4: Total transmittance of a glass/ZnO/n-film structure, where the thickness and quality of the n-film is varied.

Best transmittance is obtained for the case where no n-film is deposited onto the standard CVD-ZnO back contact. A trade-off between reasonable thickness and still good enough transmittance (especially in the long-wavelength region) is found for the third curve from top. The lowest transmittance of the old and not optimised film is not acceptable.

Thus in summary the n-film is a crucial step in the deposition of n-i-p solar cells and must fulfil the following requirements:

- The roughly 20nm thin film needs to be correctly doped in order to build the n-i-p junction.
- The absence of any amorphous incubation layer is desirable.
- A good electronic contact to the substrate or TCO and to the the i-layer.
- A correct crystallinity to facilitate the growth of the μc-Si:H i-type absorber film is required.
- A highly optically transparent n-film in the long wavelength part of spectrum is necessary for good B-R usage.

8.3 Microcrystalline solar cells

In 3 years time, over 230 functional cells could be fabricated. The μc-Si:H n-i-p solar cell with the best conversion efficiency η is presented in Fig. 8.5. We observed systematically, as reported in section 9.1.5, a divergence of cells with high V_{OC} values against cells with high J_{SC}. In fact, different classes can be formed of best V_{OC} value, best J_{SC} value and best conversion efficiency. The 'state of the art' cell in one category is rarely the state of the art in another. Thus the candidate reported here as the best n-i-p cell is a trade-off of several categories.

Cells of maximum short-circuit currents J_{SC} could be achieved exceeding $24\frac{mA}{cm^2}$, but its V_{OC} value is at position 100 of the decreasingly sorted list of V_{OC} values. The cell with the best conversion efficiency (η=7.8%, V_{OC}=461mV, FF=73%, J_{SC}=23.1) lies within the top five J_{SC} values and is reported in Fig. 8.5. On the other hand the cell with the best V_{OC} value reaches only a rank of 66 in the list of J_{SC} values.

Note that the maximum n-i-p cell conversion efficiency is thus fabricated first with a good J_{SC} and second with a good V_{OC} value.

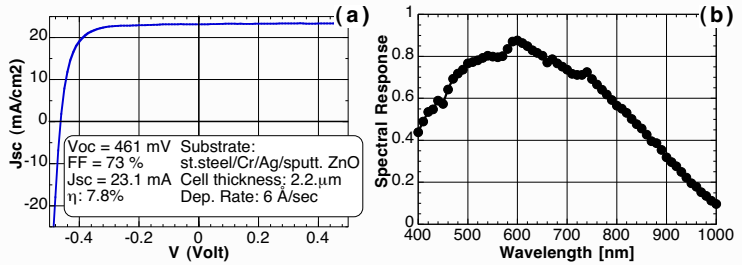

Fig. 8.5: The best μc-Si:H solar cell fabricated on steel/hot silver/ZnO substrate: (a) I-V curve (b) quantum efficiency curve.

8.4 Micromorph solar cells

The combination of a microcrystalline cell and amorphous cell (the micromorph solar cell) gives an other image if looking at the statistics of the cell performances.

The best conversion efficiency of micromorph cells are, unlike the microcrystalline cell, obtained with the cell of the highest V_{OC} value and only the second criterion is the J_{SC} value.

The best micromorph cell was entirely fabricated at IMT on a B-R from Jülich during the NEST project; the initial conversion efficiency $\eta = 11.2\%$ is given in Fig. 8.6.

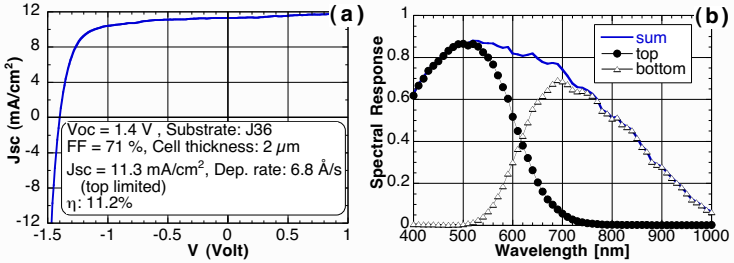

Fig. 8.6: The best micromorph solar cell fabricated on steel/hot silver/ZnO substrate: (a) I-V curve (b) quantum efficiency of the amorphous top cell, the microcrystalline bottom cell and the sum of both.

8.5 Conclusions

8.5.1 Three back-reflector types

Apparently, a high total reflectance is a necessary but not sufficient condition for powerful back-reflectors for cell manufacturing. The best total and diffuse reflectance values on the Jülich series were obtained using hot silver on stainless steel substrates; a haze of H=0.96 (with RT=0.78 and RD=0.75) was obtained on sample nb. J37. More total reflectance and an acceptable haze of H=0.73 (with RT=0.94 and RD=0.68) on sample nb. J32 (etch 30 sec). These average values are always taken over the interval ranging from 650nm up to 1200nm.

Note that on exactly this series of back-reflectors of increasing etch time the sample nb. J32. (etch 7 sec) yields a maximum short-circuit current with a haze of H=0.57 (with RT=0.91 and RD=0.51) and a structure of glass/silver/ZnO. AFM surface scans are used to interpret the surfaces and to correlate cell performance and surface topology. These evaluations of the B-R surfaces should give hints for further reflector design.

The best parameters for the textured silver B-R made at IMT are H=0.93, RT=0.93, RD=0.70. These spectrometry results of haze factor, total and diffuse reflectance show, thus, that the recently developed substrates are at least as good as the formerly available Jülich type substrates.

The main benefit of the series of copper/polyimide based substrates (low cost, flexible B-R) is opposed to the technological problems encountered in the fabrication of solar cells. These substrates systematically destroyed the junction of the solar cell, probably due to a out-diffusion problem. With the introduction of diffusion barriers (silver, CVD-ZnO and sputtered ZnO) the cells operated normally, but the benefit of the copper was lost again.

8.5.2 Designing back-reflectors

Light-trapping for solar cells has been a topic for over 30 years. Two schemes are reported: 1st the naturally grown surface texture and 2nd the optical diffraction grid. The surface texture structure is well implemented at IMT since January 2001 by the combination of hot silver and ZnO:Al films by sputtering on stainless steel substrates. The short-circuit current is improved from $18.6\frac{mA}{cm^2}$ to $21.6\frac{mA}{cm^2}$ for a solar cell deposited on a flat silver or a textured silver B-R respectively, which is a 33% increase. There is still room for improvement to reach the limit of 30 $\frac{mA}{cm^2}$ predicted by the simulations by Springer et al. [78].

The recent development of B-Rs based on naturally textured silver/sputtered ZnO at IMT is an excellent base for solar cells with high short-circuit currents exceeding $24\frac{mA}{cm^2}$. In a recent publication [107] it semes possible to fabricate μc-Si:H solar cells reaching a J_{SC} of $29\frac{mA}{cm^2}$. This shows the powerful possibilities of optically well designed solar cells. On the other hand is the question, which parameter (i.e. J_{SC} or V_{OC}, FF) can give room for further improvement. In the case of μc-Si:H n-i-p solar cells, after a well designed B-R, there may be quicker improvements in the cell interfaces (i.e. V_{OC} and FF) than in a further optimisation of the diffusely scattering B-R. A key parameter for higher efficiencies in μc-Si:H cell is in our opinion the V_{OC}. Improvements in V_{OC} can be made by deposition close to the transition regime (cf. section 9.1). However, due to the sharpness of the latter in our case, it is difficult to achieve larger V_{OC} without decreasing in FF and J_{SC}.

The theoretical analysis for the requirements of B-R for microcrystalline silicon solar cells gives a wavelength $\lambda_0 = 866nm$ where a geometrical light-trapping scheme with optical diffraction grids has to be placed. An implementation of such diffraction grids is reported in literature [18] only for the case of amorphous solar cells (where no big increase of light trapping in the long wavelength spectrum is possible).

Chapter 9

Dilution series on solar cells

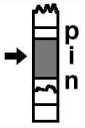

The dilution series consists of one batch of solar cells where the silane concentration (SC) was varied from 5%, 5.5%, 6%, 6.5%, 7%, 7.5% with SC$\doteq \frac{[SiH_4]}{[SiH_4+H_2]}$. This variation of the feedstock gas supply of the absorber layer changes its phase from microcrystalline (at 5% SC) to amorphous (at 7% SC). All other deposition parameters as the n-layer and p-layer were not changed for the whole series of cell fabrication. The solar cells were deposited in a single-chamber VHF-GD reactor at plasma excitation frequencies between 70 and 130MHz. Typical deposition parameters for the intrinsic layer are: base pressure of the vacuum chamber better than $4{\cdot}10^{-8}$mbar, deposition pressure p=0.1-0.9mbar, applied plasma power P=5-30W, substrate temperature around 200°C. A gas purifier was used to avoid incorporation of detrimental oxygen contamination [86]. These conditions lead to deposition rates in the region of 8 to 10Å/sec, cf. figure 1.3. For each dilution step the solar cell is deposited on glass (AF45 Schott) substrates coated with a back-TCO with CVD ZnO on one half and a sputtered ZnO on the other half of the whole deposition area. The top-TCO contact of all cells are made of CVD ZnO. In parallel to the solar cells, exactly the same absorber layer were fabricated on glass, in order to investigate both layer quality and solar cell performance, and eventually conclude in similar trends on the solar cell performance as well as on the layer properties.

This dilution series of solar cells and i-films on glass lead to several publications to be cited [19, 3, 4, 16, 101, 102, 103, 104].

9.1 V_{OC}, Fillfactor, J_{SC} and η

With the increase in the silane concentration from 5 to 7%, the electrical characterisation (see Fig. 9.1) of the devices show a clear increase of the open-circuit voltage V_{OC}, a slight decrease of the short-circuit current J_{SC}, a decrease of fill-factor on CVD and an increase of fillfactor on sputtered ZnO back TCO. In summary the conversion efficiency η remains roughly constant on a plateau for cells on sputtered ZnO, whereas conversion efficiency drops on increasing SC. The electrical characteristics of the same solar cell of the dilution series deposited on CVD-ZnO follow different trends than on sputtered ZnO.

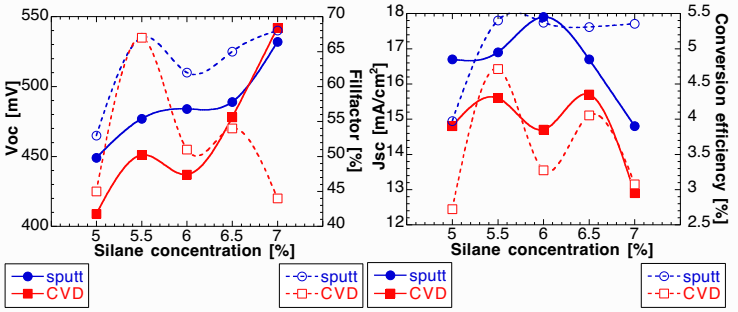

Fig. 9.1: (a) V_{OC} and FF of cells in the dilution series made on CVD and sputtered ZnO (b) J_{SC} and conversion efficiency.

The series of solar cells on CVD-ZnO has an overall lower electrical performance as the series of solar cells on sputtered ZnO – not only in this dilution series here, but also on several other deposition runs. Within this work, CVD-ZnO back-TCO and the n-i-p cell could not be optimised fully together; it never was a project aim either. Other research projects on p-i-n cell optimisations showed excellent cell performance of cells optimised on CVD-ZnO [54]. One characteristics of this interface optimisation is shown in Fig. 9.3(b) where the quantum efficiency is nearly the same independently whether the cell is illuminated from the p-side (normal illumination side) or from the n-side of the solar cell.

The question is, whether the source of the problem can be found at the interface back-TCO / cell. We wanted to investigate in this question and propose in the next section a well suited tool to better highlight the functioning

of the solar cell at the back-TCO interface[1].

9.1.1 Quantum efficiency n/p side

Definitions

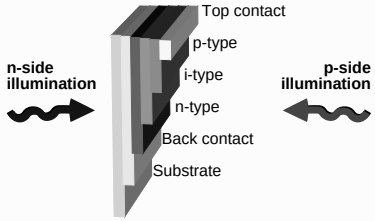

Fig. 9.2: The configuration of the n-side and p-side illuminated solar cell.

The two thin-film silicon solar cell structures differ in their deposition order, e.g. n-i-p designates the *substrate* type cell where first the n-film is deposited onto the substrate (e.g. metals or plastics), then the intrinsic i-layer and then the p-layer, whereas the p-i-n designates the *superstrate* cell, where first the p-layer is deposited onto the substrate then follows the i-layer and finally the p-layer.

Common to both solar cell structures is that normally the p-side[1] is illuminated. In consequence, n-i-p cells are always illuminated through the doped layer which was deposited last of the deposition process. This is in contrast to the p-i-n structure on glass, where the cell is illuminated through the doped layer which was deposited first (before the the i-layer and n-layer). In either structure, under a regular p-side illuminated cell of a thickness of about 2μm, only light above a wavelength of 700nm hits the n-layer at the rear. (The deposition order of the different doped layers has nothing to do with the terms used in context of illumination, where the top-TCO designates the first layer exposed to the light source and the back-TCO or back-reflector designates the part where light arrives only after one cell-passage.)

In the solar cell deposition process, the very first nanometers of silicon film are the most crucial task, in the case of the n-i-p device this refers to the interface TCO/n-layer as well as the interface between n/i layer. The

[1]Note, because of regularly illuminating thin-film solar cells from the p-side, the back-TCO interface is in the case of a n-i-p solar cells always at the beginning of cell growth, whereas the back-TCO is at the end of the cell deposition process for p-i-n solar cells.

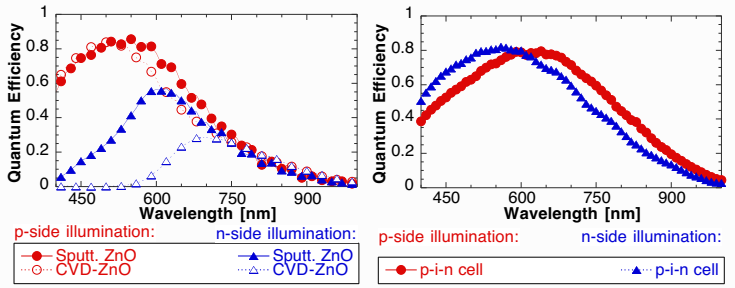

Fig. 9.3: Quantum efficiency from the p-side and the n-side: (a) two solar cells of the dilution series deposited both at 5.5% SC once on sputtered and once CVD-ZnO respectively. (b) A p-i-n cell optimised on CVD-ZnO; source: J. Meier.

difficulty lies in the fabrication of a crystallographically and electronically correct base layer on which the intrinsic absorber film can start growing correctly. Even though a n-type film is an 'easy' film to optimise, not much research has been done on its optimisation in recent years.

With the method of n-side illuminated solar cells, a good analysis tool is found for the development of the back-TCO interface, since the junction is now highlighted not only with the long-wavelength part of the spectrum (near infrared), but also with the short-wavelength, high energy-blue part, see Fig. 9.2.

In this section, first the role of the type of TCO on the performance of a standard solar cell is reported. Then the results of quantum efficiency measurements made on the dilution series of solar cells is given.

Fig. 9.3(a) shows quantum efficiency curves of two n-i-p cells, one with an optimised interface back-TCO / n-layer on sputtered ZnO and another n-i-p cell on an un-optimised interface. The p-i-n cell of Fig. 9.3(b) fabricated on CVD-ZnO has a nearly symmetric quantum efficiency curve which indicates a well tailored interface to the CVD-ZnO contact. Longer optimisation process of the cell-ZnO interface and more experience led to this p-i-n solar cell whereas n-i-p cell development is not at this stage yet.

9.1.2 The p-side illuminated case

The quantum efficiency curves of the dilution series are summarised by the short-circuit currents J_{SC} in Table 9.1. All J_{SC}values of p-side illuminated cells are systematically higher than the J_{SC}values of n-side illuminated cells, independently of the back-contact material (here: sputtered ZnO or CVD ZnO). This observation holds for most n-i-ptype cells fabricated over the last few years. A second observation is the lower J_{SC}values for cells deposited on CVD ZnO compared to cells deposited on sputtered ZnO - independently of the illumination side. Such a behaviour is, thus, not just typical for the *dilution* series but is a general observation for these two kinds of back-contacts, see also Fig. 8.2 in section 8.1.

When measured on CVD and on sputtered ZnO substrates (see Table 9.1) even though a systematically better J_{SC} is measured on sputtered than on CVD ZnO. This is not a recently observed trend but is very consistent over the last few years of cell manufacturing;

Table 9.1: Quantum efficiency on dilution series: p-side and n-side illumination

Silane Concentration [%]	**p-side** J_{SC} Sput. ZnO $[\frac{mA}{cm^2}]$	**p-side** J_{SC} CVD ZnO $[\frac{mA}{cm^2}]$	**n-side** J_{SC} Sput. ZnO $[\frac{mA}{cm^2}]$	**n-side** J_{SC} CVD ZnO $[\frac{mA}{cm^2}]$
5.0	16.7	14.9	14.6	4.3
5.5	16.9	15.6	9.8	4.5
6.0	17.9	14.8	12.4	4.7
6.5	16.7	15.7	9.4	4.7
7.0	14.8	12.9	5.9	3.8

9.1.3 The n-side illuminated case

Surprisingly, no significant trend of the quantum efficiency data in function of dilution can be observed on the cells deposited on CVD ZnO in the n-side illuminated case. There is a systematically low signal up to a wavelength of 520nm, only in the typical microcrystalline absorption region of the spectrum (above 650nm) the signal of the n-side coincide with the signal from the p-side illuminated cell; this behaviour is reflected also in the J_{SC} value, see Table 9.1.

A completely different behaviour is reported for the cells deposited on sputtered ZnO where the J_{SC} gets smaller for silane concentrations ranging

from 5% up to 7% or in other words: the more of an amorphous phase is present in the absorber layer, the lower that J_{SC} gets. The solar cell with 5% SC on sputtered ZnO has an almost symmetric quantum efficiency if observed from the n-side or the p-side, whereas the solar cell with 7% SC on sputtered ZnO has a poor quantum efficiency which is comparably poor as the quantum efficiency of all cells on CVD ZnO.

This trend is expressed in Fig. 9.4 where the difference of the short-circuit currents from the two illumination sides is plotted. The smaller the difference of the p-n side QE, the better the symmetry of the curves. Another correlation to this tendency is based on the TEM observations: The contact height 'h' is defined as the distance from the beginning of the i-layer growth to the place where the cone-shaped crystallites start touching each other (this layer is also referred to the mixed-phase layer; see the sketch in Fig. 1.15). This mixed-phase layer is observed to get thicker for higher silane concentrations. In Fig. 9.4 the difference of the J_{SC}values (p-side minus n-side illuminated QE) is reported against SC. The contact height 'h' is reported as second y-axis and a similar trend for the two y-axis is apparent (see also section 8.1.2 for more on TEM on cells).

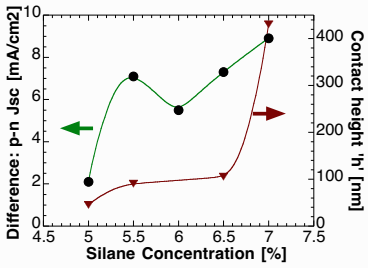

Fig. 9.4: The difference of the J_{SC} illuminated from the p-side and the n-side of cells deposited on sputtered ZnO – the smaller the difference, the more symmetric is the quantum efficiency.

9.1.4 Conclusions: n/p side QE

The method of n-side illumination gives a qualitative information on the junctions of a thin-film device. The 'ideal' solar cell with identical quantum efficiency curve for both illumination sides is best approached by the p-i-n

type cell shown in Fig. 9.3; no similar n-i-p type device is observed in our lab so far.

The concept of n-side illuminated solar cell was investigated further in a publication by Gross et al. [24] for p-i-n and n-i-p devices on glass: no differences in the collection of photogenerated electrons or holes were observed here when illuminated from the two sides of the device. The authors conclude that μc-Si:H solar cells can be illuminated from either side without any significant impact on their performance. This is a rather surprising finding and should be confirmed independently.

The comparison of solar cells on different substrates shows the importance between a reference standard cell and its substrate; one working deposition process for a device can, in fact, hardly be copied onto another substrate without an adaptation of interfaces. The reason for this is found in the quality of the n-type layer. A slight difference of quality in electronic and/or crystallographic properties changes the whole solar cell performance.

In the dilution series, once more the difference of sputtered and CVD ZnO can be observed on the n-i-p solar cells. The trend towards lower J_{SC} for absorber layers with higher amorphous volume fraction is consistent with the observations of the previous section(9.1.3): the thicker the mixed-phase layer at the n-i interface gets, the lower the value of J_{SC}. The combination of high J_{SC} and high V_{OC} to fabricate high efficiency μc-Si:H solar cells seems to lie in an optimised interface of the n-film and i-film w.r.t. mixed-phase layer thickness.

9.1.5 The Voc-Jsc problem

The evaluation of the solar cells (deposited on glass substrates) of the dilution series showed a clear increase of the V_{OC} value up to 530mV and the J_{SC} value decreases down to $15\frac{mA}{cm^2}$ if the SC is increased towards more amorphous growth conditions, see Fig. 9.1. On the other hand, solar cells deposited on the diffusely scattering back-reflectors (based on surface-textured Ag/sputtered ZnO) reach maximum J_{SC} values exceeding $24\frac{mA}{cm^2}$ but the V_{OC} value remains within a range of 440 to 470mV.

In order to increase overall conversion efficiency, we tried hard to combine the two properties (high current and high voltage) with limited success: Too often the so called V_{OC}-cell on top of the optimised B-R lacks in current and as soon the J_{SC}-cell is measured the voltage dropped.

These two cell types are technologically based on variations of SC within the intrinsic absorber layer, like in the dilution series. Apparently, the variation of the i-layer as a whole element for the solution of the J_{SC}-V_{OC} problem is not satisfying. This lets us conclude that if not the bulk i-layer then the

interfaces of the i-layer should result in an overall increase of conversion efficiency. The μc-Si:H n-i-p cell development could be guided into this direction, at the time of writing this approach is not terminated yet.

Essential to the continuity of this work are a reliable and reproducible fabrication process. That is why the single-chamber deposition system will be upgraded: a double-chamber system facilitates separated deposition of doped and intrinsic films and a plasma cleaning procedure will permit a periodic system clean without a too long down-time of the fabrication process (e.g. interruptions because of lost base-pressure, or after the removal of electrode parts for cleaning, changes in plasma impedance occurred).

9.1.6 Variation in E_g

The optical gap of thin amorphous silicon films is often determined with Tauc's plot which is based on optical absorption data as measured e.g. by PDS. The optical bandgap E_{Tauc} is obtained by extrapolation of the linear region in a $\sqrt{\alpha \cdot E(E)}$ plot, where E_{Tauc} is the energy value at the intersection of the fit with the energy axis.

Many experts may ask, if the change in silane concentration (SC) results in the deposition of the μc-Si:H absorber material with a gradual change of the bandgap E_g of the material, like it happens e.g. in amorphous silicon films: Platz [65] states an experimentally confirmed linear dependency of the optical band-gap with hydrogen dilution within the amorphous growth regime (linear fit with a slope of $\approx 8meV/at\%$). A completely different situation governs μc-Si:Hfilm material. This method is not applicable to μc-Si:H films. Here some reasons:

- For a-Si:H, there is a change of the gap because with an increased hydrogen content, electron states are removed from the top of the valence band in Si-H alloy thus widening the (Tauc) gap. For μc-Si:H material there is no such effect since hydrogen is on crystallites surfaces and in surrounding amorphous tissue but percents of hydrogen can not possibly be dissolved in crystallites, the optical gap of μc-Si:H is governed otherwise.

- Tauc's plot is not a very useful method for μc-Si:H films at the transition to the a-Si:H phase: the initially high surface roughness of a microcrystalline film decreases rapidly after the transition to amorphous phase. Thus, the absorption is increased by up to a factor of 12 due to light trapping on the rough surface [66] compared to absorption on a flat surface. Every evaluation based on optical data within this

transition zone suffers from large uncertainties which in turn will make a correct determination of E_g more than difficult.

- The measurement of the optical absorption of a mixed-phase material such as microcrystalline silicon is not simple to interpret, because of the enhanced absorption of μc-Si:H material compared to a-Si:H material in the red-spectral region (about a factor 25). Even if the crystalline fraction of the material can be determined (e.g. by X-ray diffraction or by Raman spectroscopy) the exact optical path through the conglomerate of crystalline and amorphous material can at present not be determined. The PDS measure of absorption will always be biased by the heavily absorbing material, thus a plot of E_g in function of the SC will follow a step-function behaviour, i.e. low band-gap for low silane concentrations and a high band-gap for high silane concentrations.

Thus, there is no correlation possible between the optical absorption of films and the V_{OC} of cells of the dilution series - unless the tiny interval of half a percentage silane concentration (here between 6.5% and 7%), where the actual phase transition takes place, would be investigated.

Chapter 10

Thermography for shunt detection

Introduction

The local heating of a solar cell under bias-voltage is proportional to the local dissipated power, itself proportional to the local current if a fixed voltage is applied. Thus the thermography allows for the local current measurement under external bias. In order to increase the thermal resolution and the local resolution of the measurement, the bias voltage is applied periodically and the data is acquired in the lock-in mode.

10.1 Experimental

10.1.1 Cell structuring

After the deposition process of a solar cell, the active area is subdivided in order to measure several cells per deposition run. This cell structuring is essential to exactly define the cell surface for a correct J_{SC} value and reduce a lateral conductivity loss. It is done in industry by laser scribing whereas in the research lab, other possibilities are as well investigated, i.e. the structuring by P70 (see Fig. 10.1) or by masking parts of the cell during the last contact deposition process.

For cell structuring by the liquid plastic film 'P70', about 20 cells are painted by a paint brush on the top-TCO coated cell (overall surface of ≈16cm^2), see Fig. 10.1(a). The isolation of individual cells happens in two steps: First the painted dots (1 dot = 1 cell) are isolated on the level of the top-TCO by a chemical wet-etch, Fig. 10.1(b). No silicon is removed just

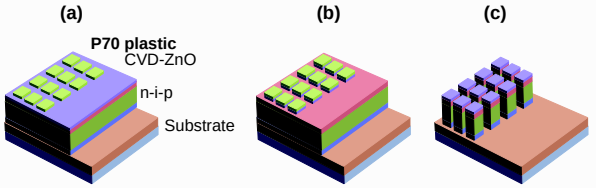

Fig. 10.1: Three step cell structuring: (a) sub-cells are painted by liquid plastic (P70) on top of the TCO coated cell; (b) the top-TCO is removed chemically, and (c) the silicon cells are isolated by plasma etch.

the TCO. Second the silicon solar cell is isolated by a plasma attack of the silicon layer, Fig. 10.1(c). Even though this method looks rather artistic, good results could be achieved by this lab-level cell structuring method.

Over the last four years, we used essentially the three structuring methods which are shown in Fig. 10.2 e.g. first the ITO front contact, then the P70 and the laser scribe on CVD ZnO front contacts. Since the small area of these solar cell does not generate high short-circuit currents, we rarely used metallic contact grids on top of the solar cells.

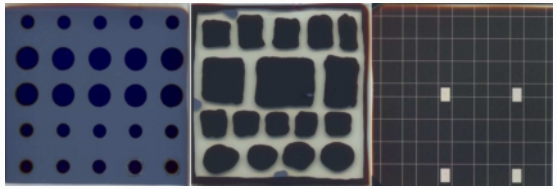

Fig. 10.2: Three solar cell substrates of 4x4cm^2 area which were structured by three different methods: (1) thin AR coating of ITO, (2) thick CVD ZnO structured by P70 plastic, (3) thick CVD ZnO structured by laser scribe.

10.1.2 Lock-in infrared thermography

The infrared thermography pictures were taken with a commercial lock-in thermography system TDL 384 M by the German company Thermosensorik GmbH (Erlangen). It consists of a Mercury-Cadmium-Telluride focal plane array with a resolution of 288 x 288 pixels at a fixed frame rate of 140Hz,

with 15Hz modulation frequency of the signal and 15min acquisition time; the solar cell is measured at both 0.5V forward and reverse bias voltages, the injected current reading has an offset of roughly 1mA and an error of about the same value, the IR image acquisition is not taken in the dark, but at a working lab-light level (roughly 0.01 sun); the temperature modulation scales: -0.2 to 2mK

The lock-in thermography results are usually represented as an amplitude image, a phase image, and a topography image, all appearing from the same measurement. The topography image is one single image of the thermocamera. The amplitude image is a measure of the local heat dissipation density. Hence, in this image strong shunts appear as bright spots or even "overexposed" (artificially enlarged), whereas weak shunts may remain invisible. In the phase image, which represents a measure of the local time delay of the thermal waves, both strong and weak shunts appear with a similar brightness.

The solar cell surface is protected from too strong a needle pressure of the probing top-contact by a small square piece of nickel, which is visible on the topographic camera images.

10.1.3 Cells investigated

Up to now, three microcrystalline n-i-p samples were analysed by Lock-In Thermography at the Max-Planck-Institut (MPI) Halle in the research group of O. Breitenstein:

1. P70 structured cell L260901G on back-reflector / steel
2. Laser structured L260901G on back-reflector / steel
3. Laser structured L130301G on sputtered ZnO / glass

The first two cells were sent to Halle in order to investigate the systematically low fill-factor (FF) on the laser-scribed cells compared to the P70 cells fabricated under the same deposition conditions onto comparable hot silver type back-reflectors, see table 10.1. The conclusion of this first run was, that there were not more shunts at the borders of laser scribed cells compared to the borders of P70 structured cells, as far as this visualisation method is able to detect.

The third sample was a better cell (considerably better $V_{OC}$and fill-factor) deposited on glass / sputtered ZnO and the hope was to find no shunts at all, but the people at MPI Halle could even find shunts on these cells.

In Table 10.1 statistics on the I-V data is shown. On the first sample 25 cells are compared and the best 12 cells were averaged, on the second sample

the best 13 cells out of 25 were averaged and on the third sample the top 15 out of 30 cells were averaged. The selection criterion was the product of $V_{OC}{\cdot}FF$, the second half of each data set was considered as non-relevant and thus not taken into account for a comparison of the three samples.

Table 10.1: Average and standard deviation of cell performance data of the three samples under thermography investigation: first two rows compare the same type of cell sample but different structuring, the last row is a better cell with laser structuring, where n is the number of measured cells per batch.

Cell nb.	Structured, batch	Mean V_{OC}[mV]	Std.Dev. V_{OC}[mV]	Mean FF[%]	Std.Dev. FF[%]	n
L260901G	Laser-BR	388	19	44	4	13
L260901G	P70-BR	433	12	54	5	12
L130301G	Laser-glass	513	17	61	2	15

10.2 Results

10.2.1 Cell L260901G

This first batch of cells was analysed to find an answer to the low fill-factor on laser-structured n-i-p cells as compared to P70 structuring of n-i-p cells. On the first sample (laser structured), five thermography images were taken of cells number 1, 7, 9, 12, 16 out of the list of the $V_{OC} \cdot$ FF-product containing 25 entries, so the best (B3) and the worst (C3) cells of that series are shown in the images below:

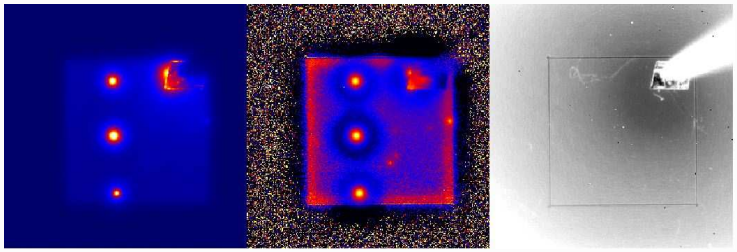

Fig. 10.3: Best laser scribed L260901G, B3: Amplitude, Phase, Topography, 0.5V 5.36mA applied; $V_{OC} \cdot$ FF=206, V_{OC}=0.406V, FF=51%, η=4.3%

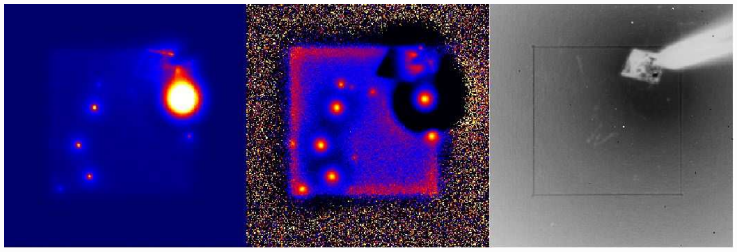

Fig. 10.4: Worst laser scribed, L260901G, C3: Amplitude, Phase, Topography, 0.5V 6.26mA applied; $V_{OC} \cdot$ FF=125, V_{OC}=0.339V FF=37% η=2.5%

On the second sample of the first batch (P70 structured), also five thermography images were taken of cells number 2, 3, 10, 14, 15 out of the list of the $V_{OC} \cdot$ FF-product containing 25 entries, so the second-best (A3) and the worst (E3) cells of that series are shown in the images below:

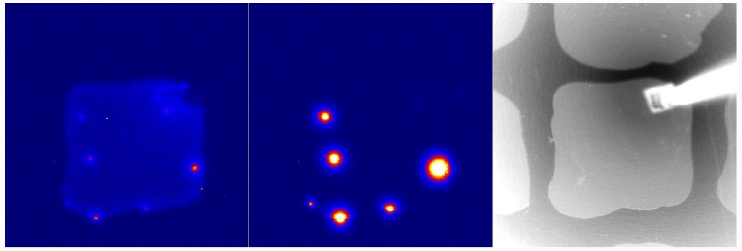

Fig. 10.5: Best P70 structured, L260901G, C3: forward 2.54 mA, reverse 0.68mA 1V, Topography; $V_{OC} \cdot$ FF=254, V_{OC}=0.445V FF=57% η=5.3%

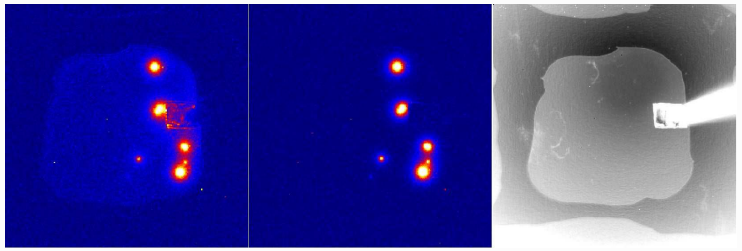

Fig. 10.6: Worst P70 structured, L260901G, E3: forward 5.33mA, reverse 0.97mA, Topography; V_{OC}·FF=180, V_{OC}=0.387V FF=46%

A more detailed analyse of the shunts on cell C3 of sample nb. L260901G structured by P70 follow here. The cell substrate was cleaned in acetone for 30 minutes in an ultrasonic bath, in order to remove loose particles on the surface. Even after this procedure, still many particles could be observed by optical microscopy on the surface of the cells.

Optical microscopy and SEM imaging (see Fig. 10.8) reveal particle size around 10μm some of them with parallel borders. Concentrating on spots number one (on the left border) and two (on the bottom right) of Fig. 10.7, further analysis of the nature of these particles is undertaken.

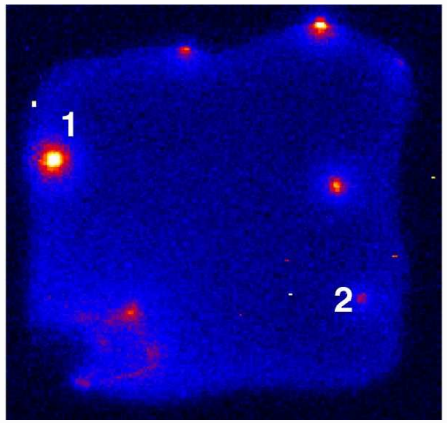

Fig. 10.7: Overview on cell P70-C3 with the two shunts to be analysed in more detail

The two shunts on sample P70-C3 are analysed as well by SEM at 10kV, X3700:

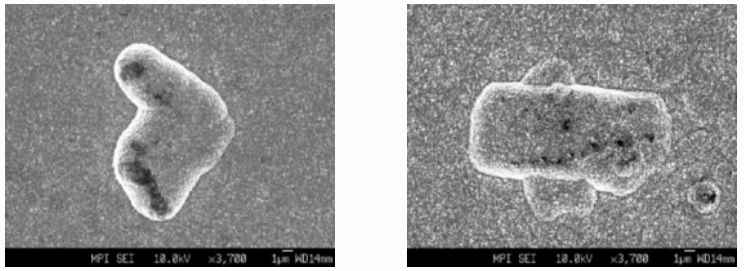

Fig. 10.8: SEM image of shunt number one and number two

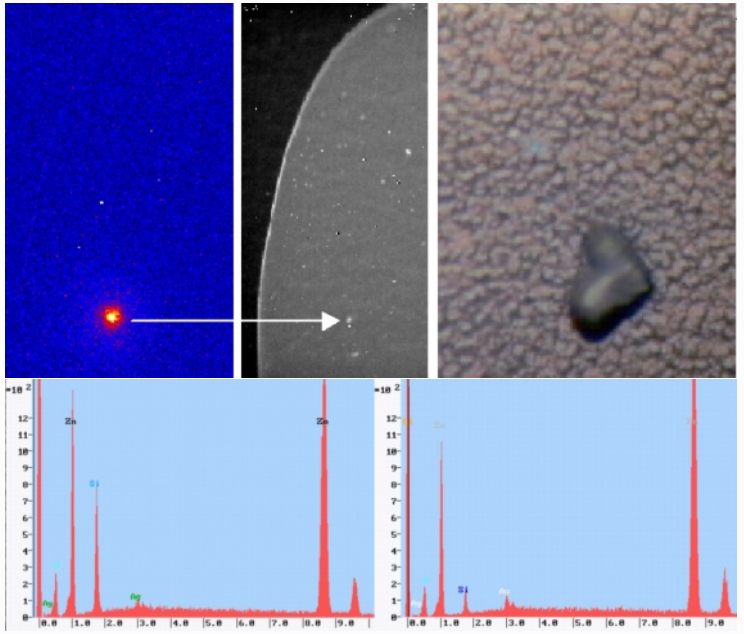

Fig. 10.9: The shunt can be identified in the optical microscope image (x1000) and EDX analysis show 24% Si on the particle and 6% aside of the particle, Zn concentrations for both locations above 76%

10.2.2 Cell L130301G

In this test, better cells were analysed in order to see whether there are shunts on all μc-Si:H n-i-p solar cells or not.

The laser structured cell-deposition on sputtered ZnO / glass has considerably better average performance (see table 10.1). The thermography imaging is performed on two candidates at extreme $V_{OC} \cdot$ FF values: the third best (D4) and the worst (E4) out of 30 cells are compared in the images below:

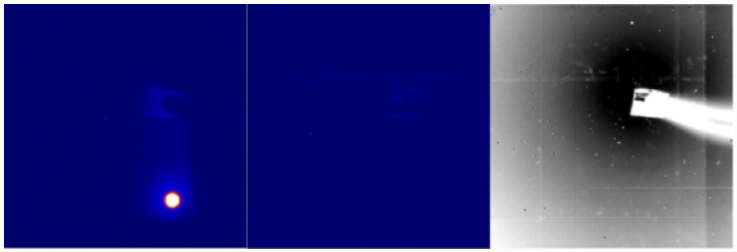

Fig. 10.10: Good laser scribed, L130301G D4; forward +0.5V, 3.68mA, -1 to 10mK; reverse -0.5V, < 1mA, -1 to 10mK; Topography; $V_{OC} \cdot$ FF=315, V_{OC}=0.518V, FF=61%, η=5.0%; non-ohmic shunt

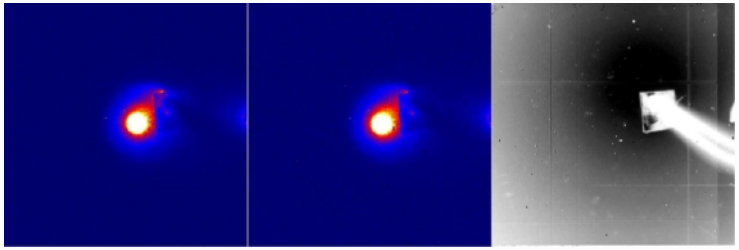

Fig. 10.11: Bad laser scribed, L130301G, E4, forward +0.5V, 5.73mA, -1 to 10mK; reverse -0.5V, 5.6mA, -1 to 10mK; Topography; $V_{OC} \cdot$ FF=079, V_{OC}=0.310V, FF=25%, η=1.0%; ohmic shunt

The observations of this series indicate the following correlations a weak non-linear shunt on cell D4 goes with a good I-V curve, whereas the worst solar cell of that sample has the strongest linear shunt.

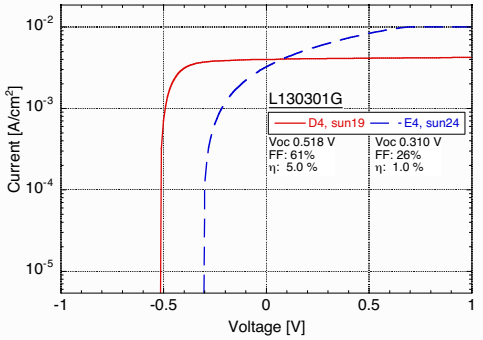

Fig. 10.12: The I-V curve of the good and the bad candidates which were analysed in this case

Some other cells (not shown here) of this second batch possess more border shunts than the first batch of cells, this indicates less optimised laser-scribe conditions for the later cells.

10.3 Conclusions

- Bad cells are dominated by shunts of an ohmic I-V characteristic (same appearance on the thermography image of the shunt in applied forward and reverse bias voltage)
- SEM images show two typical shunt particles of roughly 10μm size
- EDX micro-analyse indicate a silicon concentration of 24% of silicon on the shunt particles and 6% nearby the particle; the zinc concentrations are of 76% and 94% respectively
- Much more particles are visible than shunts: comparing the number of particles on the topography image and the number of shunts results in a ratio of nearly 1 to 100 of detectable shunts
- Good cells may still have a non-linear shunt problem and may thus be improved (fill-factor and V_{OC}) by the elimination of these remaining shunts.

Chapter 11

Conclusions of Part II

In conclusion of this second part on solar cell optimisations fabricated by the PE-CVD deposition process, the following can be said:

Solar cells were successfully fabricated onto a large variety of substrates such as stainless steel, flexible copper-coated polyamide films as well as on glass substrates with various back-reflecting (B-R) coatings. These different B-R coatings could be compared and classified against each other based on spectrometric reflectance measurements and on simple statistical sorting methods. The conversion efficiency η of μc-Si:H n-i-p solar cells could considerably be increased based on optical fine-tuning of the whole device:

1. The optical reflectance loss on completed solar cells can be reduced considerably by a front-TCO which is a surface textured CVD ZnO material instead of flat front-TCO.

2. The back-reflecting properties of the n-i-p cell's substrates influence directly (over the short-circuit current J_{SC}) the conversion efficiency.

3. The ratio of optical diffuse reflectance to total reflectance (the so called haze) turned out to be of little interest for a qualitative correlation of back-reflecting properties and cell performance. Only by considering both the total reflectance data together with the cell's quantum efficiency data, a nice correlation between back-reflecting properties and short-circuit currents could be sketched (see wet-etch series in section 7.2.1).

4. The back-reflector and the silicon solar cell form an 'experimental unity', which can not be optimised independently nor in parallel.

5. Calculations on the AM1.5 solar spectrum and the absorption of a 2μm thin microcrystalline silicon absorber material show: the spectral part

of interest for B-R optimisation lies at $\lambda_0 = 866nm$.

In this work, we introduced a systematic comparison of quantum efficiency data of the solar cell illuminated from the n-side with quantum efficiency data illuminated from the p-side. These curves turned up to be **asymmetric** and highlight a collection/generation problem at the n-i interface of our n-i-p cells whereas the i-p interface operates properly. We note that cells on CVD-ZnO back-TCO suffer from a larger lack of n-J_{SC} as compared to cells on sputtered ZnO back-contacts. The low n-J_{SC} value of cells on CVD-ZnO can be correlated to the contact height h of crystal grains (see TEM investigations in section 8.1.2 and the sketch in figure 1.15). Additionally, the higher the silane concentration of the absorber material the lower the n-J_{SC} value of the quantum efficiency.

Our best microcrystalline silicon solar cells in the n-i-p configuration fabricated: conversion efficiency η=7.8%, V_{OC}=461mV, J_{SC}=23.1$\frac{mA}{cm^2}$, FF=73%, deposition rate 6Å/sec; and our best micromorph tandem solar cells: initial conversion efficiency η=11.2%, V_{OC}=1.4V, J_{SC}=11.3$\frac{mA}{cm^2}$, FF=71%, deposition rate 6.8Å/sec.

Appendix A

Tables of the dilution series

The following table gives an overview of the widely characterised dilution series on solar cells and films.

All i-type layers of both cells and layers on glass are fabricated at a set substrate temperature of 225°C, 30W plasma power and an excitation frequency of 130MHz; the gas purifier was used.

Characterisation methods applied to these films: UV-Vis spectrometry, CPM, Raman spectroscopy, Atomic Force Microscopy, Transverse Electron Microscopy, dark conductivity σ_{dark}, Time Of Flight, Fourier Transform Infrared Spectroscopy.

These solar cells were measured by I-V characterisation, Spectral Response, Transverse Electron Microscope, Raman Spectroscopy.

Table A.1: List of films deposited on glass, sputtered ZnO coated AF45 glass and c-Si wafer at varying silane concentration (SC).

SC [%]	Film Name	Film Thickness [μm]	Deposition Rate [Å/sec]
5	L03029	2.1	6.3
5.5	L290199	2.4	6.4
6	L040299	2.4	7.8
6.5	L090299	2.3	8.5
7	L09029B	2.3	9.6
7.5	L250399	2	10.1
8	L290399	2	11.1

Table A.2: List of n-i-p solar cells at varying silane concentration (SC).

SC [%]	Cell Name	back-TCO type	V_{OC} [mV]	FF [%]	J_{SC} [$\frac{mA}{cm^2}$]	η [%]
5	L020399G	sput.	433	63	n.a.	n.a.
		CVD	400	60	n.a.	n.a.
5.5	L260299G	sput.	471	71	18.8	*6.3*
		CVD	428	67	14.8	4.3
6	L240299G	sput.	473	64	17.2	5.2
		CVD	420	63	15.0	3.9
6.5	L220299G	sput.	491	62	17.7	5.4
		CVD	470	63	15.6	4.6
7	L100299G	sput.	531	68	15.5	5.6
		CVD	596	29	0.5	0.5

Appendix B

Abbreviations

In this thesis, the following symbols and abbreviations were used:

$\alpha_{0.8}$	Absorption coefficient at 0.8 eV photon energy
α_{app}	Apparent Absorption coefficient
α_{true}	True Absorption coefficient
A	Absorption
AiC	Aluminium Induced Crystallisation
at.%	atomic weight percentage
a-Si:H	Hydrogenated amorphous silicon
Å	1 Ångstrom = 10^{-10} m
AFM	Atomic Force Microscope
AM1.5	Air Mass 1.5
B-R	Back-Reflector
C_H	hydrogen content in at.%
CPM	Constant Photocurrent Method
c-Si	Crystalline Silicon
E_A	Activation Energy
E_g	Bandgap (Energy gap)
ESR	Electron Spin Resonance
FF	Fill-Factor
FIB	Focused Ion Beam
FT-IR	Fourier Transform Infra Red spectroscopy
H	Haze Factor
H_α	optical emission line of hydrogen at 656 nm
HW	Hot Wire

Table B.1: Abbreviation List 1.

$< i >$	Intrinsic, undoped
J_{SC}	Short Circuit Density
λ	wavelength Lambda
LP-CVD	Low Pressure Chemical Vapour Deposition
mbar	milli bar
MHz	Mega Hertz
meV	milli Electron Volt
mm	milli meter
μc-Si:H	Hydrogenated microcrystalline silicon
$\mu^\circ \cdot \tau^\circ$	mobility lifetime product
μm	1 micrometer = 10e-6 m
N_2	Nitrogen
n-i-p	substrate solar cell: substrate/n/intrinsic/p
$< n >$	n-type doped film
OES	Optical Emission Spectroscopy
p-i-n	superstrate solar: substrate/p/intrinsic/n
$< p >$	p-type doped
PDS	Photothermal deflection Spectroscopy
Φ_C	Crystalline volume fraction detected by Raman spectroscopy
R, RD, RT	Reflectance, Diffuse Reflectance, Total Reflectance
RMS	Root Mean Square: $\delta_{RMS} = \frac{1}{N}\sqrt{\sum_{i,j=1}^{N}(\xi_{ij} - \overline{\xi})^2}$
SiH_4	Silane gas
SC	Silane Concentration: $\frac{[SiH_4]}{[SiH_4+H_2]}$
SCC-VHF	Static Closed Chamber Very High Frequency
sccm	Standard Cubic Centimeter
SEM	Scanning Electron Microscope
σ_{dark}	Dark conductivity
SiH*	optical emission line of silane at 414 nm
Sq	see RMS
T	Transmittance
TEM	Transverse Electron Microscope
PE-CVD	Plasma Enhanced Chemical Vapour Deposition
UV-Vis	Ultra Violet Visible
VHF-GD	Very High Frequency Glow Discharge
V_{OC}	Open Circuit Voltage
XRD	X-Ray Diffraction
$< 100 >$	crystalline plane orientation in Millers index
ZnO, ZnO:Al	Zinc Oxide, Aluminium doped ZnO

Table B.2: Abbreviation List 2.

Bibliography

A

[1] Source NREL: ASTM E 892 - 87 standard (normalised to 1000 W/m^2), IEC standard 60904-1

[2] Armin G. Aberle, Nils-Peter Harder and Stefan Oelting, "Formation of large-grained uniform poly-Si films on glass at low temperature", Journal of Crystal Growth, Volume 226, Issues 2-3, June 2001, Pages 209-214.

B

[3] J. Bailat, E. Vallat-Sauvain, L. Feitknecht, C. Droz, A. Shah, "Influence of substrate on the microstructure of microcrystalline silicon layers and cells", ICAMS 2001, Nice, France, 2001, J. Non-Crystalline Solids Vol. 299-302, pp. 1219-1223.

[4] J. Bailat, E. Vallat-Sauvain, L. Feitknecht, C. Droz, A. Shah, "Microstructure and open-circuit voltage of n-i-p microcrystalline silicon solar cells", J. of Appl. Phys., May 2003, Vol. 93, No. 9, pp. 57275732.

[5] P. A. Basore, "Pilot Production Of Thin-Film Crystalline Silicon On Glass Modules", Pacific Solar Pty Limited, Presented at the 29th IEEE Photovoltaic Specialists Conference, New Orleans, 21 May 2002

[6] R.B. Bergmann, "Crystalline Si thin-film solar cells: a review", Appl. Phys. A 69, 187194 (1999)

[7] M. H. Brodsky, M. Cardona, and J. J. Cuomo, "Infrared And Raman-Spectra Of Silicon-Hydrogen Bonds In Amorphous Silicon Prepared By Glow-Discharge And Sputtering" Phys. Rev. B 16, 3556 (1977).

[8] P. Broguiera and J.P. Conde, "Amorphous and microcrystalline silicon films deposited by hot-wire chemical vapour deposition at filament temperatures between 1500 and 1990°C", J. Appl. Phys. 79 (1996) pp. 8748-8760

[9] The Beer law is derived from the definition of Transmittance (T) in presence of Reflectance (R) for a film of thickness d:

$$T = (1 - R)e^{-\alpha \cdot d} \tag{B.1}$$

is a good approximation in the region between full absorption and the beginning of interference fringes, i.g. between $\alpha \cdot d = 5$ and $\alpha \cdot d = 2$ see for instance Saleh Teich or M. Born

[10] N. Beck, M. Vanecek, J. Meier, R. Flückiger, A. Shah, J. Pohl, "Enhanced Optical Absorption in Microcrystalline Silicon", Journal of Non-Crystalline Solids, 1996, Vol. 198-200, pp. 903-906.

[11] N. Beck "Optical and electrical properties of hydrogenated amorphous and microcrystalline silicon for solar cell applications", Ph.D. Thesis, IMT, Uni Neuchâtel 1997, Ufo Atelier für Gestaltung & Verlag, Band 327, ISBN 3-930803-26-7.

C

[12] P. Campbell, M.A. Green, "Light trapping properties of pyramidally textured surfaces" Journal of Applied Physics, 62 (1): pp. 243, 1987

[13] J. Cifre, J. Bertomeu, J. Puigdollers, M. C. Polo, J. Andreu, and A. Lloret, "Polycrystalline silicon films deposited by Hot-Wire chemical vapour deposition", Appl. Phys. A 59, 1994, p. 645

D

[14] J.M. Dubois, G. Wileke, K. Prasad, O. Blenk, A. Shah, E. Bucher, "Hall Effect Studies on VHF-prepared GD c-Si thin Films", Proceedings of the 11th EC Photovoltaic Solar Energy Conference, Montreux, October 1992,pp. 718-721

[15] H.W. Deckman, C.R. Wronski, H. Witzke, E. Yablonovitch, "Optically enhanced amorphous-silicon solar-cells", Applied Physics Letters, 42 (11): 968-970 1983

[16] C. Droz, E. Vallat-Sauvain, J. Bailat, L. Feitknecht, A. Shah, "Application Of Raman Spectroscopy For The Microstructure Characterisation In Microcrystalline Silicon Solar Cells", Proceedings of the 17th EU Photovoltaic Solar Energy Conference, Munich, October 2001

[17] to be published in Solar Energy Materials & Solar Cells

E

[18] C. Eisele, C. E. Nebel and M. Stutzmann, "Periodic light coupler gratings in amorphous thin film solar cells", J. Appl. Phys., Vol. 89, No. 12, 15 June 2001

F

[19] L. Feitknecht, O. Kluth Y. Ziegler, X. Niquille, P. Torres, J. Meier, N. Wyrsch and A. Shah (2001). "Microcrystalline n-i-p solar cells deposited at 10 Å/s by VHF-GD". Solar Energy Materials & Solar Cells 66, 397-403

[20] L. Feitknecht, P. Torres , J. Zürcher and A. Shah. "Plasma deposition of thin film silicon: Kinetics monitored by optical emission spectroscopy", Proc. of the 12th International Photovoltaic Science and Engineering Conference, PVSEC12, Cheju Island, Korea, June, 2001, Solar Energy Materials and Solar Cells vol 74/1-4 pp. 539-545

[21] The URL of a Quick Time movie of the kinetics of a closed chamber plasma:
http://www-micromorph.unine.ch/Publications/Videos/cc-VHF-GD4a.mov

[22] oral communication

G

[23] T. Globus, G. Ganguly, PRI Cabarrocas, "Optical characterization of hydrogenated silicon thin films using interference technique", J APPL PHYS 88 (4): 1907-1915 AUG 15 2000.

[24] A. Gross, O. Vetterl, A. Lambertz, F. Finger, A. Dasgupta, and H. Wagner "N-side illuminated microcrystalline silicon solar cells", Appl. Phys. Lett., Vol. 79, No. 17, 22 October 2001

[25] A. Goetzberger, "Optical Confinement in Thin Si-solar cells by diffuse back reflectors", 15th IEEE Photovoltaic Specialists Conference, Orlando, 1981, pp. 867-870.

[26] M. Goerlitzer, N. Beck, P. Torres, N. Wyrsch, A. Shah, J. Appl. Phys. 80, 5111 (1996) M. Goerlitzer, N. Beck, P. Torres, J. Meier, N. Wyrsch, A. Shah, "Ambipolar Diffusion Length and Photoconductivity Measurements on 'Midgap' Hydrogenated Microcrystalline Silicon", J. Appl. Phys., November 1996, Vol. 80, pp. 5111-5115.

[27] M. Goerlitzer, P. Torres, N. Beck, N. Wyrsch, H. Keppner, J. Pohl, A. Shah "Structural properties and electronic transport in intrinsic microcrystalline silicon deposited by the VHF-GD technique", Journal of Non-Crystalline Solids 227230 1998 9961000

[28] M. Goerlitzer, "Propriétés électroniques et structurelles du silicium microcristallin hydrogéné", Ph.D. Thesis, IMT, Uni Neuchâtel 1998, ISBN 2-9700197-0-1, 1998.

[29] E.A. Guliants, W.A. Anderson, "Metal-induced growth of poly-Si on foreign substrates for solar cell applications", Conference Record of the Twenty-Eighth IEEE Photovoltaic Specialists Conference - 2000 (Cat. No.00CH37036). IEEE. 2000, pp.154-7. Piscataway, NJ, USA.

H

[30] M.S. Haque, H. A. Naseem, and W. D. Brown, "Interaction Of Aluminum With Hydrogenated Amorphous-Silicon At Low-Temperatures", J. Appl. Phys. 75 (8): 3928-3935 APR 15 1994.

[31] C. Heine, R.H. Morf, "Submicrometer gratings for solar-energy applications", APPLIED OPTICS 34 (14): 2476-2482 MAY 10 1995

[32] S.R. Herd, P. Chaudhari, and M. H. Brodsky, "Metal Contact Induced Crystallisation In Films Of Amorphous Silicon And Germanium", J. Non-Cryst. Solids 7, 309-327 (1972).

[33] L.J. Heyderman, H. Schift, C David, B Ketterer, M. Auf der Maur, J. Gobrecht, "Nanofabrication using hot embossing lithography and electroforming", MICROELECTRONIC ENGINEERING , 57-8: 375-380 SEP 2001

[34] W. Ma, T. Hirade, N. Toyozawa, H. Okamoto, and Y. Hamakawa, Proceedings of the 9th International PVSEC; Miyazaki, Japan, 1996, p. 693.

[35] L. Hultman, A. Robertsson, H. T. G. Hentzell, I. Engström, and P. A. Psaras, "Crystallization of amorphous silicon during thin-film gold reaction"J. Appl. Phys. 62, 3647 (1987).

[36] L. Houben, M. Luysberg, P. Hapke, R. Carius, F. Finger, H. Wagner, "Structural properties of microcrystalline silicon in the transition from highly crystalline to amorphous growth", Phil. Mag. A 77 (1998) 1447.

[37] N-P Harder, JA Xia, S. Oelting, O. Nast, P. Widenborg, A.G. Aberle, "Low-temperature epitaxial thickening of sub-micron poly-Si seeding layers on glass made by aluminium-induced crystallisation", Conference Record of the Twenty-Eighth IEEE Photovoltaic Specialists Conference 2000, pp.351-4.

I

J

[38] G. Juska, M. Viliunas, K. Arlauskas, N. Nekrasas, N. Wyrsch, and L. Feitknecht "Hole Mobility in μc-Si:H", J. Appl. Phys., May 2001, Vol. 89, No. 9, pp. 49714974.

K

[39] M.J. Keevers and M.A. Green, "Absorption edge of silicon from solar cell spectral response measurements", Appl. Phys. Lett. 66, 174 (1995).

[40] J. Kocka, J. Stuchlik, H. Stuchlikova, V. Svrcek, P. Fojtik, T. Mates, K. Luterova, and A. Fejfar,"Amorphous/microcrystalline silicon superlattices - the chance to control isotropy and other transport properties", Appl. Phys. Lett., Vol. 79, No. 16, 15 October 2001

[41] A. Kuoni, M. Goetz and A. Shah, "Light trapping, piègage de lumière pour des cellules solaires comme élément de façade", travail de sémestre Institut de Microtechnique Neuchâtel 1996

[42] M.J. Kushner, "A Model For The Discharge Kinetics And Plasma Chemistry During Plasma Enhanced Chemical Vapor-Deposition Of Amorphous-Silicon", J. Appl. Phys. 63(8), 1988, p.2532 ff.

[43] O. Kluth, A. Löffl, S. Wieder, C. Beneking, W. Appenzeller, L. Houben, B. Rech, H. Wagner, S. Hoffmann, R. Waser, J. A. Anna Selvan, and H. Kepner, "Texture Etched Al-Doped ZnO: A New Material for Enhanced Light Trapping in Thin Film Solar Cells", Proceedings of the 26th PVSC, Anaheim, CA, 1997 (IEEE, New York, 1997), p. 715.

[44] S.Koynov, R. Schwarz, T. Fischer, S. Grebner and H. Münder (1994), "Closed-Chamber Chemical Vapor Deposition: New Cyclic Method for Preparation of Microcrystalline Silicon Films", Jpn. J. Appl. Phys. Vol. 33 pp.4534-4539.

[45] U. Kroll, J. Meier, A.Shah, S. Mikhailov, J. Weber (1996). "Hydrogen in Amorphous and Microcrystalline Silicon Films prepared by Hydrogen Dilution", J. Appl. Phys. 80, 4971-4975.

[46] U. Kroll, J. Meier, P. Torres, J. Pohl, A. Shah, "From Amorphous to Microcrystalline Silicon Films Prepared by Hydrogen Dilution Using the VHF(70MHz) GD Technique", J. Non-Crystalline Solids, 17th International Conference on Amorphous and Microcrystalline Semiconductors, Budapest, August 1997 , 1998, Vol. 227-230, pp. 68-72.

L

[47] R.M. Langford, A.K. Petford-Long, "Preparation of transmission electron microscopy cross-section specimens using focused ion beam milling", Journal Of Vacuum Science & Technology A-Vacuum Surfaces And Films 19 (5): 2186-2193 Sep-Oct 2001

[48] F. Leblanc, J. Perrin, J. Schmitt, "Numerical modelling of the optical properties of hydrogenated amorphous silicon based p-i-n solar cells deposited on rough transparent conducting oxide substrates", Journal of Applied Physics, 75 (2): 1074-1087 JAN 15 1994

M

[49] A. Matsuda, " Formation Kinetics and Control of Microcrystallite in μc-Si:Hfrom Glow Discharge Plasma", (1983) J. Non-Cryst. Solids 59 & 60 pp.767-774.

[50] A. Matsuda, "Growth mechanism of microcrystalline silicon obtained from reactive plasma, Thin Solid Films (1999), 337, 1-6.

[51] J. Meier, R. Flückiger, H. Kepner, A. Shah, "Complete microcrystalline p-i-n solar cell - crystalline or amorphous cell behaviour", Applied Physics Letters 65 (7): 860-862 AUG 15 1994

[52] J. Meier, S. Dubail, R. Flückiger, D. Fischer, H. Keppner, A. Shah, "Intrinsic Microcrystalline Silicon (μc-Si:H) - a Promising New Thin Film Solar Cell Materialin": Proceedings of the first World Conference on Photovoltaic Energy Conversion, Hawaii, December 1994, vol. 1, pp. 409-412.

[53] J. Meier, S. Dubail, S. Golay, U. Kroll, S. Fay, E. Vallat-Sauvain, L. Feitknecht, J. Dubail, A. Shah, "Microcrystalline Silicon and the Impact on Micromorph Tandem Solar Cells", Proc. of the 12th International Photovoltaic Science and Engineering Conference, PVSEC12, Cheju Island, Korea, June, 2001, Solar Energy Materials and Solar Cells vol 74/1-4 pp. 457-467

[54] J. Meier, J. Spitznagel, S. Fa, C. Bucher, U. Graf, U. Kroll, S. Dubail, A. Shah, Enhanced Lighttrapping for Micromorph Tandem Solar Cells by LP-CVD ZnO, Proc. of 29th IEEE PVSC (New Orleans 2002), p. 1118.

[55] Y. Mishima, S. Miyazaki, M. Hirose, Y. Osaka, "Characterisation of Plasma-Deposited Microcrystalline Silicon", Phil. Mag. B 46 (1982), pp. 1-12.

[56] D. W. Marquardt, J. Soc. Ind. Appl. Math. 11 (1963) 431.

N

[57] O. Nast, T. Puzzer, L. M. Koschier, A. B. Sproul, and S. R. Wenham, "Aluminium-induced crystallization of amorphous silicon on glass substrates above and below the eutectic temperature", Applied Physics Letters, Vol. 73, No. 22, pp. 3214-3216, 30 November 1998

[58] O. Nast, S. Brehme, D.-H. Neuhaus, S. R. Wenham, "Polycrystalline silicon thin films on glass by aluminum-induced crystallization", IEEE Trans. Electron. Dev. 46 (1999) 2062.

[59] O. Nast and S. R. Wenham, "Elucidation of the layer exchange mechanism in the formation of polycrystalline silicon by aluminium-induced crystallization", J. Appl. Phys., Vol. 88, No. 1, 1 July 2000.

[60] O. Nast, S. Brehme, S. Pritchard, A. G. Aberle, S. R. Wenham, "Aluminium-induced crystallisation of silicon on glass for thin-film solar cells", Solar Energy Materials & Solar Cells 65 (2001) 385-392.

[61] Y. Nasuno, M. Kondo and A. Matsuda, "Effects of Substrate Surface Morphology on Microcrystalline Silicon Solar Cells", Jpn. J. Appl. Phys. Vol. 40 (2001) L303-L305, Part 2, No. 4A, 1 April 2001

[62] D.H. Neuhaus, R. Bardos, L. Feitknecht, T. Puzzer, M.J. Keevers, and A.G. Aberle, "Minority Carrier Properties Of Single- And Polycrystalline Silicon Films Formed By Aluminium-Induced Crystallisation", Conference Record of the Twenty-Eighth IEEE Photovoltaic Specialists Conference - 2000 (Cat. No.00CH37036). IEEE. 2000, pp.65-8. Piscataway, NJ, USA.

O

[63] M. Otobe and S. Oda, "The Role of Hydrogen Radicals in the Nanocrystallization of Silicon", Proc. Jpn. Plasma Chem. (1992) 5, 123-128.

[64] T. K. Olson, R. G. Lee, and J. C. Morgan, "Contrast Mechanisms in Focused Ion Beam Imaging", Proceedings of the 18th International Symposium for Testing and Failure Analysis, Los Angeles, CA (1992), p.373.

P

[65] R. Platz, "Amorphous silicon for optimized multi-junction solar cells: Material study and cell design", Ph.D. Thesis, IMT, Uni Neuchâtel 1999, UFO Atelier für Gestaltung & Verlag, Band 362, ISBN 3-930803-61-5.

[66] A. Poruba, A. Fejfar, Z. Remes, J. Springer, M. Vanecek, J. Kocka, J. Meier, P. Torres, A. Shah, "Optical absorption and light scattering in microcrystalline silicon thin films and solar cells", Journal of Applied Physics, 88 (1): 148-160 JUL 1 2000

[67] Private communication.

Q

R

[68] D. Redfield, "Multiple-Pass Thin-Film Silicon Solar Cell", Appl. Phys. Lett., Vol. 25, pp. 647, 1974.

[69] B.S. Richards, "Optical Characterisation of Sputtered Silicon Thin Films for Photovoltaic Applications", PhD thesis, Photovoltaic Special Research Centre, School of Electrical Engineering, University of New South Wales Australia, February 1998

S

[70] T. Satoh and A. Hiraki, "Detailed study of Si-H stretching modes in μc-Si:H film through second derivative IR spectra", J. Appl. Phys. 24, L491-L494 (1985)

[71] K. Saito, M. Sano, K. Matuda, T. Kondo, T. Nishimoto, K. Ogawa, I. Kajita, in: Proceedings of the Second WCPSEC, 1999, p. 351.

[72] IMT progress report 1996

[73] J.A. Selvan, Kepner H, Kroll U, Cuperus J, Adatte T, Ketterer C, Shah A, "Material aspects of ZnO to make surface texture growth for light trapping for thin film solar cells", Helvetica Physica Acta, 70: S.9-10, Suppl. 1 1997

[74] J. A. Anna Selvan, H. Kepner, U. Kroll, J. Cuperus, A.Shah, T. Adatte, N. Randall, "The Fiber Texture Growth and the Surface Roughness of ZnO Thin Films", Proceedings of the MRS Symp., Spring Meeting, San Francisco, April 1997, Vol. 472, pp. 39-44.

[75] J. A. Anna Selvan,"ZnO for Thin-Film Solar Cells", UFO Atelier für Gestaltung & Verlag, Band 361, ISBN 3-930803-60-7, 1999

[76] R. S. Sposili and J. S. Im, "Sequential lateral solidification of thin silicon films on SiO_2", Appl. Phys. Lett. 69, 2864 (1996).

[77] J. Springer, A. Poruba, A. Fejfar, M. Vanecek, L. Feitknecht, N. Wyrsch, J. Meier and A. Shah, "Nanotextured thin film silicon solar cells: Optical model", Solar Energy Materials and Solar Cells, presented at PVSEC-11, Sapporo, 20-24 September 1999, Vol. 66, 2001

[78] J. Springer, A. Poruba, A. Feifar, M. Vanecek, N. Wyrsch, L. Feitknecht, J. Meier, A. Shah, "Nanotextured Thin Film Silicon Solar Cells: Optical Model", Proceedings of the 16th EE Photovoltaic Solar Energy Conference, Glasgow, UK, May 2000, pp. 434-437.

[79] N. Sridhar, D.D.L. Chung, W.A. Anderson, J. Coleman, "Polysilicon films of high photoresponse, obtained by vacuum annealing of aluminum capped hydrogenated amorphous silicon", J. Appl. Phys. 78 (12), 1995, p. 7304.

[80] S.M. Sze, "Semiconductor devices, Physics and Technology", book, J. Wiley & Sons, 1985

[81] R. E. I. Schropp, K. F. Feenstra, E. C. Molenbroek, H. Meiling, and J. K. Rath, "Device-quality polycrystalline and amorphous silicon films by Hot-Wire chemical vapour deposition", Phil. Mag. B, Vol. 76, 1997, pp. 309-321

[82] R. Swanepoel, "Determination of the thickness and optical constants of amorphous silicon", J. Phys. E: Sci. Inst. 16, (1983) p. 1214

T

[83] B-Y. Tsaur, G.W. Turner, J.C.C. Fan, "Efficient Si solar cells by low-temperature solid-phase epitaxy", Appl. Phys. Lett. 39, 749 (1981).

[84] F. A. Trumbore, Bell Syst. Tech. J. 39, 205 (1960).

[85] J. Turunen and F. Wyrovski, "Diffractive Optics", book, Wiley Akademie Verlag Berlin 1998, ISBN 3-527-40100-8, pp. 361-389

[86] P. Torres, J. Meier, R. Flückiger, U. Kroll, J. Anna Selvan, H. Keppner, A. Shah, S.D. Littlewood, I.E. Kelly, P. Giannoulès, "Device Grade Microcrystalline Silicon Owing to Reduced Oxygen Contamination", Appl. Phys. Lett., September 1996, Vol. 69, pp. 1373-1375.

[87] P. Torres, J. Meier, U. Kroll, N. Beck, H. Keppner, A. Shah, U. Malang,"Fast Deposited Microcrystalline Silicon Solar Cells", Proceedings of the 26th IEEE Photovoltaic Specialists Conference, Anaheim, CA, September-October 1997, pp. 711-714.

[88] P. Torres, U. Kroll, H. Keppner, J. Meier, E. Sauvain and A. Shah, "Deposition of Thin-Film Silicon for Photovoltaics: Use of VHF-GD and OES", Proc. of the 5th Thermal Plasma Process St. Petersburg.

[89] P. Torres, "Hydrogenated Microcrystalline Silicon Deposited by VHF-GD for Thin-Film Solar Cell", Ph.D. Thesis, IMT, Uni Neuchâtel 1998, ISBN 3-930803-51-8

[90] P. Torres work in [66]

U

V

[91] The factor of 12 between apparent and true optical absorption coefficient alpha is documented in [66].

[92] M. Vanecek, A. Poruba, Z. Remes, J. Rosa, S. Kamba, V. Vorlicek, J. Meier, A. Shah "Electron spin resonance and optical characterization of defects in microcrystalline silicon", Journal of Non-Crystalline Solids 266-269 (2000) pp. 519-523

[93] M. Vanecek, J. Kocka, A. Poruba and A. Fejfar, "Direct measurement of the deep defect density in thin amorphous silicon films with the "absolute" constant photocurrent method", J. Appl. Phys. 78, 6203 (1995)

[94] M. Vanecek, J. Kocka, J. Stuchlik and A. Triska, "Direct measurement of the gap states and band tail absorption by constant photocurrent method in amorphous silicon", Sol. State Commun. 39 (1981) 1199.

[95] S. Veprek, F.A. Sarott, Z. Iqbal, "Effect of grain boundaries on the Raman spectra, optical absorption, and elastic light scattering in nanometer-sized crystalline silicon.", Phys. Rev. B36 (1987) 3344.

[96] E. Vallat-Sauvain, U. Kroll, J. Meier, A. Shah, J. Pohl, "Evolution of the Microstructure in Microcrystalline Silicon Prepared by Very High Frequency Glow-Discharge using Hydrogen Dilution", J. Appl. Phys., March 2000, Vol. 87, pp. 3137-3142.

W

[97] R. L. Wallace, B. Jagannathan, X. Gu, N. Sridhar, K. Etemadi, D. D. L. Chung, and W. A. Anderson, J. Coleman, "Low-cost, thin-film silicon for terrestrial solar cells", AIP Conference Proceedings, January 25, 1996, Volume 353, Issue 1, pp. 511-518.

[98] J. H. Werner, R. Bergmann, and R. Brendel, in Festkoerperprobleme/Advances in Solid State Physics, edited by R. Helbig (Vieweg, Braunschweig, 1995), Vol. 34, p. 115.

[99] P. Winkler, V. Daudrix, A. Shah, "Dépôts d'argent texturé comme réflecteurs diffusants pour les cellules solaires en silicium amorphe", Diploma work report, Ecole polytechnique Fédérale de Lausanne & Institut de Microtechnique Neuchâtel, 2001

[100] N. Wyrsch, P.Torres, M. Goerlitzer, E. Vallat, U. Kroll, A. Shah, M. Vanecek, "Hydrogenated Microcrystalline Silicon for Photovoltaic Applications", Proceedings of the 5th International Conference on Polycrystalline Semiconductors - POLYSE'98, , Schwäbisch-Gmünd, Germany, Polycrystalline Semiconductors V - Bulk Materials, Thin Films, and Devices, J.H. Werner, H.P. Strunk, H.W. Schock eds., in Series "Solid State Phenomena", Scitech Publ., Uettikon am See, Switzerland 1999,Vol. 67-68, pp. 89-100.

[101] N. Wyrsch, L. Feitknecht, C. Droz, P. Torres, A. Shah, A. Poruba and M. Vanecek, "Hydrogenated Microcrystalline Silicon: How to Correlate Layer Properties and Solar Cell Performance", J. Non-Crystalline Solids, presented at 18th International Conference on Amorphous and Microcrystalline Semiconductors, ICAMS18, Snowbird UT, August 1999, 2000, Vol. 266-269, pp1099-1103.

[102] N. Wyrsch, C. Droz, L. Feitknecht, M. Goerlitzer, U. Kroll, J. Meier, P. Torres, E. Vallat-Sauvain, A. Shah, M. Vanecek, "Hydrogenated Microcrystalline Silicon: From Material to Solar Cells", Proceedings of the MRS Symp., Spring Meeting, San Francisco, April 2000, Vol. 609, 2001, pp. A15.1.1-A15.1.11.

[103] N. Wyrsch, C. Droz, L. Feitknecht, P. Torres, E. Vallat-Sauvain, J. Bailat, A. Shah, "Effect of the Microstructure on the Electronic Transport in Hydrogenated Microcrystalline Silicon", proc. of the 19th International Conference on Amorphous and Microcrystalline Semiconductors, Nice, France, 2001. J. of Non-Cryst. Sol.

[104] N. Wyrsch, C. Droz, L. Feitknecht, J. Spitznagel, A. Shah, "Transport Path in Microcrystalline Silicon", Proceedings of the MRS Spring Meeting, San Francisco, April 2002, Vol. 715., 2002, pp. A25.3.1-A25.3.6.

[105] N. Wyrsch, C. Droz, L. Feitknecht, P. Torres, E. Vallat-Sauvain, J. Bailat, A. Shah, "Effect of the microstructure on the electronic

transport in hydrogenated microcrystalline silicon", [Conference Paper], Journal of Non-Crystalline Solids, vol.299-302, pt.A, April 2002, pp.390-4.

X

[106] H. Xia, Y.L. He, L.C. Wang, W. Zhang, X.N. Liu, X.K. Zhang, D. Feng, H.E. Jackson, "Phonon mode study of Si nanocrystals using micro-Raman spectroscopy", J. Appl. Phys. 78 (1995) 6705.

Y

[107] K. Yamamoto, A. Nakajima, M. Yoshimi, T. Sawada, S. Fukuda, K. Hayashi, T. Suezaki, M. Ichikawa, Y. Koi, M. Goto, H. Takata, Y. Tawada, High Efficiency Thin Film Silicon Solar Cell and Module, Proc. 29th IEEE PVSC (New Orelans 2002), p. 1110.

[108] E. Yablonovitch, G.D. Cody, "Intensity enhancement in textured optical sheets for solar cells", IEEE transactions on Electron Devices, 29 (2): 300-305 1982

Z

[109] Y. Ziegler, "Le dépot du silicium amorphe hydrogéné par la méthode dite du filament chaud: De l'optimisation de la couche intrinsèque à son intégration dans la cellule solaire", Ph.D. Thesis, IMT, Uni Neuchâtel 1997.

[110] Y. Ziegler, S. Dubail, Ch. Hof, U. Kroll, A. Shah, "High Efficiency p-i-n Solar Cells with $< i >$ Deposited by the Hot-Wire Technique", Proceedings of the 26th IEEE Photovoltaic Specialists Conference, Anaheim, CA, September-October 1997, pp. 687-690.

Acknowledgements

First of all, I would like to thank Prof. Arvind Shah who made this work possible within the frame of his research group. The rich mixture of cultures, languages and personal points of views as well as the steadily developed laboratory equipment could give a fruitful impact on my work.

I also appreciate the acceptance of Dr. Herbert Keppner, Dr. Milan Vanecek and Dr. Hans Peter Herzig to join the examination board and to devote time to the critical reading of this thesis.

I thank Pedro Torres, Hannes Meier and Ulli Kroll who introduced me to the technology and 'art' of μc-Si:H thin film solar cell manufacturing. It was also a rich experience sharing the same office with Pedro, a common interest for Australia or some good ideas of a 'friday afternoon experience' up there in the lab, where the μc-Si:H "flame" will burn and develop much longer than the time of a PhD thesis.

Joelle Guillet and Nicolas Wyrsch guided in their way the maturing process of my PhD thesis.

A special thank goes to all my colleagues at the 'Thin-Film Silicon and Photovoltaics' group. This includes those numerous unmentioned jobs from substrate cleaning to good advise from the mechanical work-shop. In the secretary there were Sylvie Baillot, Joelle Banjac and formerly Ingrid Mantle who helped not only with that paperwork related to this thesis but they also helped in a more human way.

Thanks also to all other members of the Institut de Microtechnologie, Neuchâtel.

A part of this work was done at the Photovoltaics Research Center at the University of New South Wales, Sydney in the research group of Dr. Armin Aberle. His and his wife Anjas kind support during my first days 'down under', the experienced atmosphere of the researchers of the PV-center and the friendly social ambience of its members turned my stay in Sydney in a rich experience. This six month research work was partially supported by the "Fondation Charles-Edouard Guillaume", Bienne and the community of Cortaillod, Neuchâtel.

Another part of this work was done during the European JOULE project. I acknowledge the collaboration with the PV group of the Forschungszentrum Jülich, Germany, on this exhaustive topic of microcrystalline silicon solar cell manufacturing in all its aspects. Beside technological aspects, there is optics of thin-films where Ales Poruba from the Prag group contributed to solve many questions.

The chapter on Thermography for shunt detection on solar cells came out of a collaboration with Otwin Breitenstein of Max-Planck-Institut für Mikrostrukturphysik Halle, Germany.

In memory of my parents, who passed away too early.
I finally wish to thank my wife Barbara who accompanied me over the last seven years of ups and downs in live. Our first son, Basil, was born just two weeks after the public presentation of this thesis.